Spring 2017

Development of piezocatalytic nanomaterials for applications in sustainable water treatment

Brandon Jennings
University of Iowa

Recommended Citation

Jennings, Brandon. "Development of piezocatalytic nanomaterials for applications in sustainable water treatment." MS (Master of Science) thesis, University of Iowa, 2017.
https://doi.org/10.17077/etd.libi-1o63

Follow this and additional works at: https://ir.uiowa.edu/etd
Part of the Civil and Environmental Engineering Commons

DEVELOPMENT OF PIEZOCATALYTIC NANOMATERIALS FOR APPLICATIONS IN SUSTAINABLE WATER TREATMENT

by

Brandon Jennings

A thesis submitted in partial fulfillment
of the requirements for the Master of Science
degree in Civil and Environmental Engineering in the
Graduate College of
The University of Iowa

May 2017

Thesis Supervisor: Associate Professor David M. Cwiertny

Graduate College
The University of Iowa
Iowa City, Iowa

CERTIFICATE OF APPROVAL

MASTER'S THESIS

This is to certify that the Master's thesis of

Brandon Jennings

has been approved by the Examining Committee for
the thesis requirement for the Master of Science degree
in Civil and Environmental Engineering at the May 2017 graduation.

Thesis Committee: ____
David M. Cwiertny, Thesis Supervisor

____
Richard L. Valentine

____
Syed Mubeen

To my best friends, my siblings, my parents. I would not be here without you.

ACKNOWLEDGEMENTS

First and foremost, I would like to thank my advisor, David Cwiertny, who has been my mentor, guide, and advocate throughout my undergraduate and graduate coursework and research. Thank you for your constant encouragement and patience with me as I struggled to come into my own as an engineer. You have been and continue to be an inspiration with your positivity and your outrageous work ethic.

To all of my lab mates – Jiajie Qian, Kathy Peter, Katie Greenstein, Matt Nagorzanski, A.J. Johns, Andrew Kral, Kathryn Klarich, Nick Pflug, Edgard Verdugo, Haydar alAlawan, and Aruni Gankanada – thank you for being forgiving when I forgot sometimes to wash my beakers. More seriously, you all have made the past several years fun, engaging, and utterly weird in all the best ways.

I would like to thank our collaborators at the University of California, Riverside, especially: Gerardo Ico, Nosang Myung, and Jin Nam whose assistance in material characterization truly helped pull this project together.

This work would not have been possible without the funding of the National Science Foundation (Grant No. 1437989) or the continued support of the federal government for scientific inquiry and technological development.

To my family, whose endless support is really the reason why I've gotten this far. My parents, especially, were bastions Dad, thank you for encouraging me to pursue engineering as a means to advance my goals. Mom, thank you for consistently checking in with me and so frequently sending me tokens of support.

ABSTRACT

Piezoelectric materials produce an electric potential in response to a mechanical strain. They are, therefore, capable of converting ambient waste mechanical energy into useful electrical energy which, in turn, may be harnessed and used as a supplemental source of power in a variety of applications. Engineered piezoelectric materials may be deployed to improve treatment efficiency during the production of potable water, which is both chemically and energetically intensive. Ambient mechanical energy is prevalent in municipal water treatment. Vibrations induced by water treatment plant pumps (such as High Service Pumps), turbulence resulting from cross-flow or dead-end membrane filtration, or agitation from mechanical mixing (paddle or impeller) may provide sufficient input mechanical input energy to activate a piezoelectric response.

The objective of this work was to fabricate and characterize a range of nanofiber-based piezoelectric materials and demonstrate their application as an alternative energy supply for driving environmental treatment (e.g., pollutant degradation) via simple mechanical agitation. To achieve this objective, we fabricated a variety of piezoelectric nanofiber composite mats consisting of barium titanate (BTO) nanocrystals grown via an alkaline hydrothermal method atop an electrospun carbon nanofiber (CNF) support.

We hypothesized that the greatest degree of piezoelectric activity (as measured by the voltage produced as a function of mechanical strain) would be achieved for nanofiber composites containing BTO with the largest fraction of tetragonal crystal structure, known to be piezoelectrically active. A systematic study on the impacts of hydrothermal treatment time, temperature, as well as the influence of ethylene glycol as an organic co-solvent on BTO crystal size and morphology was performed. For example, ethylene glycol was found

to disrupt the dissolution-precipitation mechanism of BTO crystal growth and instead spurred the growth of BTO nanorods and nanosheets on the CNF support.

After characterization, the strength and electromechanical properties of various BTO-CNF composites was assessed. In some cases, output voltages have been measured on the order of 2.0 V/cm^2 in response to surface bending strain induced by a custom cantilever-oscillometer apparatus. Optimal fractions of BTO loading in the composites were assessed through mass-loading electromechanical studies.

As a proof of concept application, BTO nanoheterostructures were shown to utilize ultrasonic vibrations to degrade sodium orange II salt (4-(2-Hydroxy-1-naphthylazo)benzenesulfonic acid sodium salt) via piezocatalysis. Ongoing and future work will continue to develop optimized piezocatalytic nanoheterostructures able to harvest the electrochemical potential generated from mechanical agitation and structural deformation for the production of oxidizing and reducing equivalents for degradation of persistent and emerging organic contaminants and disinfection in water treatment.

PUBLIC ABSTRACT

Due to extensive water quality and quantity challenges, water utilities nationwide are having to consume increasing amounts of energy and chemicals to produce water that meets demand as well as regulatory standards for quality. Water treatment is, therefore, both becoming more expensive and deepening its carbon footprint. Accordingly, and in light of climate change and resource scarcity, there is mounting pressure for water utilities to improve sustainability and incorporate technologies that optimize chemical and energy efficiency.

In this work, we have developed a novel class of materials to meet the challenge of sustainable, energy-efficient water treatment. When piezoelectric materials bend or deform, they produce a voltage that can be harnessed for a variety of processes. This ability makes piezoelectric materials popular in many everyday commercial applications such as spark plugs, buzzers, and actuators.

Here, we are among the first to evaluate and demonstrate the application of piezoelectric materials for water purification. We successfully produced nanotechnology-enabled materials that can harness readily available but underutilized forms of waste energy (e.g., vibrations from pumps or turbulently flowing water) to induce their structural deformation, which in turn generates forms of chemical energy that can be used to help purify water. The materials here hold much promise for integration into future water treatment technologies, including advanced processes like membrane filtration, where their ability to drive chemical reactions should improve the overall efficiency and sustainability of treatment.

TABLE OF CONTENTS

LIST OF TABLES

LIST OF FIGURES

CHAPTER 1 INTRODUCTION

1.1 Emerging challenges to water quality and quantity necessitate advanced treatment and distribution infrastructure

Water utilities across the United States are struggling with deteriorating source water quality and quantity in the face of tightening regulations and heightened demand. In particular, increased loadings of emerging and as yet unregulated contaminants (synthetic organics, metals, pathogens, or otherwise) coupled with dated treatment and distribution infrastructure are forcing municipalities, private water service providers, and consumers to rely on advanced treatment technologies to sufficiently meet public health standards.

In agricultural regions, the accumulation of fertilizers and pesticides in surface and groundwater(s) represent an incipient obstacle to clean and safe drinking water. A 2013 study of 100 small streams across the Midwest found an average of 62 pesticides (or degradants thereof) in each sample and detected 141 of the 227 pesticides surveyed at least once [1]. Another study of Midwestern drinking water utilities found 40% of the monitored systems had peak concentrations of the pesticide atrazine above the Safe Drinking Water Act (SDWA) Maximum Contaminant Level (MCL) of 3 ppb [2]. Further, hydrophilic and persistent pharmaceuticals such as metroprolol have been detected up to hundreds of nanograms per liter even in groundwater samples [3]. As a result, emerging organic contaminants such as pharmaceuticals and personal care products (PPCPs), as well as plasticizers, antioxidants, and many other synthetic organic chemicals are routinely detected in many environmental compartments – soil, surface water, groundwater, as well as the fatty tissues of organisms (although generally at low concentrations - ppb or ppt) [4, 5]. The sheer diversity of chemical structures and character of emerging synthetic organic contaminants pose a significant challenge to utilities that rely on mechanisms for targeted pollutant capture – such as adsorption to activated carbon or metal-salt coagulants [6].

The lack of toxicological data or chronic health studies on these chemicals has raised concerns about public and environmental health implications of long-term exposure to low concentrations of PPCPs [7]. Some PPCPs released into the environment are also hormonally active (endocrine disrupting) and have been highlighted as a subset of emerging contaminants that could induce health effects at relatively low concentrations over chronic exposure (μg/L or ng/L levels) [8]. Accordingly, many of such emerging contaminants are listed under the EPA’s Contaminant Candidate List (CCL). The CCL is a compilation of contaminants for which the EPA is considering primary drinking water standards because of their measured occurrence in supplies, but has not yet issued such standards due to insufficient data on prevalence, toxicity, and removal mechanisms [9].

Dwindling water resources in arid, coastal, or agricultural regions is another stressor for water quality and quantity. According to a recent edition of the United Nations World Water Development Report, an estimated 21 of the 37 largest aquifers in the world are severely over-exploited [10]. Concurrent with a rising global population, the overall rate of groundwater withdrawals is increasing by an estimated 1-2% per year [10]. Continued urbanization and migration to coastal regions as well as enhanced climate uncertainty will constitute an added pressure to already limited coastal water resources [10]. By 2030, for instance, it is estimated that nearly 60% of the world’s population will live near a coastal region [11]. Coastal aquifers and surface water sources will not be able to support a burgeoning urban population.

Pumping and discharging drinking water source water from inland areas into saline coastal waters is also inherently unsustainable. As a result, many coastal communities are beginning to adopt water conservation measures, such as direct or indirect potable reuse of treated wastewater (DPR and IPR, respectively). The EPA estimated in 2004 that a total of 1690 MGD of treated wastewater was beneficially reused in the United States and growing at approximately 15% per year [12]. Florida, Texas, and California are among the leaders in the development and implementation of engineered IPR and DPR systems in the United States. In 2015, for instance, the State of Florida reported that there were 478 wastewater treatment facilities that produced effluent available for reuse [13]. In sum, these facilities had a total capacity of 2,374 MGD – of which approximately 738 MGD was consistently reused for beneficial purposes [13].

The persistence of synthetic organic contaminants in drinking water is a concern especially for communities implementing direct or indirect potable reuse of wastewater in response to a dwindling or uncertain water supply. It has been well-documented that conventional and even advanced wastewater treatment technologies do not fully remove synthetic organic chemicals from influent waste streams. A review of over 40 published studies and 1500 data points suggested that, at best, conventional wastewater treatment processes (primary and secondary treatment) are capable of achieving a 1-log reduction in PPCP concentrations, although in general much larger fractions (~0.39) persisted in the effluents (Figure 2) [14]. In fact, several states, such as California, Florida, Texas, Arizona, Colorado, Georgia, and Oklahoma have made strides to adopting significant water recycling programs. In 2013, the Colorado River Municipal Water District (CRMWD) in Big Spring, Texas, opened the first direct potable reuse facility in the United States –

capable of treating 2 MGD of wastewater to drinking water quality. Similar facilities are being built across the country to address water scarcity concerns. To ensure the quality of recycled water, such facilities are implementing advanced treatment technologies such as reverse osmosis (RO) and advanced oxidation processes employing ultraviolet (UV) light and ozone.

1.2 Growing energetic and chemical footprints of treatment increase costs and threaten access to clean and safe drinking water

To meet these and other emerging challenges, public and private water providers are turning to advanced treatment technologies such as membrane filtration, ion exchange, electrodialysis, advanced oxidation, and others to reliably remove problematic chemical and biological contaminants from source water, as in the case of water reuse facilities. Complete degradation and removal of synthetic organic contaminants, for instance, generally requires the application of an advanced oxidation process (AOP). Defined broadly, an AOP relies on the oxidative power of highly reactive chemical intermediaries - the most common being oxygen-derived radicals such as hydroxyl radicals ($\bullet OH$) and superoxide anions ($O_2^{\bullet -}$). Because of their promise, AOPs have been the subject of intense research and development over the past decade. Between 2005 and 2007, more than 4,500 articles were published in journals of the Science Citation Index related to a variety of advanced oxidation techniques, including photocatalysis, ozonation, Fenton reactions, and others [15].

Chemical oxidation processes, including advanced oxidation, are also becoming increasingly popular in municipal potable and wastewater treatment. For example, the number of drinking water facilities utilizing ozonation has increased dramatically from 40 in 1990 to 277 in 2013, producing a combined volume of 14.5 billion gallons per day [16, 17]. Membrane filtration technology has also experienced a boom in development since the 1990s given the accelerated rise of patents filed shown in (Figure 3) [18]. Accordingly, recent trends toward increased DPR and IPR will only accelerate the application of advanced treatment processes, especially AOPs. For example, the newly constructed DPR facility in Big Springs, Texas sequentially incorporates microfiltration, reverse osmosis filtration, and advanced oxidation (Figure 4). Indeed, markets for ozonation and reverse osmosis (RO) were projected to grow at a compound annual growth rate (CAGR) of 8.1% and 10.5% annually, respectively, at least until 2019 [19, 20]. These markets are heavily influenced by the water and wastewater sectors [19, 20].

While advanced treatment options are capable of producing high quality finished water, these processes require a substantial increase in power relative to conventional treatment (Figure 4) [21]. The Electrical Power Research Institute (EPRI) estimated that electrical demand for water and wastewater production increased 69% from 1996 to 2013 and cited the implementation of advanced treatment technologies as one of the prime drivers for this increase in power consumption [22]. However, most of this increase in electricity is derived from coal-fired combustion plants with adverse implications for climate change. Through this challenge at the energy-water nexus, the sustainability of such advanced technologies is often called into question unless renewable forms of energy are integrated into their operation.

In addition to a deepening electrical footprint, rising prices of water and wastewater treatment chemicals are compounding costs for private and public water service providers.

Water and wastewater treatment processes typically rely on a diverse suite of chemicals including coagulants, disinfectants, anti-corrosives, oxidizers, pH adjusters, anti-scaling agents, and others to assist in the production of finished water. In fact, as new and increasingly sophisticated water treatment plants are constructed to accommodate population growth, deteriorating water quality, and shrinking quantity, a concomitant surge of chemical consumption should also be expected which will also increase annual operating costs [23]. Exhaustable specialty chemicals such as granular activated carbon (GAC) or ion exchange resins will constitute another recurring cost for water utilities working to remove recalcitrant contaminants. The Freedonia group has estimated that global demand for water treatment chemicals is expected to increase 3.2 percent per year to $7.5 billion in 2019 with volume reaching 15.5 billion pounds (Figure 5) [24].

Consequently, water and wastewater utilities across the United States are approaching a critical juncture. Faced with emergent classes of microcontaminants, heavy metals, and pathogens, as well as aging infrastructure and increasing water consumption, water service providers must find innovative solutions to cut costs associated with the production and distribution of finished water while still maintaining water quality standards and meeting water quantity demands. To this end, there has been much recent research and development focused on next-generation, low-footprint technologies capable of improving overall water treatment process sustainability. Among the technologies at the vanguard of energy-efficient water treatment are low-pressure biomimetic membranes, catalytic nitrate reduction, and photocatalytic advanced oxidation processes [25, 26]. In fact, the inextricable relationship between energy and water, known broadly as the energy-water nexus, has been at the forefront of developing action-plans to address climate change and population growth while promoting environmental stewardship and social responsibility.

1.3 Piezoelectric materials represent an innovative, yet to-date, unexplored technology for improving treatment efficiency

Energy harvesting materials have the capacity to convert mechanical and thermal waste energy into useful electrical energy. For example, pyroelectric materials convert fluxes in thermal energy to an electric potential. Another promising class is piezoelectric materials, which are the focus of this project. We hypothesize that electrical energy may be harnessed with these next-generation materials to improve energy efficiency and sustainability of water treatment while still maintaining the same high level of treatment.

Piezoelectric materials produce an electric potential in response to the application of a mechanical strain. This phenomenon only occurs in materials whose lattice structure(s) lack inversion symmetry and therefore possess a net electric dipole moment. Applying force to a non-centrosymmetric lattice structure will heterogeneously deform the lattice, resulting in a change of the material’s polarization and leading to the formation of an electric potential gradient (voltage) (Figure 6). This is known as the direct piezoelectric effect. The polarization of the lattice temporarily creates local oxidizing (electron deficient) and reducing (electron abundant) environments within the piezomaterial. Conversely, applying an electric potential to a piezoelectric material will force the lattice structures to deform, leading to a minuscule change of shape in the material. This phenomenon is known as the indirect piezoelectric effect.

Piezoelectric technologies offer the capability to harvest and recycle waste mechanical energy into directly usable voltages to improve process efficiency [27]. Modern piezoelectric ceramics such as lead zirconate titanate (PZT), sodium niobate (NBT), or barium titanate (BTO) are distinguished in the field of microelectronics by their exceptionally large power densities (amount of power produced per volume of material). As shown in Figure 7, piezoelectric materials cover the largest range of power densities, comparable to those of lithium ion batteries and thermoelectric generators [27, 28].

Piezoelectric materials are found in myriad consumer and industrial products. Certain appliances such as butane lighters and spark plugs rely on the ceramic piezoelectric element to generate large voltages when struck with a hammer to ignite a gas mixture. Other devices take advantage of the piezoelectric effect to detect mechanical agitation – such as medical ultrasonic transducers, contact microphones, piezoelectric guitar pickups, and strain gauges. And still other technologies are premised off the indirect piezoelectric effect. Certain buzzers and alarms, for instance, contain piezoelectric ceramic disks which rapidly oscillate when subjected to high voltages to produce loud noises. Accordingly, the piezoelectric device market is well-established and growing steadily. By 2022, the piezoelectric device market is expected to be valued at 31.33 Billion USD. Between 2016 and 2022, this market is expected to grow at a CAGR of 4.88% [29].

1.3.1 Constitutive equations and coefficients relating to piezoelectricity

The electric field generated by applying force to a piezoelectric material is given by the following expression:

$$D_m = d_{mi}\sigma_i + \xi_{ik}^{\sigma} E_k \qquad \text{Eq. 1}$$

where D_m is the vector of electric displacement (C/m^2) and ξ is the permittivity of the material (superscript σ represents value taken at constant stress) (F/m), σ is the stress vector (N/m^2), and E is the vector of the applied electric field (V/m) [30]. The indices $i, j = 1, 2 \ldots, 6$ and $m, k = 1, 2, 3$ refer to the material's coordinate system, given in Figure 1 [30]. The 'piezoelectric strain constant' d_{mi} is an empirically assessed ratio of the voltage produced per strain of the material. It is usually defined as the amount of electrical charge delivered by 1 m^2 of the piezoelectric material which has been polarized along axis m when a pressure of 1 Pa is applied in the direction i (frequently pC/N) [30]. The piezoelectric strain constants d_{33} and d_{31} are commonly used industry indicators of piezoactivity and refer to the charge generated when the material is strained along the polarization axis and at a right angle to the polarization axis, respectively. Polarization refers to a common technique in which a large electric potential (often in the tens of kilovolts) is applied across a piezoelectric element for a specified period. Doing so forces the randomly aligned crystalline dipoles in the piezoelectric element to align according to the applied field. When the potential is removed, the dipoles will relax but still maintain relatively uniform orientation. Polarization is used to maximize the observed strain constant d_{mi} (potential produced per stain).

The opposite of the direct piezoelectric effect is the indirect effect whereby the application of an electric field to a piezoelectric material will produce a strain in that material. The strain induced by such an electric field is given by the following expression:

$$\varepsilon_i = S_{ij}^{E}\sigma_j + d_{mi}E_m \qquad \text{Eq. 2}$$

where ε is the strain vector (m/m) and S is the elastic compliance coefficient (superscript E means that the value was taken at constant electric displacement) (m^2/N) which describes the strain produced in a material per unit of stress applied [30].

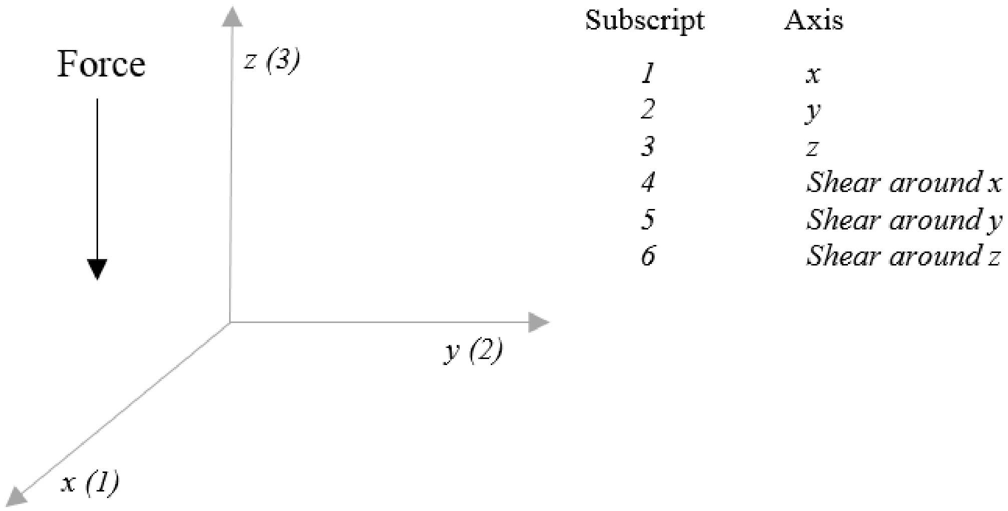

Figure 1 Piezoelectric constitutive equations subscript reference

Whereas the d_{mj} relates *strain* to output voltage, the voltage constant g_{ij} is an expression of the voltage produced by applied *stress* (V m/N). Typical *g* values include g_{33} (electric field generated per unit stress along polarization axis 3), and g_{31} (electric field generated per unit stress perpendicular to the polarization axis) [30].

The efficiency by which a piezoelectric material transforms mechanical energy into electrical energy is given by the unitless electromechanical coupling factor k_{ij}. The *i* and *j* indices refer to the directions of polarization and stress, respectively. Typical k_{31} and k_{33} conversion values for ceramics range from 30-75% [31].

A summary of the piezoelectric constants for several common piezoelectric materials is given in Table 1. Piezoelectric materials that are also ferroelectric (possess a permanent electric polarization) will lose piezoelectric and ferroelectric properties up above a critical temperature, known as the Curie temperature (or T_c). The Curie temperature is defined as the temperature above which ferroelectric materials become paraelectric, due to the rapid switching of the magnetic domains within the material. As a result, at and above the Curie temperature, piezoelectric materials do not exert a significant cumulative electric effect.

1.3.2 Applications of piezoelectric materials to water treatment

The potential generated by the direct application of mechanical energy may be harnessed to catalyze oxidation and reduction reactions of compounds vulnerable to electrochemical transformation. At sufficient material strains, redox reactions occurring at the piezoelectric – solution interface can split water molecules, leading to the formation of hydrogen radicals in reducing conditions and the formation of hydroxyl radicals in oxidizing conditions [32, 33]. The mechanism for water electrolysis depends on the nature of the electrode used to apply the electric current to water, as well as a variety of other chemical and physical parameters. J. Rossmeisl et al. (2005) proposed the following mechanism for water electrolysis using Pt and Au electrodes [34].

In an acidic environment:

$Cathode: 2H^+ + 2e^- \rightarrow H^* + H^+ + e^- \rightarrow H_2$ Eq. 3

$Anode: \quad 2H_2O \rightarrow HO^* + H_2O + H^+ + e^-$ Eq. 4

$\rightarrow O^* + H_2O + 2H^+ + 2e^-$ Eq. 5

$\rightarrow HOO^* + 3H^+ + 3e^- \rightarrow O_2 + 4H^+ + 4e^-$ Eq. 6

In an alkaline environment

$Cathode: \quad 2H_2O + 2e^- \rightarrow 2OH^- + H_2$ Eq. 7

$Anode: \quad 4OH^- \rightarrow OH^* + 3OH^- + e^-$ Eq. 8

$\rightarrow O^* + H_2O + 2OH^- + 2e^-$ Eq. 9

$\rightarrow HOO^* + H_2O + OH^- + 3e^-$ Eq. 10

$\rightarrow O_2 + 2H_2O + 4e^-$ Eq. 11

(Reproduced from [34])

As a potent reactive oxygen species (ROS), •OH is considered the strongest oxidant in water and thus is capable of oxidizing a wide variety of organic and inorganic compounds present in aqueous solution [35]. Similarly, the hydrogen radical (•H) is a strong reductant. Table 2 lists the oxidation potentials of a variety of common oxidants used in water treatment and the hydroxyl radical tops the list with an oxidation potential of 2.8V. Further, the reaction rate of hydroxyl radicals is widely cited to be near diffusion limited [35]. In conventional water treatment applications, the action of the hydroxyl radical is the basis for most advanced oxidation processes (or AOPs) such as ozonation or UV light when used in tandem with hydrogen peroxide (O_3/H_2O_2 or UV/H_2O_2).

The potential to spontaneously generate both hydrogen and hydroxyl radicals makes piezoelectrics excellent candidates for catalyzing powerful redox reactions relevant to water and wastewater treatment (Figure 6). The process of utilizing piezomaterials to induce redox reactions in solution is referred to as piezocatalysis or the piezoelectrochemical effect [36]. A detailed discussion of the underlying theory and mechanism(s) of piezocatalysis is given by Starr and Wang (2013) and Starr, Shi, and Wang (2012) [32, 33]. The capacity for a strained piezoelectric material to either donate electrons to or accept electrons from a compound depends on the magnitudes of the compound's Highest Occupied Molecular Orbital (HOMO) and Lowest Unoccupied Molecular Orbital (LUMO) energies with respect to the magnitude of the piezoelectric material's Valence Band (VB) and Conduction Band (CB) [33]. The Highest Occupied Molecular Orbital refers to the highest energy bond or lone electron pair in the compound. The HOMO is the source of electrons (therefore acting as a reductant in the redox reaction). Conversely, the Lowest Unoccupied Molecular Orbital (LUMO) refers to the compound's lowest energy antibonding orbital capable of accepting a pair of electrons (an oxidant). As a result, if the potential generated by the piezoelectric material is less than the energy of the HOMO, the substrate will undergo oxidation by donating electrons to the piezoelectric material. If the potential generated by the piezoelectric material is greater than the LUMO of the compound, then the LUMO will accept electrons from the piezoelectric material and undergo reduction. Starr and Wang (2013) reported that piezoelectric materials are capable of generating exceptionally high voltages (ranging from tens to hundreds of volts) when subjected to moderate or severe strain [33]. In circumstances where the piezopotential exceeds that of a standard hydrogen electrode (SHE) by more than 3 volts, it becomes thermodynamically favorable for many contaminants to undergo either oxidation or reduction reactions [33].

If the potential induced by the piezoelectric material is sufficiently high, then the rate at which a piezocatalyzed redox reaction will occur will be limited predominately by mass transfer kinetics. If migration and convective considerations are neglected, the maximum rate of electron transfer from the piezoelectric is equivalent to the rate of diffusion of the compound to the piezoelectric, resulting in a current density j given by:

$$j_i(x) = -n_i F D_i \frac{\partial C_i(x)}{\partial x} \qquad \text{Eq. 12}$$

where n_i is the number of electrons participating in the reaction, F is the Faraday constant, and D_i is the diffusion coefficient of the compound [33].

At a constant strain level, the piezoelectric will act as a capacitor in solution by slowing releasing its potential to the surrounding molecules [32]. The rate of change of the electric potential is given by the expression, below:

$$\frac{\partial V_p}{\partial t} = -\frac{w_x F \sum n_i D_i^{\frac{1}{2}} c_i f_i}{t^{\frac{1}{2}} \varepsilon_0 \varepsilon_{r,x} \pi^{\frac{1}{2}}} \qquad \text{Eq. 13}$$

where w_x is the width of the piezoelectric material in the x dimension, c_i is the bulk concentration of species i, f_i is a parameter taking on a value between 0 and 1, ε_o is the electrical permittivity of free space, and $\varepsilon_{r,x}$ is the relative permittivity in the x dimension, and t is time [32, 33].

Furthermore, piezoelectric activity in solution may by indirectly measured by monitoring hydrogen gas evolution or the presence of oxidized byproducts in solution. The build-up of a capacitative layer in the solution surrounding the piezoelectric or losses in the electric field present inside the piezoelectric also indicates piezocatalytic action [32, 33]. The rate at which H_2 gas evolves is a function of the level of strain experienced by the piezoelectric. Thus, the minimum strain necessary to drive a particular electrochemical reaction is given by the following expression:

$$S_{min,1} = \frac{\varepsilon_x \varepsilon_{r,x}(\varphi_{ElectrodeHOMO} - \varphi_{LUMO})}{2 w_x Y d_{xk}} \qquad \text{Eq. 14}$$

where Y is the Young's modulus of the material, w_x is the width of the piezoelectric material in the x dimension, d_{xk} are the piezoelectric moduli, $\varphi_{ElectrodeHOMO}$ is the electric HOMO potential of the electrode, and φ_{LUMO} is the electric LUMO potential of the water molecules in solution [32, 33]. Further, Hong et al. (2012) showed that agitated barium titanate microfibers rapidly degraded organic azo dyes by piezocatalysis [36].

The capacity for strained piezoelectric materials to catalyze redox reactions in aqueous environments is a tremendous opportunity for the development of novel, next-generation water treatment technologies that recycle waste mechanical energy at water utilities into useful electrochemical energy available for pollutant transformation and, ultimately, mineralization. Moreover, strategically designed piezoelectric materials could integrated into current treatment technologies to improve overall performance. For example, strategically implemented piezoelectric materials into membrane surfaces could inhibit biofouling at the membrane surface by periodically 'flexing' the membrane with the application of an electric potential (the indirect piezoelectric effect).

1.3.3 Composite materials blend the strength of polymeric materials with highly efficient piezoelectric inorganic phases

Piezoelectric ceramics such as barium titanate ($BaTiO_3$), lead zirconate titanate ($Pb[Zr_xTi_{1-x}]O_3$), and sodium niobate ($NaNbO_3$), among others, are distinguished by large strain constants (e.g. d_{31}, d_{33}) and electromechanical coupling factors (e.g. k_{31}, k_{33}) but poor material properties – such as brittleness and inelasticity. By contrast, polymers such as polyacrylonitrile (PAN) or poly(vinylidene difluoride) (PVDF) generally have much lower piezoelectric activity (d_{31} of PVDF is typically 20-30 pC/N) or none at all, but are resilient, strong, and flexible materials.

In developing the next generation of piezoelectric materials, numerous research teams have turned to piezoelectric ceramic-polymer composites, which offer the benefits of ceramic piezoelectric character without the pitfalls of material fragility. Among the first piezoelectric composites reported in the literature were PZT-epoxy composites developed by Furukawa et al. (1976) [37]. Numerous other groups have shown successes in optimization of similar ceramic-epoxy composites utilizing modified piezoelectric materials [38].

Recently, there has been a push to develop micro and nanoscale piezoelectric devices due to industrial needs for size reduction of piezoelectric sensors, capacitors, and actuators. To achieve this, novel one-dimensional piezoelectric components such as nanorods, nanotubes, or nanofibers which may exhibit properties drastically different than in bulk are being considered. One-dimensional piezoelectric nanostructures are capable of sustaining large bending strains which, in turn, could generate significant useable voltages. Properly engineered composites consisting of piezoelectric nanorods or nanowires could improve voltage output without necessarily sacrificing reaction site density. Accordingly, integrated networks of polymeric and ceramic hetero-nanostructures are now being developed. Such matrices have large surface area to volume ratios and can therefore be sites of high functionality and reactivity without needing large quantities of material.

The development of these one-dimensional piezoelectric nanostructures has been hampered by electromechanical limitations observed at sub-micron crystal grain sizes [27]. Specifically, decreasing piezoelectric response with decreasing grain size is well documented in the literature [27]. Yet, Tan et al. (2015) discussed the cumulative effects of domain wall density, back fields, and point defects on the piezoelectric and ferroelectric properties of micron and nano-scale barium titanate and found that a material’s piezoelectricity is highly influenced by the starting materials and processing conditions, but not necessarily determined by grain size [39]. Moreover, several groups have documented significant piezoelectric response of nanoscale piezoelectric materials, in spite of small grain sizes. Zhu and colleagues (2014) coated multiwalled carbon nanotubes with barium titanate [40]. Kang et al. (2015) used pulse-laser deposition to grow $Na_xK_{1-x}NbO_3$ (NKN) nanorod arrays on Nb-doped $SrTiO_3$ (Nb:STO) single crystal substrates [41]. Xu, Hansen, and Wang (2010) fabricated a piezoelectric nanogenerator utilizing PZT nanowire arrays to charge capacitors for LED power [42].

1.3.4 Overview of commercially available piezoelectric materials

Currently the largest share of the piezoelectrics market is held by lead zirconate titanates, which is comprised of a variety of combinations of lead zirconates and lead titanates given by the formula $Pb[Zr_xTi_{1-x}]O_3$. With an estimated market of more than 10 billion dollars worldwide, PZT is found in a variety of commercial and industrial products, such as sensors and actuator devices, multilayered capacitors, hydrophones, and others [43]. Indeed, many recent studies on the development of novel nanoscale piezoelectric materials have centered on PZT-based composites owing to its outstanding electromechanical properties (*PZT* d_{33} *= 300 – 700 pC/N;* k_{33} *= 0.50 – 0.75*) [44].

However, environmental and public health concerns with the continued production, deployment, and disposal of lead-based PZT ceramics has prompted a search for alternative non-toxic and environmentally friendly piezoelectric ceramics [43]. To this end, a variety of materials having the same general perovskite structure as PZT (thereby exhibiting similar piezoelectric properties) such as barium titanate ($BaTiO_3$, BTO), bismuth sodium titanate ($(Bi_{0.5}Na_{0.5})TiO_3$, BNT), and potassium niobate ($KNbO_3$) are being considered. Barium titanate is distinguished by its large piezoelectric properties (d_{33} = 149 – 490 pC/N; k_{33} = 0.49) compared to the other alternatives but is limited by a low Curie temperature of 125°C [39]. However, for piezocatalytic applications in aqueous media (e.g. water treatment), temperatures are unlikely to exceed 30°C, rendering the Curie temperature irrelevant. Barium titanate is also relatively simple to synthesize via hydrothermal chemical treatment on the nanoscale. Other BTO or BNT derived ceramics, such as BNT-BTO-Nb_2O_5, BNT-BTO-CeO_2 + La_2O_3, BNT-BTO-$MnCO_3$, and others may have the advantage of relatively large piezoelectric coefficients, but would be prohibitively resource intensive to synthesize systematically on the nanoscale.

1.3.5 Structure and characteristics of barium titanate

Barium titanate ($BaTiO_3$ or BTO) is synthetic ceramic discovered in 1941 that exhibits pyroelectric, ferroelectric, and piezoelectric characteristics. Many technologies have been developed that take advantage of the unique electrical properties of BTO, such as capacitors, transducers, accelerometers, dynamic random access memory, logic circuitry, and ultrasonic generators, and many others [45]. Barium titanate remains one of the most widely utilized piezoelectric materials today [46].

Like other titanates, BTO has a face-centered cubic perovskite lattice structure with a Pm3m cubic space geometry [47]. The Ti^{IV} ion occupies the body center of the lattice structure and is surrounded by octahedra of oxygen atoms. The Ba^{II} ions are located at the corners of the cubic cell. Individual lattice cells are linked at the corners to form straight rows throughout the crystal grain, which presents the possibility of a uniform electric dipole polarization throughout (Figure 9) [47].

Within the cubic lattice structure, barium titanate can assume four temperature-dependent crystalline phases. The four phases are: cubic, tetragonal, orthorhombic, and rhombohedral. The phases are distinguished by the degree of migration of the central titanium ion in the lattice (e.g. the magnitude of the Ti-O dipole). Ferroelectric and piezoelectric character is inversely proportional to temperature. For example, at temperatures at or exceeding barium titanate's Curie temperature (125° C) the cubic phase is stable. The cubic phase lacks piezoelectric or ferroelectric polarizability because the lattice becomes centrosymmetric and loses its internal dipole (the titanium ion is equidistant from each of the adjoining oxygen atoms in the octahedron). At lower temperatures, however, the Ti ion migrates toward one or more oxygen atoms in the octahedral which deforms the lattice and creates a dipole. The deformation becomes more exaggerated at lower temperatures which enhances BTO's ferroelectric and piezoelectric characteristics.

The first phase transition occurs at the Curie point whereby the central titanium ion migrates along the <100> crystallographic direction, which produces the tetragonal phase (space group P4mm) (Figure 8) [47]. The tetragonal phase persists until the temperature decreases below -5° C where the orthorhombic phase becomes stable (characterized by a deformation along the <111> axis – space group Amm) (Figure 8) [47, 48]. The final phase transition occurs at -90° C where the orthorhombic phase deforms along the <110> crystallographic axis and transforms into the rhombohedral phase (space group R3m) [47, 49]. At room temperature, BTO can assume either the cubic or tetragonal phase depending on crystallite characteristics like grain size, the prevalence of point defects, grain wall density, and back fields (discussed above) [39].

Compared to many commercially manufactured piezoelectric ceramics, the synthesis of barium titanate is relatively straightforward which makes it a versatile compound for developing novel composite materials. In industrial processes, barium titanate is synthesized via a solid state reaction between barium carbonate and titanium dioxide at high temperatures (>900°C). Alternatively, BTO may be synthesized by chemical precipitation and subsequently calcined for oxalate decomposition [50, 51]. Conventional routes to BTO synthesis generally produce particles 1-2 μM in diameter [51].

Hydrothermal synthesis has gained popularity as a method to synthesize nanoscale barium titanate crystallites. Depending on the reagents used, hydrothermal synthesis may also be more sustainable, economical, and environmentally friendly than conventional methods [51]. It is generally performed at lower temperatures (100 – 250°C) and requires little to no mechanical processing. However, alkaline hydrothermal synthesis of barium titanate often results in imperfect crystals with point-defects such as the substitution of aliovalent OH^- ions for O^{2-} ions in the lattice structures. The displacement of negative charge in the material must therefore be compensated by periodic cation vacancies throughout the structure to maintain charge neutrality. Several groups have cited these point defects and microstrains within the lattice structure as the reason why hydrothermal treatment generally produces cubic-phase BTO crystals at room temperature, although others have noted that hydroxyl point defects may be eliminated by increasing the hydrothermal treatment temperature above 150 °C [51] [52].

There are two proposed reaction mechanisms for the hydrothermal growth of barium titanate: the in-situ transformation model and the dissolution-precipitation model (Figure 10). The *in-situ* model assumes that dissolved barium or barium-hydroxide complexes react with solid TiO_2 to form a thin layer of $BaTiO_3$ on the surface of TiO_2 particles [50]. Additional free barium and barium hydroxide complexes must then diffuse through the BTO shell in order to reach more TiO_2 substrate, which eventually becomes rate limiting for the reaction [50]. In this model, it is generally assumed that there remains a fraction within the core of BTO crystals of unreacted TiO_2 [50].

The *dissolution – precipitation* model proposes that anhydrous TiO_2 particles must dissolve via hydrolytic attack to form aqueous hydroxytitanium complexes ($Ti(OH)_x^{4-x}$) which are capable of interacting with aqueous Ba^{2+} or $Ba(OH)^+$ ions to precipitate $BaTiO_3$ [50]. Nucleation may originate either on other TiO_2 particles (heterogeneous) or may form spontaneously in aqueous solution (homogeneous) [50]. Florentina Maxim et al. (2008) reported that the mechanism of barium titanate crystallization depends on the temperature of synthesis and reflects the properties of the titanium precursor [51]. At low temperatures (~90 °C), formation of BTO is limited to an in situ topotactic reaction which produces small pseudo-cubic single crystals of BTO [51]. The dissolution-precipitation model predominates around 110 °C and produces semi-spherical crystals [51]. At or above 200 °C, nucleation and growth of BTO crystals is rapid, and it has been reported that crystals form with a dendritic morphology [51].

Hydrothermal growth of tetragonal barium titanate has been reported using a wide variety of chemical precursors. Organometallic precursors such as titanium or barium titanium alkoxides have been widely used [36, 45, 53, 54]. Eckert et al. (1996) reported the synthesis of BTO by a facile reaction of barium hydroxide and titanium dioxide (Eq. 16 below) [50].

$$Ba(OH)_2 + TiO_2 \rightarrow BaTiO_3 + H_2O \qquad \text{Eq. 15}$$

This reaction yields barium titanate crystals of cubic morphology and phase [50]. Wu and colleagues (1999) found that the addition of KOH in the range of 1.0-3.0M can improve the tetragonal phase. However, the synthesis of one-dimensional BTO nanostructures generally requires the addition of a cosolvent or binding-ligand that promotes anisotropic crystal growth. Miki Inada et al. (2015) synthesized tetragonal barium titanate nanorods from $BaCl_2$ and $TiCl_4$ precursors, NaOH as the mineralizer, and ethylene glycol as an organic cosolvent [52]. Joshi and Lee (2005) reported the synthesis of single-crystalline barium titanate nanowires using $Ba(OH)_2$ and TiO_2 precursors and hydrothermally treated in the presence of ammonia at 170° C [55]. Yet, to date, to the best of our knowledge, incorporating organic co-solvents such as ethylene glycol to control the anisotropic growth of barium titanate crystals in a polymeric-ceramic composite has not yet been investigated.

1.3.6 Evaluation of support materials for composites

Because hydrothermal synthesis of barium titanate requires elevated temperatures (>100 ^{o}C) and pressures in an alkaline aqueous solution (pH > 13), the support material for barium titanate must be able to withstand harsh hydrothermal conditions. Although polymers are strong and versatile materials, they generally cannot tolerate the hydrothermal conditions needed to grow barium titanate. For example, we have attempted to hydrothermally process polystyrene (PS), poly(methyl methacrylate) (PMMA), and polyacrylonitrile (PAN) nanofiber mats in conditions required to grow tetragonal BTO crystals and all of the polymer mats were destroyed by the process.

Alternatively, graphitic carbon is chemically stable and resistant to concentrated acidic and alkaline conditions, as well as to corrosive gasses [56]. Pure carbon (in the form of powdered or granular activated carbon) is already widely utilized in water and wastewater treatment as a potent sorbent for problematic organic chemical contaminants. Specifically, electrospun carbon nanofibers (CNF) have attracted much attention in recent years due to their outstanding adsorptive properties while maintaining structural cohesiveness (able to be woven into a mat), a large surface area-to-volume ratio, and the capacity to be chemically functionalized to target removal of specific contaminants [57]. CNF-based filters are multifunctional and are highly capable at capturing particulate, colloidal, or dissolved contaminants by physical straining or sorption mechanisms. PAN nanofibers may be converted to cyclized graphitic carbon nanofibers (CNF) through high-temperature (>500^{o} C) pyrolysis in an inert atmosphere preceded by an air stabilization step. Finally, carbon has the advantage of being conductive, which broadens the scope of the electrical applications for carbon-piezoelectric materials for energy harvesting, transfer, or application.

1.4 Objectives and hypotheses

The overarching goal of this project is to develop innovative, nanostructured piezocatalysts capable of transforming waste mechanical energy into useful electrical energy for a range of environmental applications, including water and wastewater treatment. Specifically, the primary objective is to produce a nanofiber composite piezomaterial (such as carbon nanofibers with integrated barium titanate or CNF/BTO) that exhibits both the mechanical strength and the piezoelectric activity necessary to integrate such materials into environmental treatment applications.

To fabricate this material, we will rely on electrospinning. This technique allows for the tailored control of three-dimensional nanofiber networks ideal for reactive coatings or filtration applications. Electrospinning is also ideal for composite materials because it allows for the inclusion of organic and inorganic building blocks into the precursor sol-gel. Physical characteristics of electrospun nanofibers (such as diameter, strength, and surface character) may be altered through control of electrospinning parameters such as the applied voltage per needle tip-to-collector distance (kV/cm), sol-gel flowrate, needle gauge, collector type, ambient temperature, and humidity. Furthermore, nanofiber mats are robust for post-processing like hydrothermal treatment to continue to modify composite nanostructure. This work builds on our experience with carbon-based nanofibers, for which we have used a variety of approaches to make flexible, mechanically robust materials while also using porogens to increase surface area [57]. Finally, recent developments in nanomanufacturing (like the Elmarco Spider) for needless electrospinning have overcome limitations in the production rate of nanofiber mats such that scale-up to industrially/commercially viable levels can be attained.

We envision that this composite material can be used in contaminant removal and degradation studies. Electrical potential generated by the composite under mechanical stress will be used to split water and generate reactive oxygen species (ROS). These ROS will then be available for disinfection of microbial pathogens as well as oxidation of emerging organic and inorganic pollutants. Thus, possible applications range from antimicrobial surfaces or reactive filtration via chemical oxidation. We note that it would also be possible to integrate such materials with a sustainable power supply, where potential could be applied to cause such materials to deform. Such physical agitation may be useful in slowing colloidal fouling of membrane surfaces.

Specific objectives related to the fabrication and characterization of this piezoelectric composite include:

Objective A: Demonstrate production of carbon nanofibers (CNF)-barium titanate (BTO) composite through hydrothermal treatment of polyacrylonitrile (PAN)-based CNF loaded with nanoscale titanium dioxide (TiO_2).

Objective B: Identify how synthesis (e.g. TiO_2 loading) and hydrothermal treatment conditions (e.g. temperature and duration) influence strength of the CNF support and formation of tetragonal BTO, two factors critical to the overall performance of these composites as a piezoelectric material.

Objective C: Determine how the use of crystal capping agents (e.g. ethylene glycol) can be used to alter the BTO morphology and enhance piezoelectric activity.

Objective D: Conduct proof-of-concept studies where BTO nanomaterials are used as a sustainable power supply for the electrochemical degradation of model aqueous pollutants.

In developing optimized CNF/BTO composites, we hypothesize that:

- Piezoelectric response of the composite materials will be a function of the predominant crystalline phase of the embedded $BaTiO_3$ crystals. Specifically, increasing distortion away from the cubic (non-piezoelectric) crystalline phase toward the tetragonal (piezoelectric) phase will improve overall electrical response to mechanical agitation.

- Piezoelectric response will increase with the mass loading of $BaTiO_3$ crystals in the nanofiber matrix. It is suspected that, under identical synthesis conditions, composite materials having more embedded $BaTiO_3$ crystals will output more electric power than composites with lower mass loadings.

- $BaTiO_3$ crystal anisotropy will improve overall piezoelectric performance. In particular, $BaTiO_3$ crystal morphologies capable of supporting large bending strains (i.e. ‘rods’) will generate larger potentials than composites having spherical or cubic crystal morphologies. It is suspected that $BaTiO_3$ rods will consequently be more effective redox catalysts than cubic or spherical crystals.

These hypotheses will be tested through a research plan that couples the systematic synthesis of piezoelectric composites with characterization to quantify standard performance metrics for piezoelectric materials.

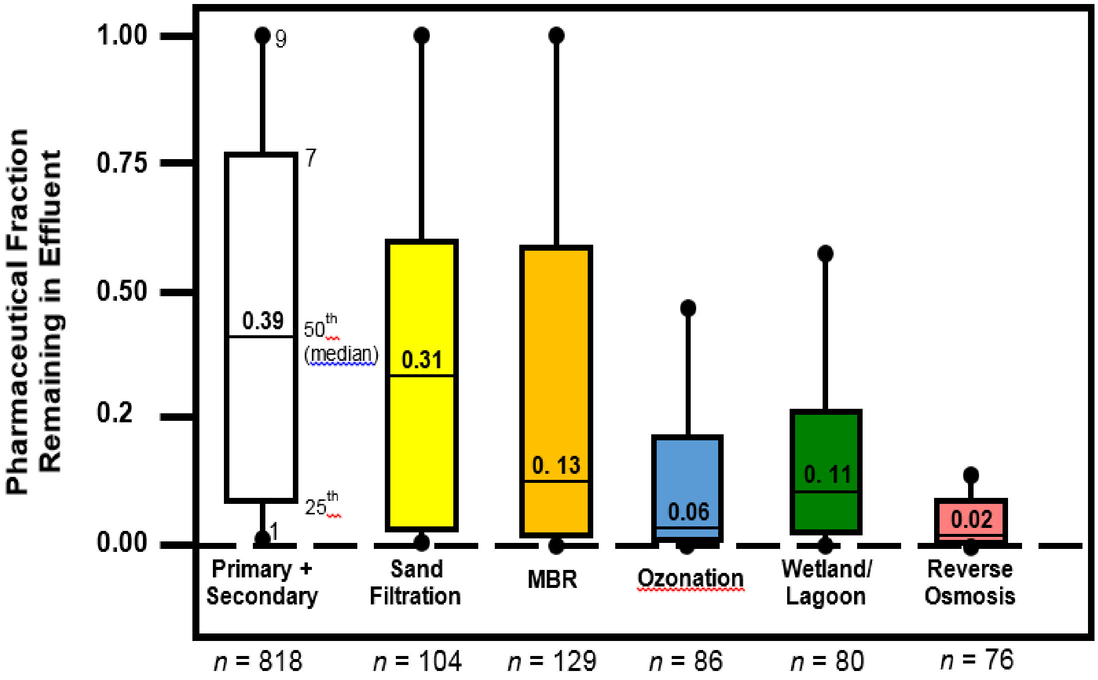

Figure 2 Fraction of pharmaceuticals remaining in wastewater effluent following various wastewater treatment processes; data compiled from Oulton, Kohn, and Cwiertny (2010).

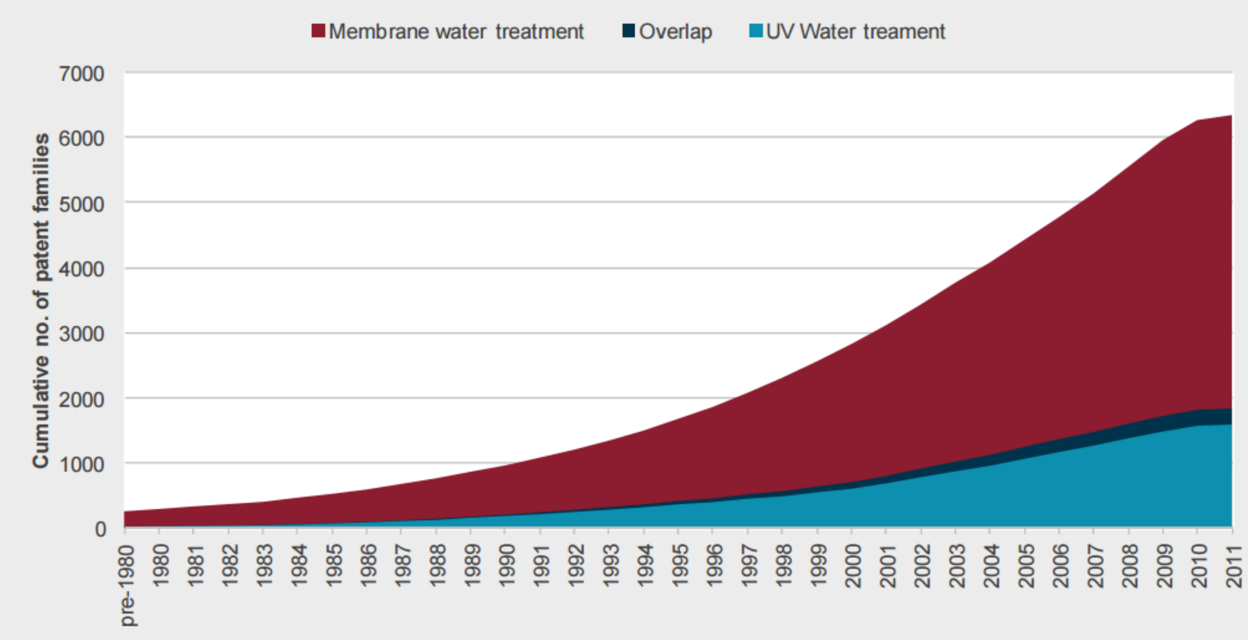

Figure 3 Cumulative patents filed for membrane and UV water treatment related technologies. Reproduced from Iliev, Ilian and Helena van der Vegt. (2012).

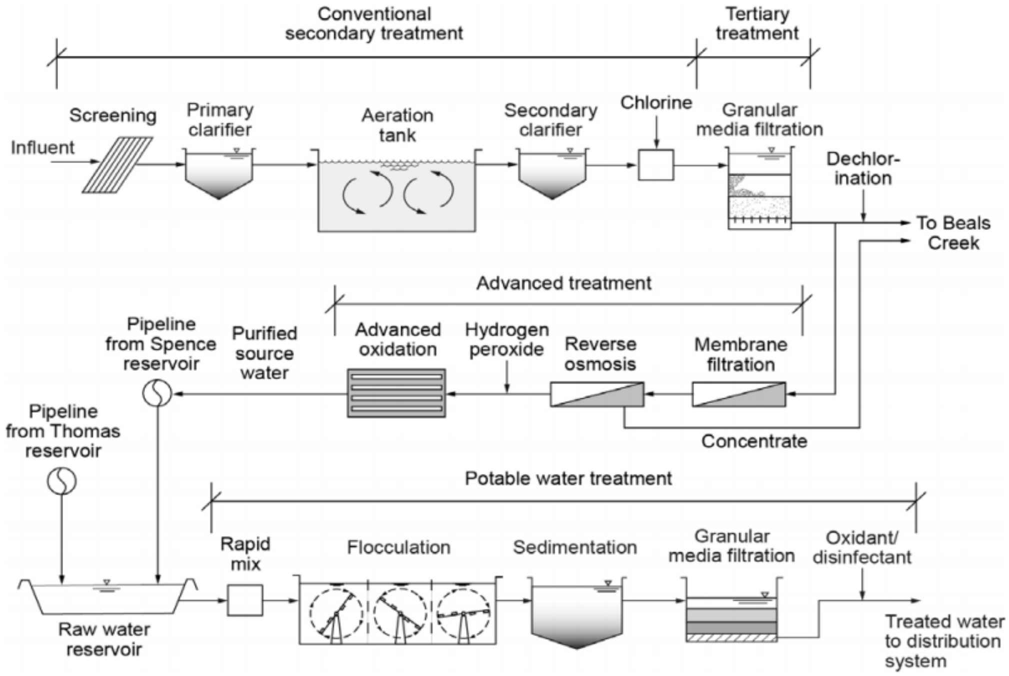

Figure 4 Flow Process Diagram of DPR Facility in Big Springs, Texas. Reproduced from Tchobanoglous, George. *Direct potable Reuse: A Path Forward: 15th Annual Education Seminar Central States Water Environment Association* (2011).

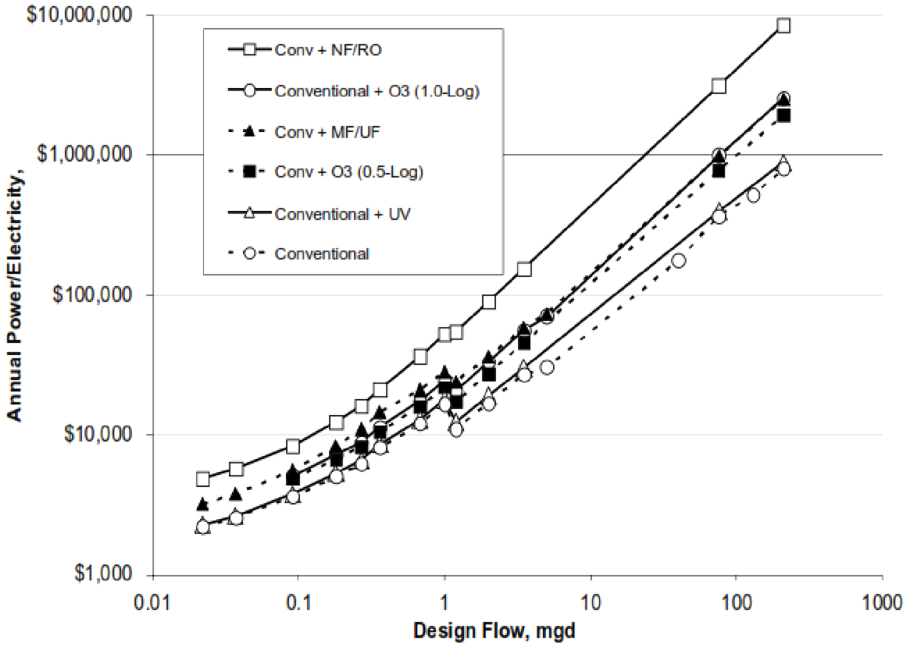

Figure 4 Advanced treatment technologies consume more electricity than conventional approaches. Reproduced from Raucher et al. *Risks and Benefits of Energy Management for Drinking Water Utilities* (2008).

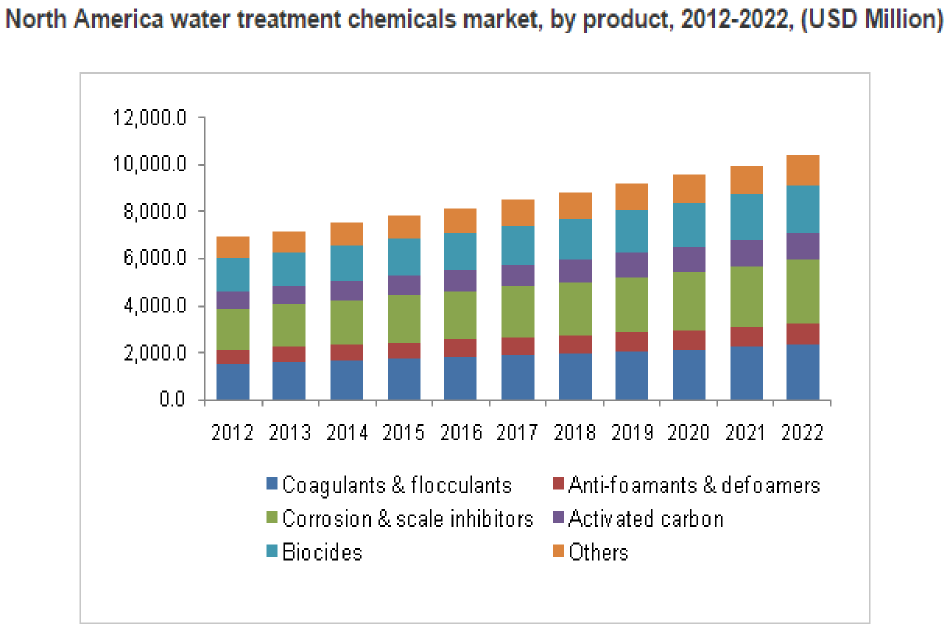

Figure 5 Market for water treatment chemicals is steadily growing. Reproduced from Grand View Research. Water Treatment Chemicals and Technology Market Analysis by Product (Pumping Systems, Membrane Separation, Chemicals) and Forecasts, 2015 To 2022 (2016).

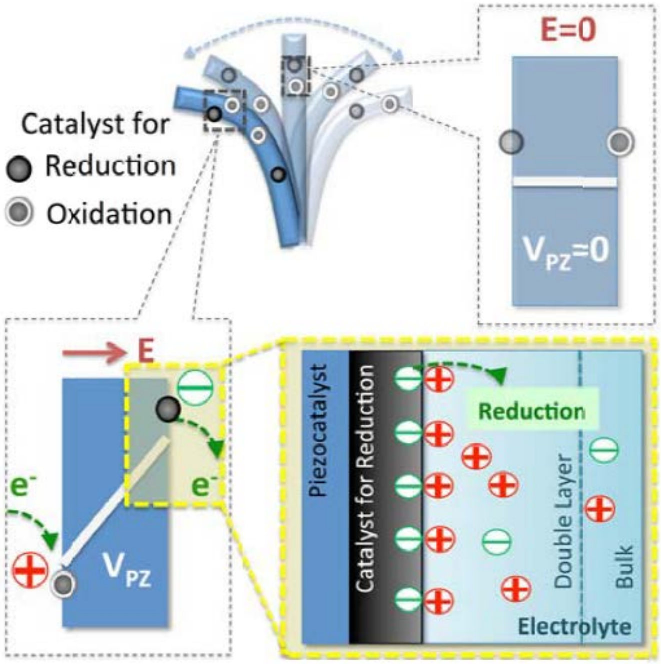

Figure 6 Piezoelectric voltage and electricity generation in strained state and non-strained state. Material polarization and an internal electric field is generated under dynamic strain. Charge separation and redox reactions are facilitated by surface catalysts. In a solution, a double layer is developed at the catalyst surface, at which capacitive charging and electron transfer events occur.

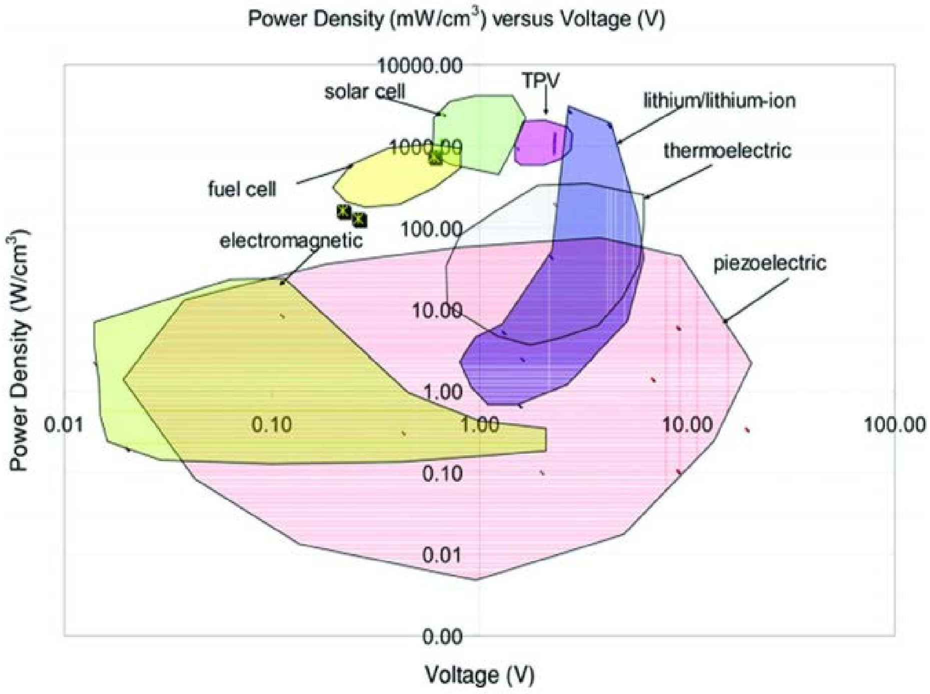

Figure 7 Power density vs. Voltage Plot of Select Regenerative Power Supplies. Reproduced from Cook-Chennault, Thambi, and A.M Sastry (2008).

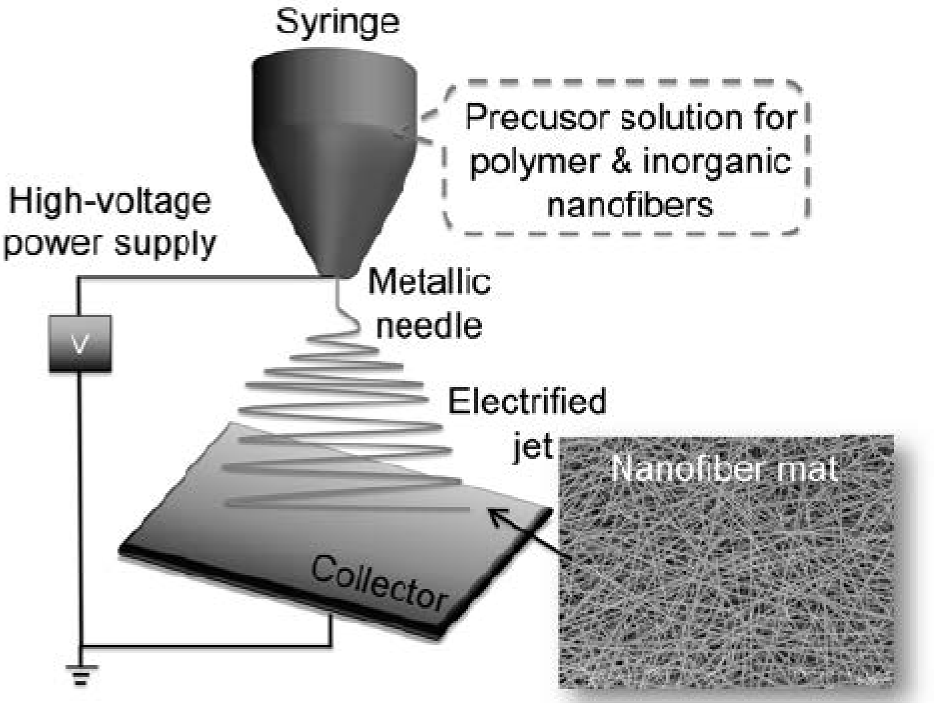

Figure 8 Electrospinning Schematic

Table 1 Summary of piezoelectric coefficients for common piezoelectric materials

System	Composition	T_c (°C)	d_{33} (pC/N)	Dielectric Constant *(K)*	k_{33}	References
PZT	$Pb[Zr_xTi_{1-x}]O_3$	195 - 370	100-700	1400 - 5000	0.69	[44, 58, 59]
BTO	$BaTiO_3$	130	149-260	1400	0.49	[43, 60, 61]
BNT	$(Ba_{0.5}Na_{0.5})TiO_3$	310	64	302.6		[43]
ZnO	ZnO	NA	11-12	11	0.48	[60, 62]
PVDF	PVDF	135	(-20) – (-33)*		0.19	[27, 60, 63]
$(K,Na)NbO_3$	$(K_{0.5}Na_{0.5})_{1-2y}AE_yNbO_3$ AE = Mg, Ca, Sr, Ba	310	95	500		[43]
Quartz	SiO_4	573	2.3 (d_{11})	4.5		[27, 64]

**electromechanical coupling coefficient of PVDF is positive in the 31 plane;* $d_{31(PVDF)} = 20$

Table 2 Oxidation potentials of oxidants typically used in water treatment [35]

Oxidant	Oxidation potential (V)
Ozone	+2.07
Hydrogen Peroxide	+1.78
Permanganate	+1.67
Chlorine Dioxide	+1.50
Hypochlorous Acid	+1.49
Chlorine Gas	+1.36
Oxygen	+1.23

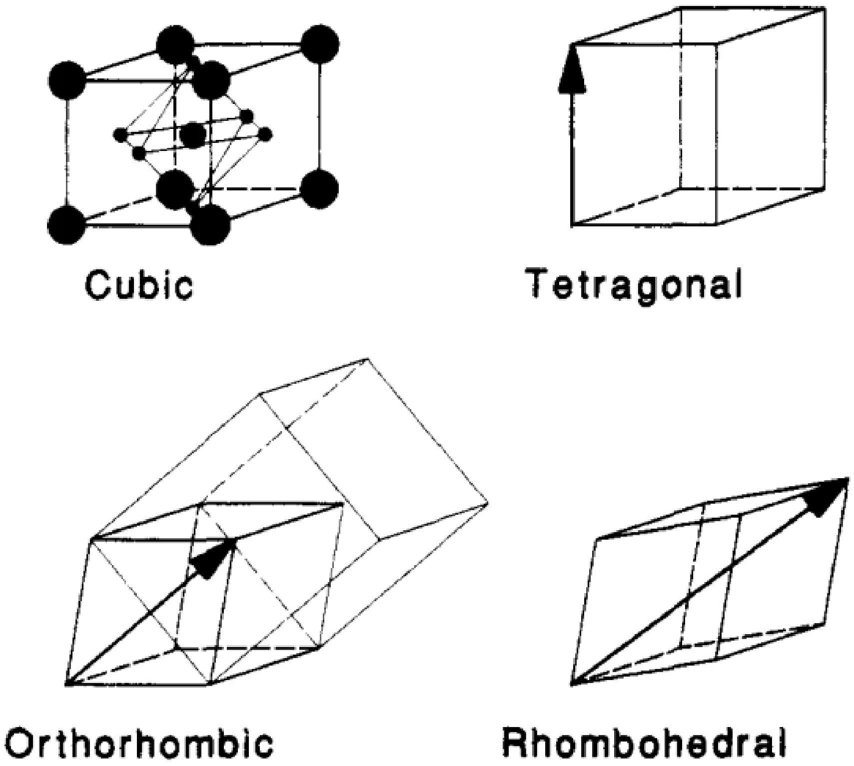

Figure 9 Crystalline phases of barium titanate. Reproduced from Kwei et al. (1993).

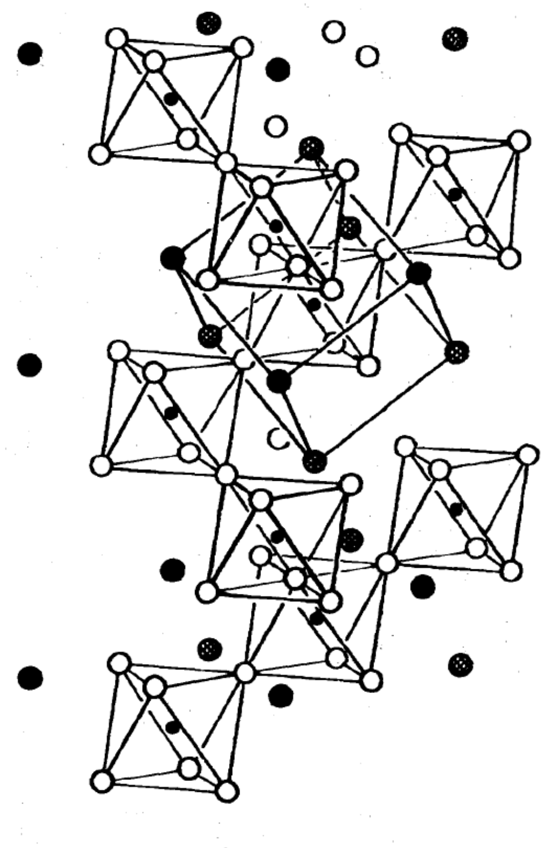

(b) Cubic

Figure 10 Lattice geometry of cubic barium titanate. Reproduced from Evans Jr., H.T. (1953).

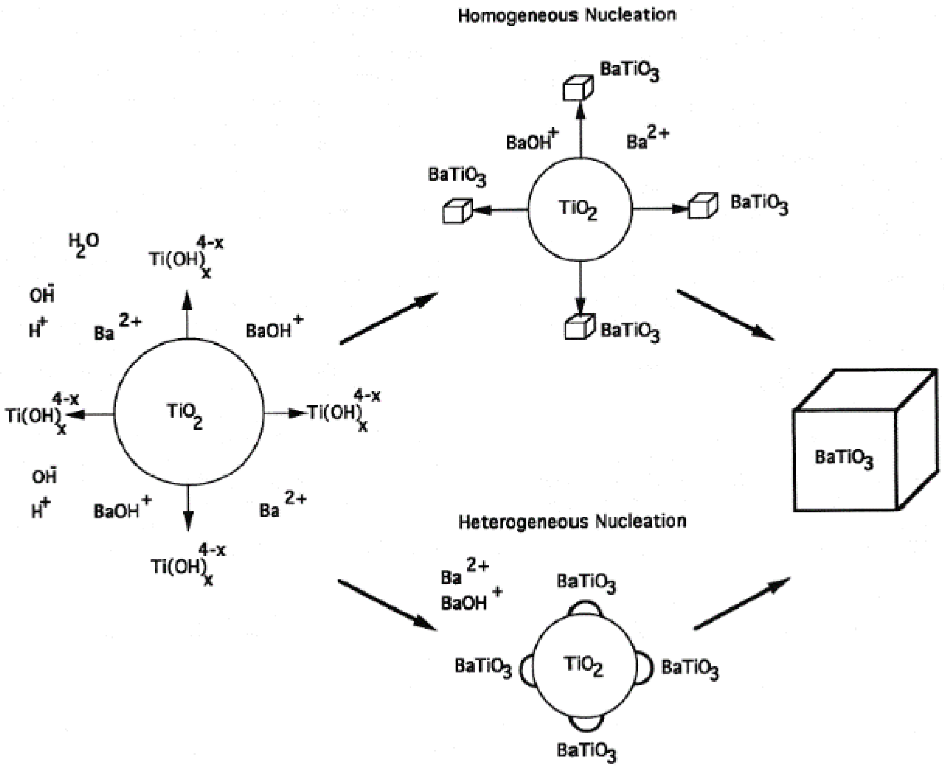

Figure 11 Homogeneous and heterogeneous hydrothermal nucleation mechanisms of barium titanate. Reproduced from Eckert et al. (1996).

CHAPTER 2 MATERIALS AND METHODS

2.1 Electrospinning of polymer nanofiber composites

All reagents were used as received. Carbon nanofibers (CNF) were used as the nanofiber scaffolding to support the piezoelectric barium titanate (BTO) crystals and were synthesized via an electrospinning with subsequent carbonization process. Optimized CNF/BTO composite recipes were investigated by preparing precursor sol-gels consisting of 8.0% (by total solution mass) polyacrylonitrile (PAN, Sigma-Aldrich, Avg. MW 150,000), 0 – 4.0% phthalic acid (hereafter "PTA"; Sigma-Aldrich, ≥99.5%), and 0 - 15.0% Degussa P25 Titanium dioxide (Sigma-Aldrich, ≥99.5%) (hereafter "P25") nanoparticles (mean diameter 25 nm). Sol-gels were typically prepared in 3 mL batches. P25 nanoparticles were incorporated into the sol-gel as seed crystals for the growth of embedded barium titanate crystals in the carbon nanofiber matrix.

PTA and P25 were dispersed in dimethylformamide (DMF, BDH Chemicals, ≥99.8%) by sonicating the mixture continuously in a Fisher Scientific Ultrasonicator (42 kHz, 100W output). We also investigated three common surfactants as nanoparticle dispersing agents: sodium dodecyl sulfate (SDS), tetrabutylammonium bromide (TBAB), and centrimonium bromide (CTAB), as well as phthalic acid (PTA), and terephthalic acid (TPTA). To test the effectiveness of these surfactants in promoting P25 dispersion, settling or sedimentation tests were performed with P25 suspensions in DMF. Dispersivity was assessed by collecting absorbance scans of each of the suspensions in a Genesys 10uv Scanning Spectrophotometer at wavelengths between 300 – 700nm.

Following ultrasonication, powdered PAN polymer was added to the sol-gel and the mixture was thermally mixed for two hours at 60 °C (700 rpm) in an Eppendorf Thermal mixer. The sol-gel was loaded into a Luer-lok tip BD 10 mL syringe fit with a 23G needle and electrospun onto a rotating drum (500 rpm) covered in aluminum foil. The sol-gel flow was held steady at 0.5 mL/h using an NE-300 syringe pump from New Era Pump Systems, Inc. A constant electric field of 12.5 kV was applied between the needle tip and the edge of the collector drum (10 cm) by an Acopian High Voltage Power Supply. During synthesis, the temperature and humidity were held between 20-30^{o} C and 20-25% RH, respectively.

The abbreviation scheme for denoting the resulting composite mats will be denoted in the general format: PAN/(wt.%)P25/(wt.%)PTA. Accordingly, PAN/6.0P25/2.7PTA refers to the electrospun polyacrylonitrile nanofiber mat (8.0 wt.% PAN), 6.0 wt.% P25, and 2.7 wt.% PTA (weight percent is assigned per initial sol-gel mass including solvent). CNF/6.0P25 refers to the carbonized composite mat with 6.0 wt.% P25. Carbon nanofiber abbreviations will exclude PTA due to the sublimation of the PTA out of the mat during pyrolysis.

2.2 Carbonization of composite mats and optimization of material strength

Electrospun PAN/P25/PTA nanofiber mats were removed from the aluminum foil and placed directly in an MTI KJ Group Tube Furnace (OTF-1200X). Carbonization proceeded in two steps. First, the fibers were stabilized in an air atmosphere at 250 ^{o}C. After stabilization, the mat was pyrolyzed in an N_2 atmosphere for one hour. The relationship between pyrolysis temperature and composite mat flexibility was explored by systematically varying the pyrolysis temperature in 150^{o} C increments between 450^{o} C and 1200^{o} C (at a heating rate 5^{o} C/min). Resulting CNF/P25 mats were compared qualitatively for strength (i.e., mats were flexed manually in the lab and fracture points were determined).

2.3 Hydrothermal treatment of CNF mats to produce barium titanate

Conversion of the embedded P25 to barium titanate (BTO) was accomplished using two methods of hydrothermal treatment. These will be referred to as either "two-stage" or "one-pot" alkaline hydrothermal synthesis. Both methods are described below.

For the two-stage method, approximately 50 mg of the CNF/6.0P25 composite mat was added to 40 mL of 10 M NaOH (Acros Organics, ≥ 97%) (prepared in Milli-Q DI water) and sealed in a 100 mL Teflon-lined autoclave. Autoclaves were placed in an oven at 150 ^{o}C to convert the embedded P25 nanoparticles into a mixture of hydrogen and sodium titanate ($A_2Ti_nO_{2n+1}$ for n = 2, 3, 4 and A = Na, H) nanorods [65]. The influence of hydrothermal treatment duration on sodium titanate (hereafter "NaT") formation and crystal morphology were explored by treating CNF/6.0P25 composites in 10 M NaOH for 4, 8, 16, and 24 hours. Resulting CNF/NaT composites with desired crystal morphology (i.e., relatively uniform NaT crystal dispersion) were subsequently treated in 0.1 M $BaCl_2 \bullet 2H_2O$ and 0.2 M NaOH at 150 ^{o}C in a simple ion exchange reaction to convert NaT into BTO. This ion exchange reaction was conducted over 2, 6, 10, 16, and 28 hours to assess the dependency of BTO conversion on treatment time and to qualitatively map the effects on BTO crystal morphology. Composite mats produced from both the first and second stage of alkaline hydrothermal treatment were washed with 0.1 M HCl followed by a wash with deionized water (DI) and then dried before the next stage of processing.

One-pot hydrothermal synthesis of the CNF/P25 composites was carried out in 0.31 M $Ba(OH)_2$• $8H_2O$ (Sigma-Aldrich, ≥ 98%) to achieve direct in-situ conversion of the embedded P25 into BTO. The one-pot synthesis proceeds via the chemical reactions given in Equation 16.

Once again, reactions were carried out for various treatment times and temperatures to explore the effects on BTO crystal development. In each case, 50 mg of the CNF/TiO_2 mat was added to 40 mL of 0.31 M $Ba(OH)_2$ • $8H_2O$ (prepared in Milli-Q DI water) and sealed in a 100 mL Teflon-lined autoclave. To explore the effects of treatment temperature, autoclaves were placed in the oven at temperatures ranging in 20 ^{o}C increments between 80 ^{o}C and 260 ^{o}C (totaling ten samples) for 24 hours. At the end of the heating cycle, reactors were extracted and quenched under flowing tap water. The hydrothermally treated CNF composites were removed and washed sequentially with 0.1 M HCl and then DI water until no pH change of the wash solution was observed. After washing, the composite material was then dried.

We note that the "one-pot' alkaline synthesis was found to produce CNF/BTO composite mats with superior mechanical and piezoelectric properties to the two-stage method, and therefore was used for further synthesis studies. For example, this approach was used to assess the impacts of BTO crystal density on electromechanical properties. Specifically, PAN composite nanofiber mats of 1.0 to 15.0 wt.% Degussa P25 TiO_2 (per total sol-gel mass) were electrospun, carbonized, and subsequently hydrothermally treated using the "one-pot" synthesis approach (i.e., in 0.31M $Ba(OH)_2$ • $8H_2O$ at 220 ^{o}C). These mats were cooled and washed according to procedures above.

2.3.1 Use of ethylene glycol to promote anisotropic BTO growth

Ethylene glycol (Fisher Chemicals, ≥ 99%) (hereafter "EG") was added to hydrothermal reactors at various volumetric fractions to promote the anisotropic growth of BTO crystals on the CNT matrix. Generally, 50 mg of the CNF/6.0P25 composite was added to 0.31 M $Ba(OH)_2 \cdot 8H_2O$ with a volumetric fraction of ethylene glycol ranging between 5 – 20% (Table 3) and reacted at 200^o C for 24 h. To investigate how treatment time and temperature influenced BTO growth in the presence of EG, select EG-containing reaction solutions were treated for various lengths of time and at different temperatures (specific conditions given in Table 3).

Table 3 Ethylene Glycol synthesis study with varied treatment time(s) and temperatures

Composite	EG Volume Fraction	HT Temperature (^oC)	HT Time (h)
CNF/6.0P25	5%	200	12
			24
			48
CNF/6.0P25	7.5%	180	24
		200	24
CNF/6.0P25	10.0%	140	12
			24
		160	12
			24
		180	
		200	
		220	
CNF/6.0P25	11.0%	200	
CNF/6.0P25	12.5%		
CNF/6.0P25	15.0%		
CNF/6.0P25	17.5%		
CNF/6.0P25	20.0%		

2.3.2 Hydrothermal synthesis of unsupported barium titanate nanorods

Unsupported BTO nano- and microcrystals were also synthesized separately from the carbon nanofiber according to a method analogous to the 'one-pot' synthesis procedure reported above for converting embedded P25 to BTO in the CNF/BTO composites. P25 nanoparticles were added to 0.31 M $Ba(OH)_2 \cdot 8H_2O$ at a molar ratio of 1:2 P25: $Ba(OH)_2 \cdot 8H_2O$ into sealed steel 100 mL Teflon-lined autoclaves and treated at 200 ^oC for 24h. Solids were separated from the resulting slurry by vacuum filtration and collected on PVDF membranes (average pore size 0.22μM). The retained solids were subsequently washed with 0.1 M HCl and DI water and dried overnight at 50 ^oC.

2.4 Material characterization

Samples prepared at each stage of synthesis (electrospinning, carbonization, and hydrothermal treatment) were characterized to assess material properties.

2.4.1 Assessments of nanofiber physical characteristics

Nanoscale physical characteristics of the composites were assessed by imaging with a Hitachi S-4800 Scanning Electron Microscopy (SEM). Pieces of the composite mats (approximately 0.5 cm by 0.5 cm) were placed on Al sample stubs and attached with carbon tape. Samples were sputter-coated with Au to allay the effects of charging while operating the SEM. Elemental maps of Ba and Ti in various composite swatches were obtained with energy-dispersive X-ray spectroscopy (EDS) with SEM. Histograms of average polymer and carbon nanofiber diameter were compiled from measurements (n=100) obtained with ImageJ software of the SEM images. Specific surface areas (m^2/g) of the composite carbon mats were measured with a Nova-4200 BET Surface Area and Pore Size Analyzer. CNF composites were degassed at 150^o C each for a minimum of three hours.

2.4.2 X-Ray diffraction analysis

Powder diffraction patterns were acquired from a Tungsten filament Miniflex II X-Ray Diffractometer under Co Kα radiation. Pattern identification was performed using reference Crystallographic Information Files (.cif) from the American Mineralogist Crystal Structure Database. Tetragonal phase barium titanate, anatase, and rutile patterns were identified with AMCSD reference patterns 0018579, 0019093, and 0019092, respectively. The locations of BTO diffraction lines, intensities, d-spacings, and Miller indices are provided in Table 4. Crystal lattice cell parameters (a, b, and c) were estimated from the fitted peak profiles of the powder reference patterns. In the pure cubic phase, all lattice cell lengths are equal (a=b=c) and therefore the lattice ratio c:a = 1.0. By contrast, it is generally accepted that the pure tetragonal phase has a lattice ratio c:a ~ 1.01 (lattice distortion along a single edge of the lattice cell [001]) [49, 52]. The stability of the tetragonal phase is also evident from the characteristic splitting of the [200] peak in the XRD pattern to register both [002] and [200] diffraction lines at 52.85 2θ and 53.18 2θ, respectively.

Table 4 Powder Diffraction Pattern Data of Tetragonal $BaTiO_3$

Diffraction line (2θ)	Intensity	d-spacing	H	K	L
25.72	7.07	4.0222	0	0	1
25.86	13.66	3.9988	1	0	0
36.79	100	2.8358	1	0	1
36.90	48.88	2.8276	1	1	0
45.52	19.96	2.3132	1	1	1
52.85	13.78	2.0111	0	0	2
53.18	27.01	1.9994	2	0	0
66.19	5.15	1.6389	1	1	2
66.41	10.39	1.6341	2	1	1
78.27	7.54	1.4179	2	0	2
78.54	3.75	1.4138	2	2	0
84.07	1.42	1.3364	2	1	2
101.37	2.24	1.1566	2	2	2

Mean crystallite size τ_{avg} was estimated using the Scherrer equation (Equation 17).

$$\tau_{avg} = \Sigma\left(\left(\frac{k\lambda}{FWHMcos\theta}\right)\left(\frac{peak\ area}{total\ peak\ area}\right)\right) \qquad \text{Eq. 16}$$

where *k* (the Scherrer constant) was assumed to be 0.9 (for spherical crystallites) and the wavelength (λ) was 1.789 nm (Co). The full width at half maximum values for all barium titanate peaks from 20 – 85 2θ were determined by automatic measurements analyzed by MDI Jade crystallographic analysis software.

2.4.3 Electromechanical testing

Testing for electromechanical properties of the composite materials was conducted by applying strain to the materials via a speaker and registering electrical signals. Output voltage from the composite mats was measured as a function of applied bending strain using a cantilever – oscilloscope setup. CNF/BTO composites were sandwiched between two brass sheets (51 mm x 16 mm x 100 µm) which served as the bending cantilever used to modulate applied strain. Samples were cut into 20 mm x 12 mm swatches and affixed to the bottom brass contact with double sided copper tape. Polyimide (Kapton) tape was used to electrically insulate the brass contacts from one another. Each brass contact was connected with a 24 gauge wire to a breadboard that ultimately led to the oscilloscope (Lecroy, Chestnut Ridge, NY) which measured the output electrical signals from the composite mat [66].

The custom cantilever was mounted atop of a subwoofer speaker. Cantilever stain was determined by measurements recorded by an ACC103 accelerometer (OMEGA Engineering, Inc., Stamford, CT) and a GoPro Hero3+ (GoPro, Inc. San Mateo, CA) which were attached to the surface of the speaker. The camera recorded the arc of the cantilever as it was flexed by the speaker, which was overlaid by a circle in post-processing to determine the cantilever's arc of curvature, R, given the thickness of the cantilever, t. Cantilever strain was therefore calculated by Eq. 18.

$$Strain\% = \frac{(t/2)}{R}\ x\ 100 \qquad \text{Eq. 17}$$

LabVIEW VI was used to deliver a sinusoidal wave to the speaker at 10Hz frequency. The current generated by the composite mats was calculated by measuring the voltage drop (V) across the total resistance system (Eq. 19) and converting the total resistance to current with Ohm's law (Eq. 20) [66].

$$R_T = \frac{R_I R_L}{R_I + R_L} \qquad \text{Eq. 18}$$

$$I_{total} = \frac{\mathrm{V}}{R_T} \qquad \text{Eq. 19}$$

where R_I is the internal resistance of the oscilloscope (10 MΩ) and R_L is an added load resistor which, when added to the internal resistance, generated total resistances of 0.5, 0.9, 1.7, 3.3, 6.88, or 10 MΩ. Ohm's Law was also used to determine power (P) [66].

$$P = \frac{V^2}{R_T} \qquad \text{Eq. 20}$$

2.5 Electrolytic degradation of sodium orange II dye

For preliminary experiments of piezocatalytic degradation of model water treatment contaminants, Sodium Orange II dye, also known as Acid Orange 7, (sodium (4-(2-Hydroxy-1-naphthylazo)) benzenesulfonic acid) (hereafter 'AO7') was used as a representative organic contaminant. Electrolytic decolorization of AO7 was performed in batch by applying 2.5V and 1.0V via Pt electrodes for three hours to stirred 50mL solutions of 10µM AO7 in 10mM potassium phosphate buffer. Samples were extracted every 30 minutes and absorbances were taken in a Genesys 10UV Scanning Spectrophotometer both for the λ_{max} ~490nm and solution absorbance across 200 – 700 nm. Solutions were left exposed to the light for the duration of the experiments. The pH was measured at the beginning and conclusion of the experiment.

2.6 Batch sonication experimental design

Preliminary batch studies meant to demonstrate the applicability of piezocatalysis to degrading model water treatment contaminants were performed with suspended commercial and laboratory-developed BTO crystals. The experimental set-up followed the procedures outlined by Hong et al. (2012) [36]. As above, AO7 was used as the model organic contaminant. In the commercial control batch experiments, tetragonal barium titanate nanopowder (U.S. Research Nanomaterials, Inc., 200nm, 99.9%) was pre-sonicated for 30 seconds in 10 mL of deionized water to disperse the nanoparticles. The sonicated mixture was added to a solution of 10 μM AO7 which was prepared in 10 mM potassium phosphate buffer (pH 7) to a total solution volume of 50 mL. To test the laboratory-developed barium titanate nanocrystals, unsupported tetragonal barium titanate nanocrystals synthesized with 6.5 vol.% EG were added at various mass loadings (0.1 g/L and 0.5 g/L) in the same manner as above. Nitrogen gas was bubbled through the sealed reactor for ten minutes to sparge the solution of oxygen. Afterward, the gas line was withdrawn from the solution such that it simply supplied nitrogen gas over-pressure to prevent oxygen from reentering the reactor. The solution of BTO and AO7 was sonicated continuously in a Bransen 42 kHz sonicator continuously for three hours. Light exposure and temperature were controlled by keeping the sonicator covered throughout the experiment and by periodically adding ice to keep the temperature between 0 – 15^{o} C. Samples were withdrawn every 20 minutes and centrifuged twice at 13,000 rpm for 10 minutes to remove any freely suspended BTO. Samples were then analyzed in a Genesys 10UV Scanning Spectrophotometer both for the solution absorbance at 490 nm (corresponding to the absorbance maximum for Orange II dye) and solution absorbance across 200 – 700 nm to examine for the presence of other peaks indicating the formation of potential transformation products. The pH was measured prior to and following the conclusion of the experiment. Calibration standards (from 0.625 to 20 μM) of Orange II were prepared and used to determine time-dependent Orange II concentrations in the batch reactor.

Figure 12 Experimental set-up of batch sonication experiments

CHAPTER 3: PIEZOCATALYTIC DYE DEGRADATION IN MODEL BATCH SYSTEMS

3.1 Batch sonication experiments with suspended barium titanate nanocrystals

The capacity of barium titanate (BTO) nanoparticles to piezocatalytically degrade organic contaminants was demonstrated in idealized model systems. These systems involved agitation of BTO nanoparticles via sonication. The target for these degradation studies was the model organic pollutant, Sodium Orange II dye (hereafter 'AO7'), which is widely used in textile industries. AO7 was selected for its ease of analysis via direct UV/visible light absorption (pKa = 10.65, λ_{max} = 482nm, ε_{molar} = 18.7 mM^{-1} cm^{-1}) [67, 68]. At neutral pH, AO7 dissolves to form an anion in solution with the negative charge located at the sulfonate group, with the similarly nucleophilic azo bond as the chromophore (Figure 12).

Both commercially available BTO nanoparticles and synthetic BTO nanocrystals synthesized in-house were tested for catalytic activity, and their reactivity was explored at various mass loadings. To compare the piezocatalytic activity between suspended BTO nanocrystals and those embedded in the nanofiber composite, materials tested in batch were grown using the same hydrothermal method developed specifically for synthesizing embedded BTO nanoparticles with a carbon nanofiber support (method development is detailed in Chapter 4).

We expected that tetragonal BTO crystals would be catalytically active in solution by supplying the electrical power necessary for electrochemical degradation of AO7. Furthermore, because output electrical energy is a function of mechanical strain, we hypothesized that BTO nanomaterials having shapes conducive to supporting strain (i.e., rods) would improve the rates of AO7 degradation. The influence of BTO nanomaterial shape on the kinetics of AO7 decolorization was explored by comparing the rates of decolorization in the presence of tetragonal BTO cuboidal nanoparticles (purchased commercially) with benchtop synthesized BTO nanorods.

3.1.1 Preliminary assessments of electrolytic degradation of AO7

As an initial proof of concept, the rate of AO7 decolorization mediated by electrochemical processes was investigated through electrolysis experiments conducted in batch systems of 20 μM AO7 in the presence of 10 mM phosphate buffer (initial pH ~7.3). Two Pt wires were used the working and counter electrodes and were both placed in the same beaker. Electric potentials of 2.5 V and 1.0 V were applied between two Pt wires to compare the rates of AO7 degradation above and below the decomposition potential of water (1.23 V).

AO7 electrolysis curves were fitted as pseudo-first order decay (Figure 13). Degradation proceeded much more rapidly with 2.5 V applied (k_{obs} = 0.0037 min^{-1}, R^2 = 0.996) than with 1.0 V applied (k_{obs} = 0.0007 min^{-1}, R^2 = 0.986). The decolorization observed at 2.5 V may be due to direct oxidation of AO7 at the electrode-solution interface or may be due to the production of hydroxyl radicals (or atomic hydrogen) following the decomposition of water (as given by the reactions shown in Eqs. 3 - 11). When the applied voltage was decreased to 1.0 V (below the decomposition potential of water), AO7 degradation may be more likely related to direct redox reactions occurring at the electrode-solution interface. The formation of transformation products was monitored by collecting absorbance scans from 200 – 700nm in the UV-vis spectrophotometer. Neither 2.5V nor

1.0V applied resulted in the growth of any tertiary peaks in the absorbance pattern (Figure 14). These results suggest that AO7 decolorization can occur at very low voltages, which makes it a suitable model pollutant target for evaluating piezocatalytic activity.

3.1.2 AO7 degradation with commercial barium titanate nanoparticles

Batch systems were sparged with N_2 gas before sonication to eliminate dissolved oxygen because it is known that sonication induces molecular oxygen to undergo reduction to generate reactive oxygen species (ROS) in solution [69]. Indeed, AO7 degraded rapidly in batch systems sonicated in the presence of oxygen. And even in the absence of O_2 or BTO, AO7 was degraded under sonication (Fisher Scientific, 42 kHz, 100W output) at a relatively steady rate of 0.02 μM AO7 min^{-1} ($R^2 = 0.98$) in the control experiments (replicated sevenfold). We propose that AO7 decolorization is the absence of any solids is related to sonolysis, whereby cavitation bubbles are produced spontaneously in aqueous media under sonication [70]. These cavitation bubbles may directly induce AO7 decay by thermolysis or indirectly (such via the production of radicals react with AO7) [70]. This background rate of decolorization of AO7 from controls due to sonolysis was compared to rates of decolorization in the presence of various commercial and laboratory-prepared BTO nanoparticles.

Commercially prepared tetragonal BTO nanoparticles were used as a reference standard to ascertain the piezocatalytic activity of tetragonal BTO crystals. Images prepared with SEM and the XRD pattern of the commercial barium titanate nanocrystals are shown in Figure 15 (panel 'A') and Figure 16, respectively. The commercial nanoparticles were cuboidal in shape and were found to have a c:a lattice ratio of 1.009, which confirms that the powder was of the tetragonal phase. At a mass loading of 0.1 g/L, it was found that tetragonal commercial BTO powder did not contribute to the decolorization of AO7 significantly beyond that of the control (Figure 17). This lack of decay may be related to the fact that the crystals' cubic shape prevents substantial deformation upon the application of mechanical force from ultrasonication. Piezoelectic output is dependent on the strain rate of the material. We expected that spherical or semi-cubic nanoparticles would be less responsive to forces imparted to the solution via sonication than anisotropic morphologies like rods or sheets.

3.1.3 AO7 degradation with unsupported laboratory-developed barium titanate nanoparticles

The inclusion of tetragonal, unsupported BTO nanocrystals hydrothermally prepared in the presence of 6.5 vol% ethylene glycol (hereafter 'US 6.5EG') significantly accelerated the rate of decolorization of AO7 in the batch solution during sonication. As shown in Figure 18, the morphologies of the US 6.5EG BTO crystals consisted of a heterogeneous mixture of cubic and rod-like shapes. BTO rods up to 1.8 μM and 0.2 μM wide were located, but were more typically ~400 nm x ~50 nm. Cuboidal crystals were generally between 50-150 nm per face. XRD confirmed the presence of the tetragonal phase, with a clear splitting of the [200] peak into [002] and [200] planes (Figure 16). The c:a lattice ratio of these materials was found to be 1.009, again consistent with the tetragonal phase.

Unlike the commercial powder, the addition of the US 6.5EG nanocrystals significantly accelerated the rate of AO7 decolorization. At a mass loading of 0.1 g/L, ultimate degradation (over three hours) increased by approximately 20% from the control with the US 6.5EG batch system exhibiting an average pseudo-first order rate of decay of 0.03 μM AO7 min^{-1} ($R^2 = 0.97$). The pH was monitored at t=0 and t=180 min and was not found to change significantly (starting and final pH typically hovered around 7.2-7.3). Moreover, the rate of decolorization was affected by the mass loading of US 6.5EG. Batch systems with 0.5 g/L US 6.5EG resembled first-order decay, with an estimated first-order rate constant of 0.005 min^{-1}. However, both mass loadings ultimately ended up at the same final concentration of AO7 at the end of the three-hour sonication period.

The difference in reactivity between the synthetic BTO and the commercial BTO powder may be the result of the shape-specific factors affecting piezocatalytic activity, discussed above. The synthetic US 6.5EG tetragonal nanocrystals consisted of a mix of cuboidal and rod-like crystals. These elongated morphologies are likely to be more conducive to supporting significant bending strains under ultrasonication and therefore be capable of generating larger voltages available for catalysis. Thus, the development of next-generation piezocatalytic materials must include crystal shape as essential criteria for effective piezocatalytic activity.

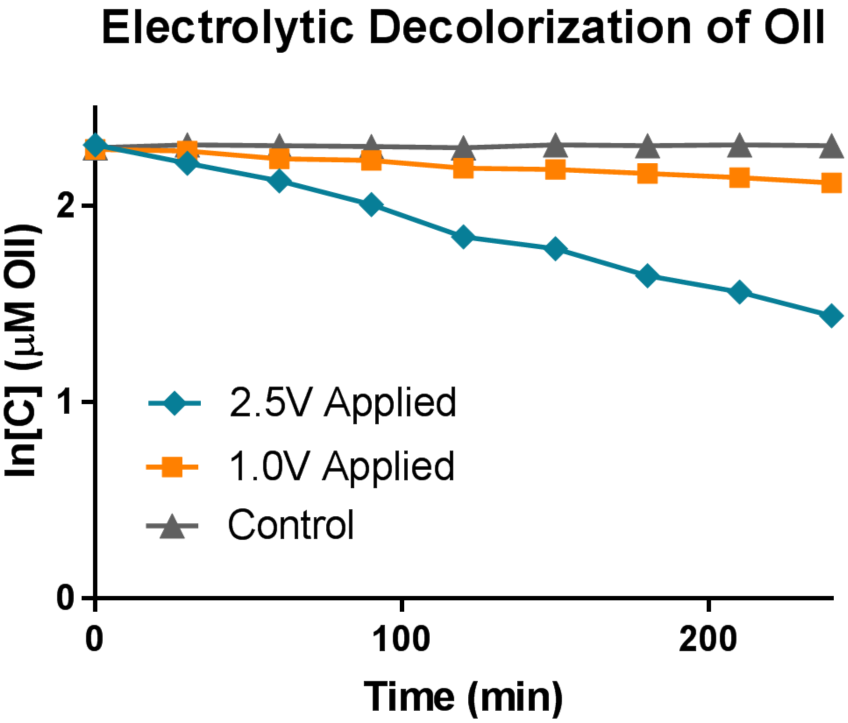

Figure 13 Electrolytic decolorization of AO7 under constant applied voltage. Decay curves were fitted as pseudo-first order.

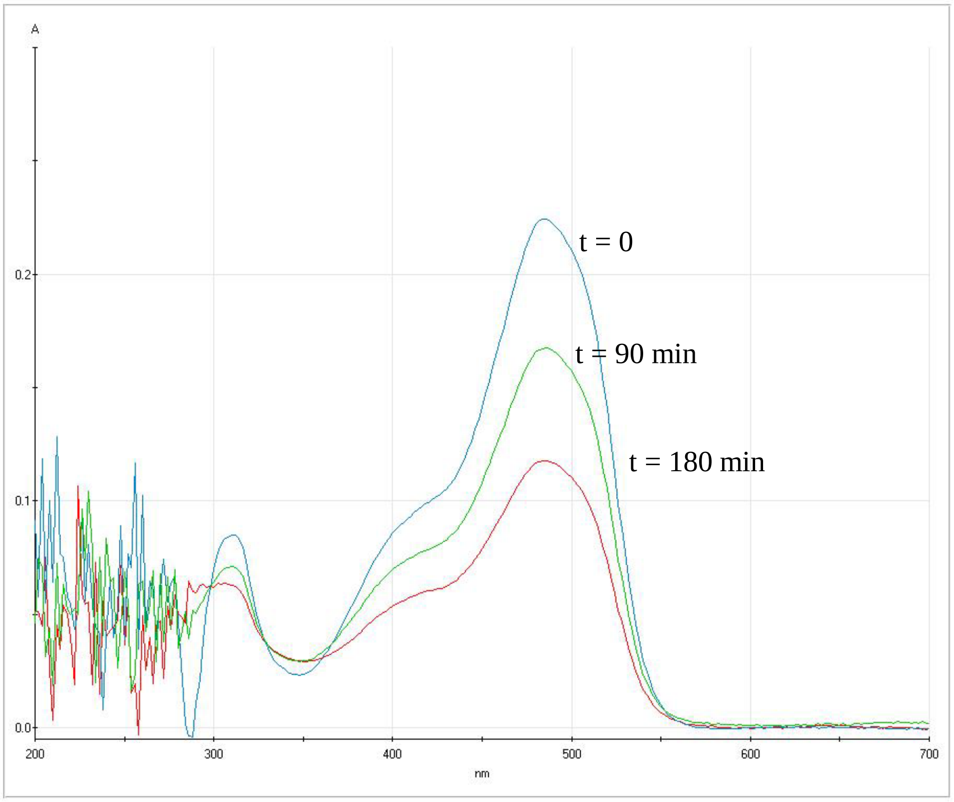

Figure 14 Absorbance scans collected from the 2.5V electrolytic decolorization of AO7. No tertiary peaks corresponding to the formation of transformation products were observed over the course of the experiments

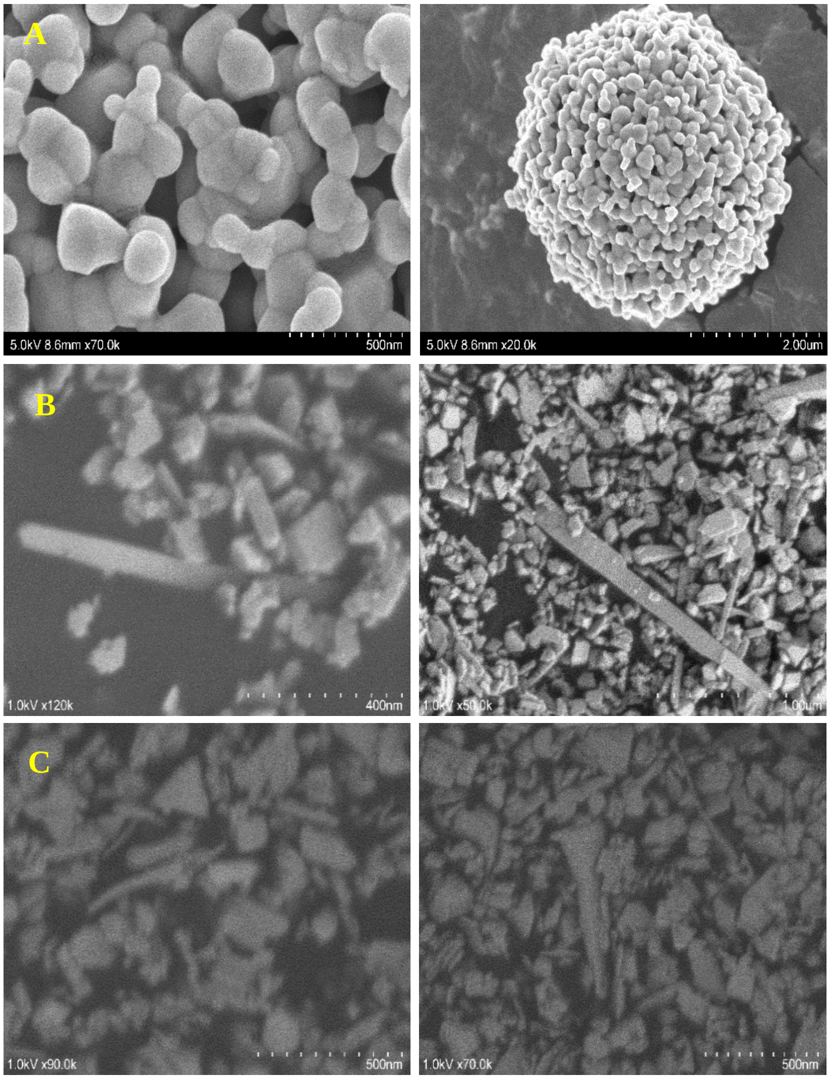

Figure 15 Unsupported (a) commercial barium titanate nanoparticles (tetragonal, 200nm) and BTO nanoparticles synthesized in-laboratory by (b) 'one-pot' method with 6.5 vol.% EG, and (c) 'one-pot' method with 8.0 vol.% EG

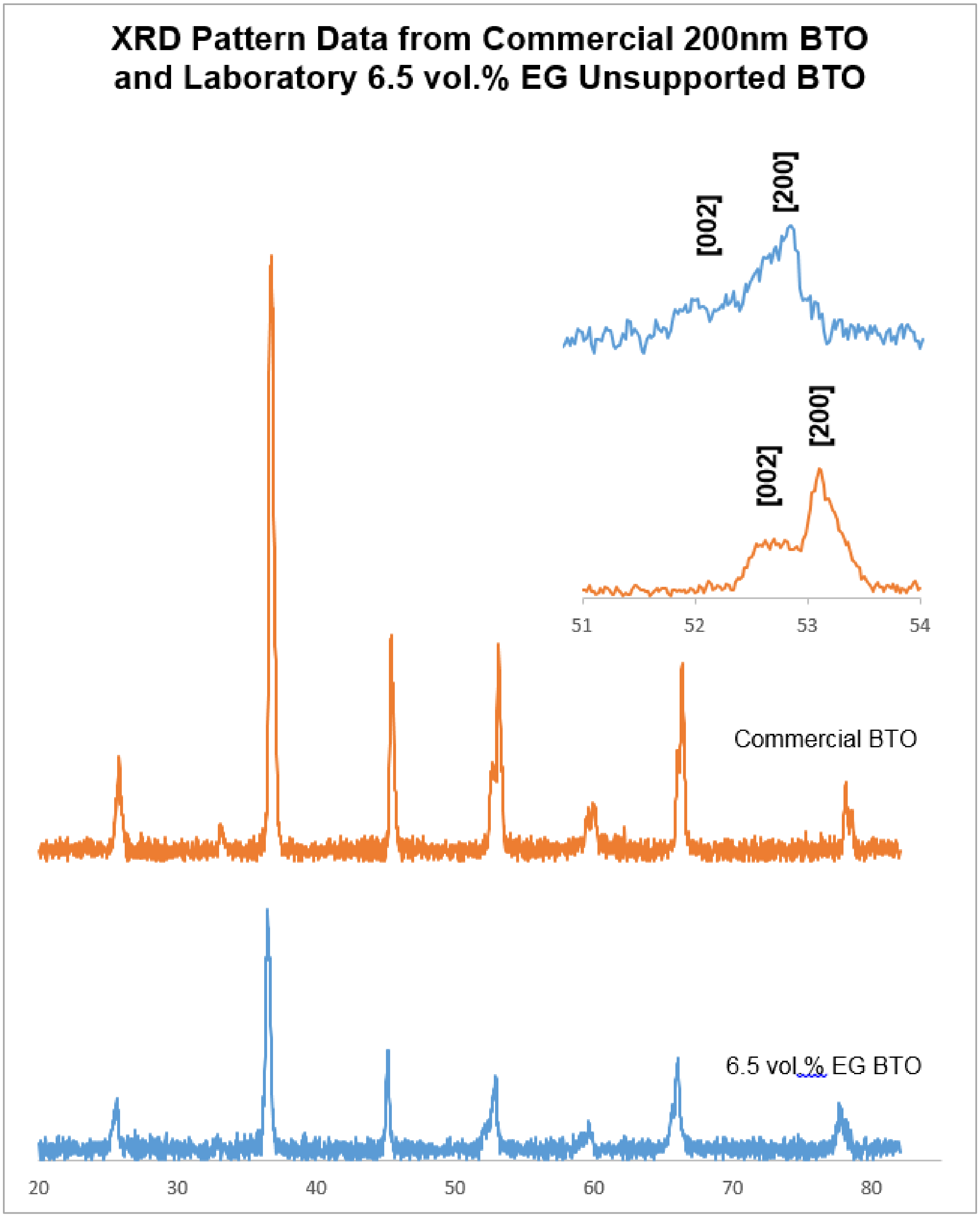

Figure 16 XRD pattern data from commercial and hydrothermally synthesized 6.5 vol.% EG BTO nanoparticles

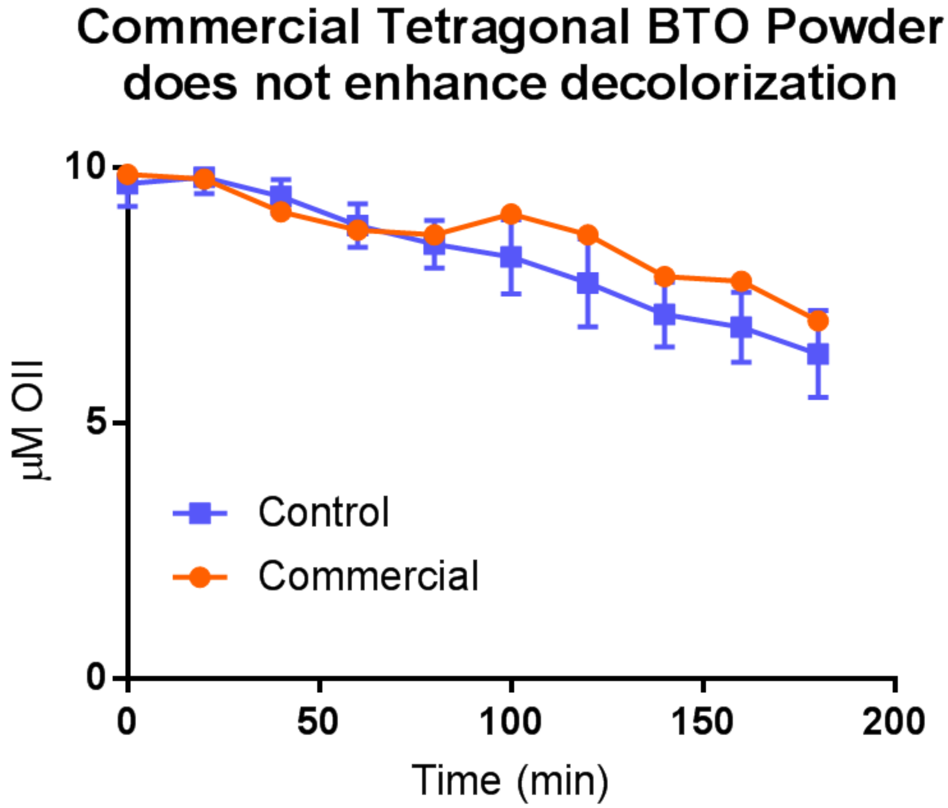

Figure 17 Batch sonication study of the 200nm Commercial Tetragonal BTO powder in an N_2 atmosphere. Commercial powder did not contribute to decolorization beyond that of the control.

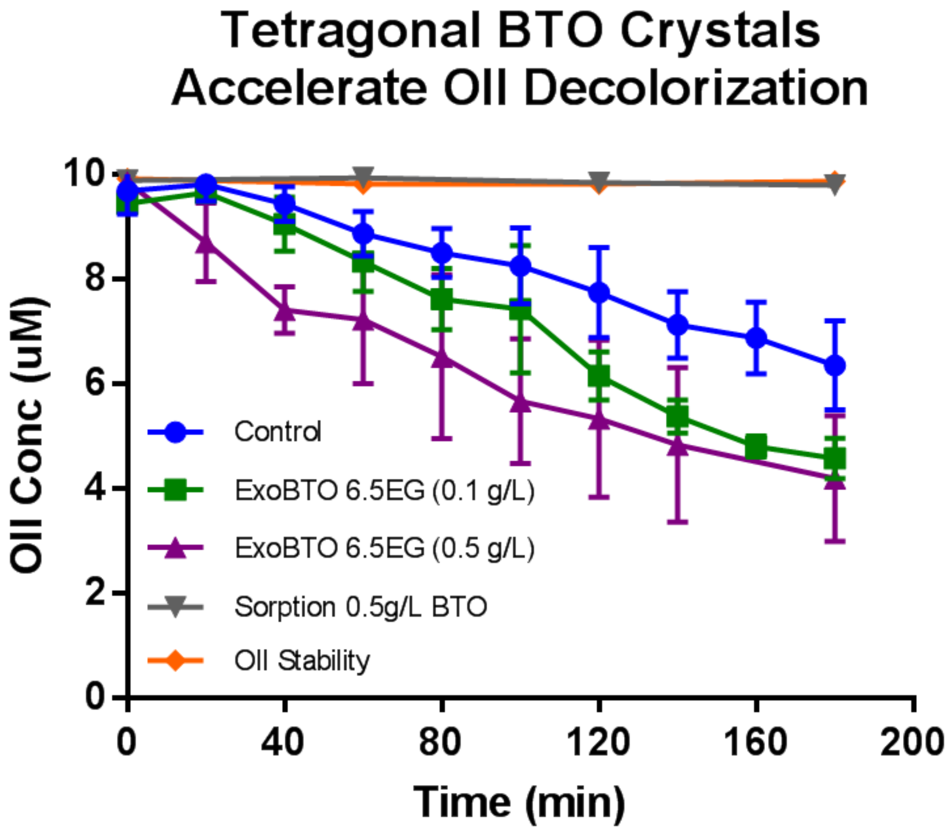

Figure 18 Batch sonication of unsupported barium titanate crystals in the presence of Sodium Orange II dye in an N_2 atmosphere. Batch suspension of the 6.5 vol.% EG crystals resulted in pseudo-first order decay of AO7, with initial kinetics being influenced by mass loading

CHAPTER 4 DEVELOPMENT AND CHARACTERIZATION OF CARBON NANOFIBER/BARIUM TITANATE COMPOSITES

4.1 Improving dispersion of TiO_2-seed crystals in precursor PAN nanofibers

In the fabrication of CNF/BTO composites, Degussa P25 TiO_2 (denoted P25) nanoparticles (mean diameter = 21 nm) were first embedded into a PAN nanofiber support. After PAN carbonization to CNFs, these embedded P25 nanoparticles served as seed crystals for BTO growth during hydrothermal synthesis. Sufficient dispersion of P25 within the PAN nanofibers is necessary to promote the uniform growth of BTO crystals along the CNFs, which in turn would maximize crystal surface area available for piezocatalysis.

Absorbance patterns collected from 12h settling tests revealed that P25 was held in suspension best in sol-gels prepared with 2.4 wt.% phthalic acid (PTA), 2.4 wt.% terephthalic acid (TPTA), and with no additional surfactants (only P25 and DMF) (Figure 20). Near complete solids separation was observed in sol-gels prepared with SDS and TBAB, and partial settling was observed in the sol-gel prepared with CTAB (visible in the insets in Figure 20).

Guided by the settling study, PAN/6.0P25 sol-gels with no included surfactant, 3.5 wt.% TPTA, and 2.4 wt.% PTA were electrospun and imaged under SEM to qualitatively assess P25 dispersion. Large and relatively isolated P25 aggregates were observed in nanofibers prepared in the absence of any surfactant (Figure 21, panels ‘A’ and ‘A2’). Nanofibers synthesized with 3.5 wt.% TPTA exhibited better dispersion of P25, but still suffered from infrequent P25 clusters and amorphous internal nanofiber beading (Figure 21, panels ‘B’ and ‘B2’). In contrast, images suggested that 2.4 wt.% PTA most effectively dispersed P25 and resulted in more uniformly integrated P25 nanoparticles within the PAN nanofibers (Figure 21, panels ‘C’ and ‘C2’).

PTA-P25 adsorptive interactions may explain these observations. It has been reported that PTA chemisorbs onto surfaces of P25 nanoparticles to form bidentate ring complexes in water (Figure 19) [71, 72]. Accordingly, PTA would act as a stabilizing or “capping” ligand to help prevent the agglomeration of P25 during the electrospinning process [72]. Our observation of improved P25 dispersion is also consistent with previous work from our group, which demonstrated that the inclusion of PTA at 2.4 wt.% in a PAN precursor sol-gel improved the dispersion of TiO_2 [72]. We note that the inclusion of PTA holds the added benefit of increasing the bending strength of CNFs in the carbonized mat [72, 73].

Given the initial promise of PTA as a dispersing agent for P25, additional investigations considered the influence of PTA loading on composite nanofiber morphology and dispersivity. Here, PTA was added to the PAN/P25 precursor solution at 2.4%, 2.7%, 3.0%, 3.5%, and 4.0% wt. (per total sol-gel mass). From SEM, 2.7% wt. PTA appeared to improve the dispersion of P25 relative to 2.4 wt.% PTA, with nanofibers exhibiting a uniform coating of isolated P25 nanoparticles along the nanofibers (Figure 22, panels ‘A’, ‘A2’, ‘B’ and ‘B2’). Above this fraction, amorphous bulging and polymer

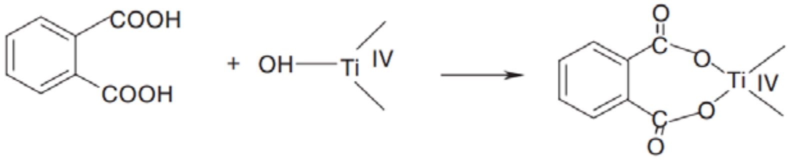

Figure 19 PTA adsorbs to Surfaces of TiO_2 particles, reproduced from Hailong Liu et al., 2011

beading was observed in the nanofibers, with no evidence of improved dispersion of P25 observed (Figure 21, panels 'C' and 'D').

Average diameters in PAN/P25 precursor nanofibers were measured using ImageJ software analysis of at least n = 100 nanofibers. PAN nanofibers with no P25 or PTA had an average diameter of 100 ± 30 nm at the synthesis conditions discussed above. Both P25 and PTA enhanced the viscosity of the electrospinning sol-gel and therefore led to increases in average fiber diameters, as typically occurs in more viscous electrospinning solutions. The inclusion of 6.0 wt.% P25 also increased the average diameter of the fibers to 240 ± 60 nm. At this P25 loading, PTA had a negligible effect on fiber diameter at 2.4 wt.% but further increased the average diameter to 480 ± 70 nm at 2.7 wt.% and to 550 ± 105 nm at 4.0 wt.% PTA.

4.1.1 Carbonization and optimizing composite flexibility

Polymer composite mats were carbonized to yield CNFs, which are chemically stable and capable of resisting the high temperatures and pressures and concentrated alkaline conditions needed to grow barium titanate crystals [56]. Carbonization of the PAN/P25/PTA composites yielded fibers that were pockmarked (Figure 23, panels 'B' and 'D'), presumably from the sublimation of phthalic anhydride out of the polymer matrix that occurs around 295^o C [57, 74]. The sublimation of PTA also left behind macropores on the fiber surface (Figure 22). Observable porosity increased with the weight fraction of PTA, consistent with expectations for greater PTA sublimation. Porosity was not observed in carbonized composites with 3.0 wt.% PTA or lower. However, composites prepared with 4.0 wt.% PTA and carbonized at 750 ^{o}C resulted in dense clusters of pores interspersed with aggregates of P25 nanoparticles along fiber surfaces (Figure 22, panel ‘D2’). We believe that, due to the adsorptive P25-PTA complexes formed in the precursor sol-gel, electrospinning would generate fibers with P25 nanoparticles coated with PTA. By extension, carbonization would generate porosity preferentially near areas of relative P25 density.

The capacity of the CNF/P25 composites to sustain large bending strains without fracture was a critical parameter in the development of these materials because piezocatalytic performance was expected to be a function of mechanical strain. Without modification, carbonized PAN nanofibers tended to be very brittle and ruptured easily at minimal strains. However, a secondary benefit of the inclusion of phthalic acid is that it improves the flexibility and strength of the carbon nanofibers [57]. For example, composite mats synthesized with 2.7 wt.% PTA and carbonized at 750 ^{o}C were bent at large strains across multiple axes without fracture, whereas CNFs prepared in the absence of PTA shattered with minimal force applied (Figure 30, panels ‘A’, ‘A2’, ‘B’, ‘B2’).

CNF strength was also expected to be a function of carbonization temperature [75]. Therefore, carbonization temperatures were systematically varied between 450 ^{o}C and 1200 ^{o}C for 8.0PAN/6.0P25/2.7PTA composites to qualitatively assess mat resilience to deformation. In general, composite flexibility was inversely related to carbonization temperature, with composites carbonized at 900 ^{o}C and 1050 ^{o}C fracturing at minimal bending strains (Figure 30). Composites treated at 450 ^{o}C, 600 ^{o}C, and 750 ^{o}C were able to bend significantly without fracture.

However, it is known that temperatures exceeding 600 ^{o}C are needed to achieve complete denitrogenation of PAN [75]. Accordingly, samples pyrolyzed at 450^{o} C showed signs of incomplete carbonization, making them vulnerable to hydrothermal degradation. Indeed, samples remained brown (rather than turning characteristically black) after pyrolysis at 450 ^{o}C for one hour and physically deteriorated after hydrothermal treatment. Mats carbonized at 750 ^{o}C for 1 h with 2.7% wt. PTA were sufficiently carbonized to resist hydrothermal degradation, but were still flexible enough to be folded along one axis without fracture (Figure 30).

In addition to fraction of PTA, fiber porosity also appeared to correlate with increasing carbonization temperature. High temperature (>1000 ^{o}C) pyrolysis induced solid state recrystallization and growth of embedded P25 nanoparticles into larger rutile TiO_2 crystals (Figure 23, panels 'D' and 'D2'). Indeed, XRD patterns confirm the growth of large rutile crystals in the composite mats as carbonization temperature was increased from 450 ^{o}C to 1050 ^{o}C. CNFs treated at 1050 ^{o}C and 1200 ^{o}C developed pores and cracks uniformly along fiber lengths. The solid-state nucleation of P25 may be responsible for porosity observed in the composites pyrolyzed at high temperatures.

Carbonized nanofiber diameters ranged between 314 ± 112nm (900 ^{o}C) to 490 ± 112nm (750 ^{o}C), with no discernible trends in average diameter related to carbonization temperature evident (Figure 24).

4.2 Development of the hydrothermal method to fabricate CNF/BTO composites

CNF/BTO composites produced by both the 'two-stage' and 'one-pot' alkaline hydrothermal methods were evaluated against several criteria. First, because BTO crystals were expected to act as catalytic sites for contaminant degradation, optimized CNF/BTO composites should maximize crystal density. Second, composite materials must maintain flexibility and structural resiliency following hydrothermal processing to effectively perform as piezocatalysts. Third, hydrothermal synthesis of barium titanate must lead to the stability of the piezoelectric tetragonal crystalline phase at room temperature in order to harness electromechanical coupling properties from BTO crystals. And fourth, preference would be given to the hydrothermal method that minimized chemical demand and the use of toxic precursor materials and reagents.

4.2.1 BTO/CNF composite fabrication with 'two-stage' hydrothermal synthesis

'Two-stage' hydrothermal synthesis relied on two separate hydrothermal reactions to convert embedded P25 first to sodium titanate ($Na_2Ti_nO_{2n+1}$ for n = 2, 3, 4) (denoted NaT) and next to barium titanate (denoted BTO). NaT crystals consisted of partially melded agglomerates of nanorods that stretched along and between CNF fibers (Figure 26, panels 'A' and 'B') [65]. The formation of NaT nanorods from hydrothermal treatment in 10 M NaOH at 150^o C is consistent with previous findings on the formation of NaT from the literature [65].

The uniform crystalline coating of NaT on the nanofibers did not persist through the ion exchange conversion to BTO. Reaction with $BaCl_2$ produced relatively isolated clusters of BTO throughout the nanofiber matrix (Figure 26, panel 'C'). BTO crystal clusters typically consisted of several cuboidal crystals adjoined together at a common base (Figure 26, panel 'D'). CNF/6.0P25 composites hydrothermally treated for 8h in both the first and second stages of treatment yielded semi-cubic BTO crystals, with a c:a lattice ratio of 1.003. Similarly, BTO crystals generated from 10 hours of second stage $BaCl_2$ treatment produced crystals with a lattice ratio of 1.001. As discussed above, phase-pure tetragonal barium titanate crystals are known to have a c:a lattice ratio of ~1.01. Two-stage hydrothermal synthesis, therefore, generated composites with only slight lattice distortions from the cubic phase. In general, two-stage hydrothermal treatment failed to produce sufficiently tetragonal BTO crystals.

Moreover, CNF/BTO composite mats produced via two-stages of hydrothermal treatment were structurally deficient compared to the CNF/P25 precursor mats. CNF/BTO produced via two-stage synthesis crumble easily during handling, which limits their viability as piezoelectric materials. Physical deterioration of the composite mat was likely related to the harsh processing conditions (10 M NaOH), as well as the second round of additional hydrothermal treatment. Consequently, the two-stage method failed to satisfactorily meet the design criteria outlined above for optimal piezoelectric materials.

4.2.2 BTO/CNF composite fabrication with 'one-pot' hydrothermal synthesis

One-step in-situ conversion of embedded TiO_2 to BTO was far more promising in producing a flexible composite with sufficiently high density of BTO crystals (Figure 27). This approach yielded a dense population of BTO crystals embedded in the nanofiber matrix, producing BTO crystal morphologies (generally <300 nm) that exhibited varying degrees of distortion from the cubic phase. Furthermore, the composite mats retained bending flexibility and tensile strength following hydrothermal treatment (assessed qualitatively – Figure 30).

More practically, this 'one-pot' synthesis was simpler in application and involved a smaller chemical footprint than the two-stage synthesis. In general, the 'one-pot' synthesis sufficiently satisfied all of the design criteria outlined above and was used for further synthesis studies. However, there were several synthesis variables that preliminary investigations revealed to be influential to the properties of the resulting BTO/CNF composites. These variables and their influence on composite properties are discussed below.

4.3 Influence of temperature on barium titanate crystallinity and piezoelectric performance

A study of the effects of hydrothermal treatment temperature on the formation of BTO revealed that higher temperatures generally resulted in larger XRD diffraction intensities. XRD peak intensity is influenced by a variety of factors including sample crystallinity, multiplicity of Bragg planes, extinction, and absorption phenomena. For similarly processed CNF/BTO composites, however, increasing peak intensity was considered indicative of either improved crystallinity or greater crystal density in the mats. For example, hydrothermally treating composites at 80 ^{o}C registered diffraction patterns with relatively low-intensity or only a few BTO peaks. Consequently, substantial anatase and rutile TiO_2 diffraction lines persisted in the 80 ^{o}C composite pattern (Figure 32). At 100 ^{o}C, anatase and rutile peaks were diminished and were offset by well-established BTO peaks (Figure 32 - 33). At and beyond 120^{o} C, no residual TiO_2 peaks were observed in the XRD pattern. A small peak at approximately 34.0 2θ was determined to be due to $k\beta$ scattering from the nearby peak at 37.5 2θ. Diffraction patterns registered with XRD from the temperature study are shown in Figure 33.

Changes to the embedded P25/BTO crystals' morphology and density were also observed as a function of temperature under SEM. Composites treated at 80 ^{o}C retained significant P25 nanoparticles implanted on fiber surfaces. Large (870 ± 330 nm), spherical crystals thought to be early stages of barium titanate were infrequently observed throughout the mat, which is supported by the low-intensity BTO XRD signals observed at this temperature, as well as the persistent diffraction lines corresponding to anatase and rutile TiO_2 for treatments at 80^o C and 100^o C (Figure 32 - 33). Furthermore, barium EDS maps of composite nanofibers show that barium (indicated by red dots) is incorporated into the composite mats at a much greater density at 120 ^oC than at 80 ^oC (Figure 31). It is not altogether surprising that BTO transition occurs more rapidly at elevated temperatures, given that reaction rates are typically directly proportional to temperature.

It was expected that higher treatment temperatures would result in increasing lattice distortion away from the cubic phase upon cooling through the Curie temperature at 125 ^oC. However, an investigation into the effects of hydrothermal treatment temperature on lattice constants showed no discernible trends with respect to degree of tetragonality. Lattice ratios for temperature samples are shown in (Figure 35). Hydrothermal treatment at 220 ^oC yielded the largest average c:a ratio of 1.008. Composites treated at 120 ^oC registered a c:a ratio of 1.005, and all other composites were semi-cubic, with ratios ≤ 1.004. Moreover, the characteristic splitting of the [200] peak at a 2θ value of ~53 (taken to indicate significant presence of the tetragonal phase) was not observed in any of the composites treated exclusively with $Ba(OH)_2$ (Figure 33).

Finally, we considered the influence of hydrothermal treatment temperature on the composites mechanical strength. Following hydrothermal treatment, the CNF/BTO composites prepared from CNF/6.0P25 composites carbonized at 750 ^oC for one hour were moderately flexible, but delamination between layers of the mat sometimes occurred as a result of mechanical strain. Delamination and mat cohesiveness deteriorated at treatment temperatures exceeding 220 °C. Materials prepared in low-temperature hydrothermal baths retained mechanical flexibility and moderate strength, but were not resilient to tearing. This delamination would limit their practical utility as piezoelectric materials.

4.3.1 Electromechanical testing of composites prepared from the hydrothermal temperature study

Select CNF/6.0P25 composites hydrothermally treated between 100 and 260 °C were tested to determine electromechanical properties on a custom-built cantilever-oscilloscope apparatus. Figure 36 - 37 show the output voltage of the samples as a function of applied resistance and hydrothermal temperature. Each of the hydrothermally treated samples showed a degree of piezoelectric response. As is expected from Ohm's law, the output voltage of all of the composites scaled proportionally with the applied resistance.

The composite prepared at 220 °C generated the most power and largest voltages at all evaluated strains, with a maximum registered peak-to-peak voltage of 3.8 V and corresponding power of 0.760 μW at a measured strain of 0.137% (Figure 37). This result was notable given that composites prepared at 220 °C exhibited the largest degree of lattice distortion toward the tetragonal phase, with an average c:a ratio of 1.007. This was consistent with our expectation that electromechanical properties would be a function of observed lattice tetragonality.

The composite prepared at 260 °C also exhibited significant piezoelectric characteristics. At 0.137% strain, this sample produced a maximum peak-to-peak voltage of 2.8 volts and a corresponding power of 0.485 μW. However, the average lattice parameter of the 260 °C composite was only slightly larger than the other tested samples (1.005 vs. 1.004 and 1.003). Indeed, some groups have noted that crystal point-defects such as hydroxyl substitution into the BTO lattice may be eliminated at hydrothermal temperatures exceeding 150° C [52]. Crystal lattice imperfections may also help explain the lack of substantial electromechanical response of the composites prepared at sub-200 °C hydrothermal temperatures.

The measured piezoelectric response of the hydrothermally prepared samples is also noteworthy because of the nanoscale BTO grain sizes. Average crystallite grain size was assessed using the Scherrer equation. Grain size was largely independent of temperature, with average grain sizes for all reported temperatures on the order of ~20 nm. Conventional wisdom has held that piezoelectricity is generally not observed at sub-micron crystalline grain sizes, due to grain boundary and domain wall restrictive effects [39]. To the best of our knowledge, our study is among the first to report significant electromechanical response of sub-100nm grains of BTO crystals prepared with the hydrothermal method.

4.4 Influence of BTO mass loading on crystal growth and electromechanical properties

Mass loadings of BTO in the composite mats were controlled by systematically varying the weight percentage of P25 TiO_2 in the precursor sol-gel. Using results from the temperature study, composites were hydrothermally treated at 220 °C to reproduce the piezoelectric properties observed earlier.

Changes in BTO crystal density as a function of P25 loading were assessed qualitatively with SEM and XRD. Higher mass loadings of P25 correlated with a marked increase of BTO crystal density on the nanofiber surface. BTO crystals were morphologically cubic and similarly embedded within the nanofiber matrix in all cases. The composite prepared with 6.0 wt.% P25 registered a phase-pure tetragonal c:a ratio of 1.010, whereas the lattice ratios of the 9.0 wt.% and 12.0 wt.% samples were calculated to be 1.005 and 1.007, respectively.

We had initially hypothesized that output voltage per volume of mat would increase with loading of BTO. However, electromechanical testing of the varied BTO samples revealed that, while the 9.0 wt.% and 12.0 wt.% composites generated larger voltages at 0.017% and 0.045% strain, the 6.0 wt.% P25/BTO composite substantially outperformed the other samples at the maximum strain evaluated of 0.137% (Figure 39) At this strain and open-circuit oscilloscope resistance, the hydrothermally treated 6.0 wt.% P25 sample produced a maximum peak-to-peak voltage of 5.0 V. At similar conditions, the 9.0 wt.% P25 and 12.0 wt.% P25 samples achieved 2.8 V and 2.17 V, respectively (Figure 39).

The unexpected decrease in output voltage following increased mass loadings of BTO could be related to several factors. First, as noted above, the 6.0 wt.% P25 hydrothermally treated mat exhibited the greatest degree of tetragonal lattice distortion with a calculated c:a ratio of 1.010 (reported in the literature as phase-pure tetragonal BTO). The higher BTO samples registered only moderate lattice distortion. The discrepancy in lattice distortions between samples could be related to several factors. First, as shown in Figure 35, sample-to-sample variability of lattice distortion is significant, especially at temperatures exceeding 180 ^{o}C. And certain variables during the fabrication of these materials were not controlled, such as the dimensions of the CNF/P25 composite mats (possibly having mass transfer implications), or the positioning of the mats within the reactor (BTO growth is likely influenced by thermal gradients in the reactor). Moreover, the sealed steel reactors relied upon for material synthesis were not equipped with pressure gauges, so internal vessel pressure (another critical parameter for the crystal growth) was controlled only indirectly by maintaining constant reactor temperature and volume. As a result, the difference in lattice parameters between the 6.0P25, 9.0P25, and 12.0P25 samples could simply be the product of synthesis variability.

However, it is worth noting that composites treated at 220 ^{o}C averaged the largest average c:a ratio (1.008) of the temperature study samples . It is possible that 6.0 wt.% P25 constituted the optimal P25:$Ba(OH)_2$ molar ratio for tetragonal BTO crystal growth at these particular experimental conditions and that increasing the loading of P25 deviated from this relationship and consequently produced comparatively cubic crystals.

Increased BTO loading may also have weakened the fibers' structural integrity, making them more prone to fracture at larger strains (thereby dampening piezoelectric response). This could potentially explain the fact that the 9.0 wt.% P25 and 12.0 wt.% P25 composites outperformed the 6.0 wt.% P25 composites at lower strains, but lacked significant response at larger strains. If this is the case, higher BTO-loaded composites may be more appropriate for catalytic water treatment applications given that ambient energy harvesting (such as from pump vibrations or turbulent flow) is expected to impart limited mechanical energy to the materials (resulting in relatively marginal strain rates).

With the goal of catalyzing redox reactions pertinent to water treatment applications (either via radical production or direct oxidation/reduction), optimized piezoelectric composites must generate sufficient voltage as well as current to drive electrochemical reactions. Starr and Wang (2013) reported that electrode potentials exceeding ~3 V (versus the Standard Hydrogen Electrode (SHE)) are required for thermodynamically favorable direct oxidation or reduction of aqueous chemical species [33]. As noted above, treatment of the 6.0 wt.% composite mat at 220 ^{o}C resulted in a peak voltage output of 2.5 V at the maximum strain tested (maximum peak-to-peak of 5.0 V). This potential should be sufficient to undergo water splitting (requiring an oxidative potential of 1.23 V) and is a promising potential for powering redox chemistry relevant to water treatment, despite the fact that it falls slightly short of the ~3.0 V standard set forth by Starr and Wang. Further, several studies have reported the decay of recalcitrant organic contaminants at potentials substantially less than 3.0 V with the application of co-oxidants such as hydrogen peroxide [76]. Output voltage of these composite materials is slightly offset by the marginal electrical currents that can be extracted from the piezoelectric materials. At the maximum strain, the peak-to-peak voltage of 5.0V corresponded to a power output of approximately 1μW.

Guided by the data obtained from the temperature study and BTO mass loading study, hydrothermal treatment at 220 ^{o}C of CNF/6.0P25 composites was determined to be an optimal recipe for synthesizing nanostructured piezoelectric CNF/BTO composites with morphologically cubic crystals.

4.5 Influence of ethylene glycol on barium titanate crystal growth and electromechanical properties

Barium titanate crystal morphology and phase was manipulated using ethylene glycol as an organic cosolvent during hydrothermal treatment. As noted earlier, the inclusion of ethylene glycol (EG) during the hydrothermal synthesis of barium titanate has been reported to promote the formation of the tetragonal phase [52]. Ethylene glycol selectively adsorbs to BTO crystalline faces during the dissolution-precipitation nucleation process and therefore forces the anisotropic growth of BTO. It has also been reported that EG inhibits the dissolution of Ba-Ti-OH precursors, which alters the mechanism and kinetics of BTO formation [52].

CNF/6.0P25 samples treated with 5 – 12.5 vol.% EG at 200 ^{o}C consistently produced nearly phase-pure tetragonal BTO crystals with lattice c:a ratios exceeding 1.009 (Figure 43). The addition of EG even at low volume fractions appears to drastically increase the lattice distortion of the BTO unit cell. Moreover, composites treated in 10.0, 11.0, and 12.5 vol.% clearly showed a split peak at 53.5 2θ, indicating the presence of both the [200] and [002] crystal planes and the predominance of the tetragonal phase (Figure 42). The largest tetragonal lattice distortion according to the c:a ratio was calculated to be 1.013 from CNF/6.0P25 composites prepared in 11.0 vol.% EG at 220 ^{o}C.

Further, morphological changes to BTO crystals were observed at low EG volume fractions. Hydrothermal treatment of CNF/6.0P25 at 200 ^{o}C with 5.0 vol.% and 7.5 vol.% EG resulted in BTO cuboidal crystals that were slightly elongated along one axis (Figure 40, panels ‘A’ and ‘B’). Samples treated in 10 vol.% EG produced a mixture of morphologically cuboidal and elongated rod-like crystals up to 1.6 μm in length. Treatment in 11.0 vol.% EG produced BTO crystals that were heterogeneously rod-like. Generally, the BTO crystals were embedded in the CNFs longitudinally along the fiber or radially out from the fiber. No consistent growth patterns were evident from SEM. At 12.5 vol.% EG, BTO crystallites grew out and beyond individual nanofibers and tended to stretch between or coil around individual nanofibers. However, at 15.0 vol.% EG, BTO crystallization was suppressed with the exception of a low-intensity (110) peak at 2θ value of 38. Resultant Ba-Ti-O amorphous nanostructures prepared at this EG fraction grew anisotropically in sheet-like character and uniformly coated nanofibers (Figure 41)

Variations in barium titanate crystal morphology were further investigated by hydrothermally treating 10.0 vol.% EG samples at temperatures between 140 – 220 ^{o}C. Low-temperature hydrothermal treatment at 140 ^{o}C produced thin, plate-like, and amorphous Ba-Ti-OH compounds that only weakly registered [100], [001], and [101] BTO diffraction lines. Treatment at 160 ^{o}C yielded more crystalline BTO with all major BTO peaks observable in XRD. Crystal morphologies consisted of an interesting mix of symmetrically angular sheet-like crystals (Figure 45, panel 'B2') and clusters of pointed, rod-like crystals (Figure 45, panel 'B'). Similarly, composites treated at 180 ^{o}C yielded poorly-crystalline BTO nanostructures arranged in sheet-like structures akin to what was observed at 160 ^{o}C (Figure 45, panels 'C' and 'C2'). However, at 180 ^{o}C, XRD recorded the presence of a variety of diffracting planes not associated with BTO (Figure 47). However, the clear formation of crystalline BTO resulted from treatments at 200 ^{o}C and 220 ^{o}C, with crystal morphologies resembling elongated rods, as discussed above (Figure 46).

The rod-like morphologies of BTO crystals prepared in EG volume fractions from 10 - 12.5% were highlighted as an advantage for applications in piezocatalysis, due to the fact that rods are expected to support larger bending strains than other cubic or spherical crystalline morphologies. CNF/BTO composites prepared in 5.0 vol.% and 11.0 vol.% EG and treated at 200 ^{o}C and 220 ^{o}C were tested for electromechanical response in the cantilever-oscilloscope apparatus. We hypothesized that all composites prepared with EG would generate voltages exceeding those of the composites with morphologically cubic crystals due to (a) the capacity of the rod-like crystals to sustain larger bending strains, and (b) that the crystals prepared in EG registered significant lattice distortion nearing phase-pure tetragonal (c:a ~ 1.010). However, as shown in Figure 48 -49, none of the composites prepared in EG demonstrated significant piezoelectric response. In fact, the CNF/P25 control registered a larger output voltage than the EG samples (maximum peak-to-peak voltage at the open-oscilloscope resistance was measured at 1.31 volts). The rationale for the marginal electromechanical response of the control is unclear, but may be related to oscilloscope measurement uncertainty.

The lack of electromechanical response from the composites prepared with EG may be related to several variables. Although it was our expectation that tetragonal rod-like crystals would sustain larger bending strains than cubic or spherical crystals per applied force, it is possible that the opposite is true. For example, by virtue of their shape and size, spherical and cubic crystallites tend to be more embedded (per total crystal volume) in their parent nanofibers than rod-like or other elongated morphologies. Consequently, spherical and cubic crystallites may experience more strain when the fibers are uniformly flexed (such as in a cantilever). Conversely, rod-like crystals may be more responsive to environments with abundant waste mechanical energy but limited resultant nanofiber mobility (such from turbulence induced by dead-end membrane filtration).

Another factor that may have inhibited the piezoelectric response of the composites prepared in EG is imperfect crystallization during the dissolution-precipitation nucleation process. Inada et al. (2015) reported that EG interferes with BTO nucleation by inhibiting the dissolution of Ba-Ti-OH precursors, which are the building-blocks for BTO precipitation. We believe that, as a result of this interference, EG is likely incorporated into the BTO lattice structure during crystal growth. Uptake of EG into BTO crystal structure would constitute significant point-defects, which could stymie piezoelectric response. Such a mechanism is akin to what is already widely reported for hydroxyl point-defects resulting from low- and mid-temperature hydrothermal treatment [51]. In this case, post-processing of the CNF/BTO composites prepared in EG may be needed to eliminate the point defects that likely have accumulated from the treatment in EG (e.g. secondary heat treatment to burn out the EG). Nevertheless, we believe that EG holds promise as a crystal-capping agent capable of selectively controlling BTO morphology and promoting the formation of the tetragonal crystalline phase.

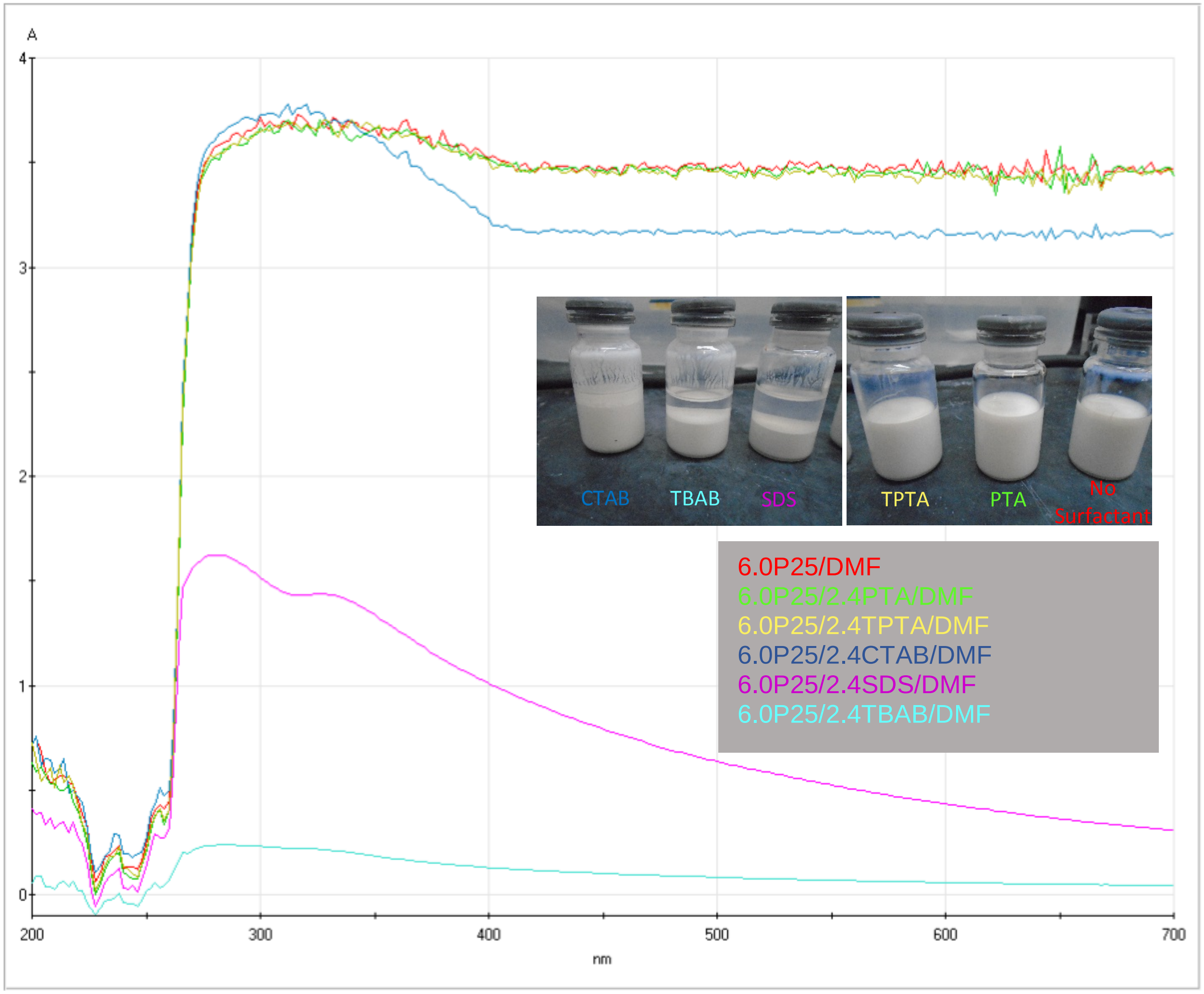

Figure 20 Absorbance scans of P25 settling tests conducted with various surfactants. Jar settling tests are also shown in the inset.

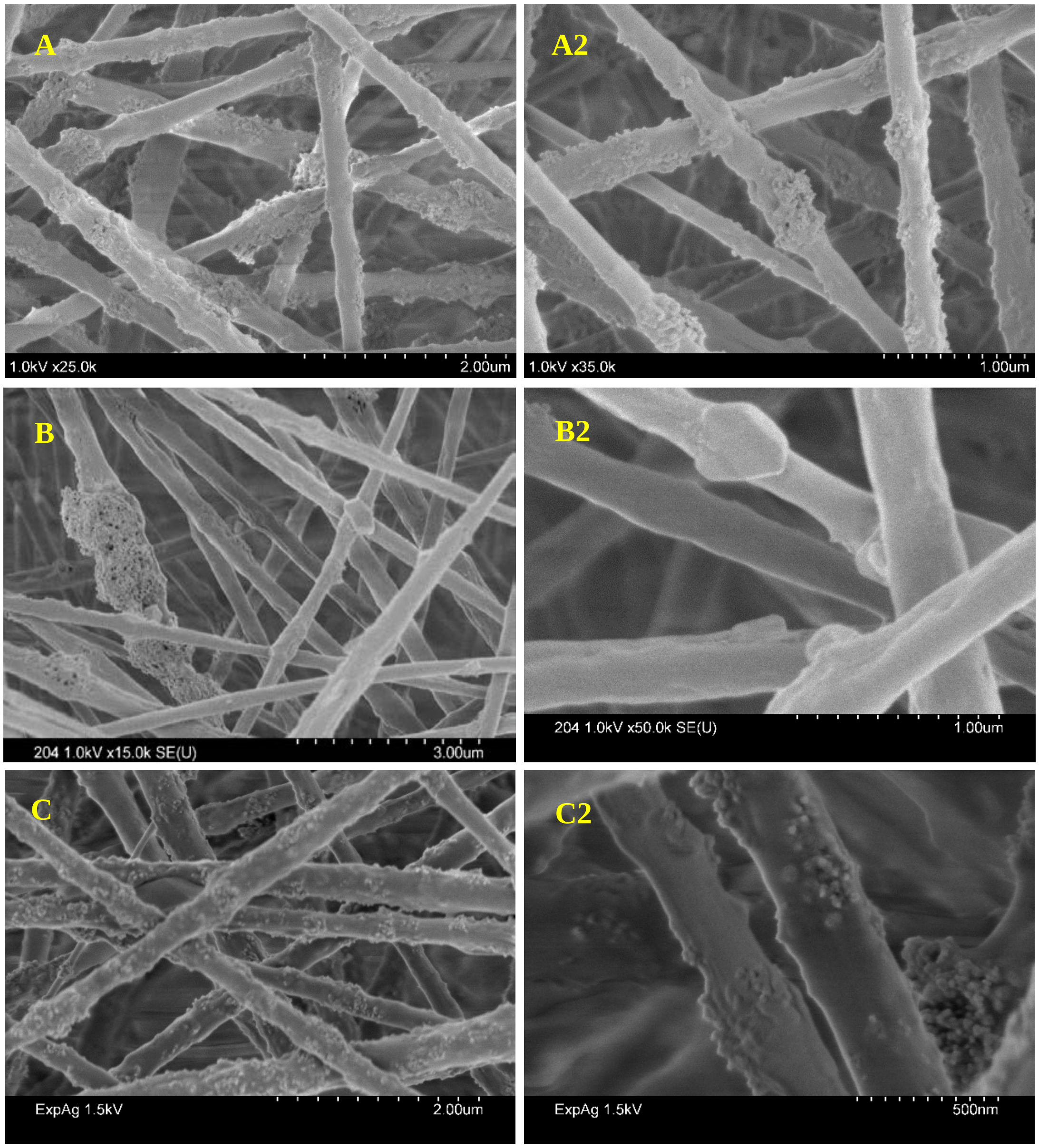

Figure 21 Electrospun PAN/6.0P25 composites with: (A, A2) no included surfactants (B, B2) 3.5 wt.% TPTA; and (C, C2) 2.4 wt.% PTA

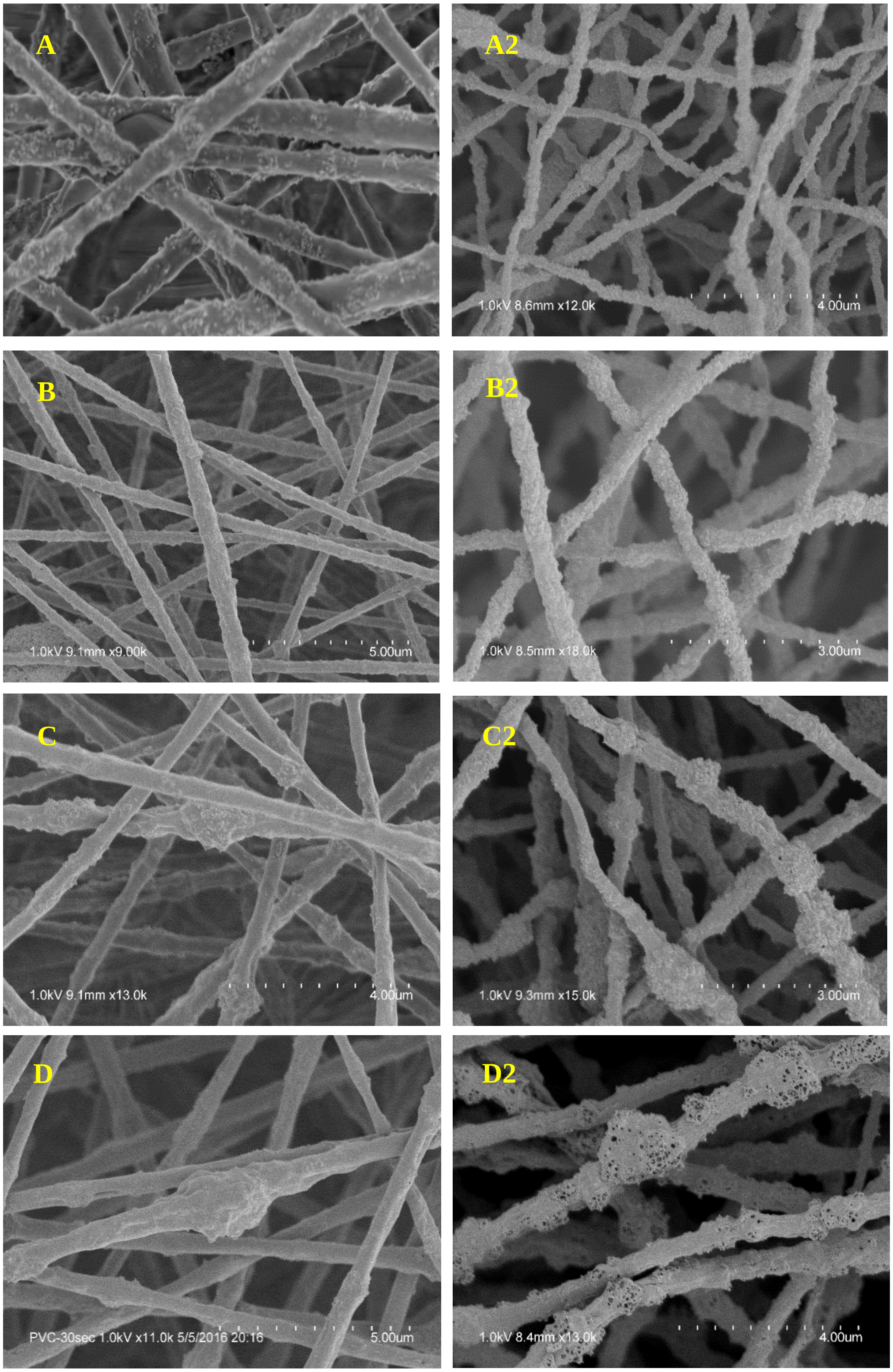

Figure 22 PTA dispersion study with (A) PAN + 6.0P25/2.4PTA, (A2) CNF + 6.0P25/2.4PTA, (B) PAN + 6.0P25/2.7PTA, (B2) CNF + 6.0P25/2.7PTA, (C) PAN + 6.0P25/3.0PTA, (C2) CNF + 6.0P25/3.0PTA, (D) PAN + 6.0P25/4.0PTA, (D2) CNF + 6.0P25/4.0PTA

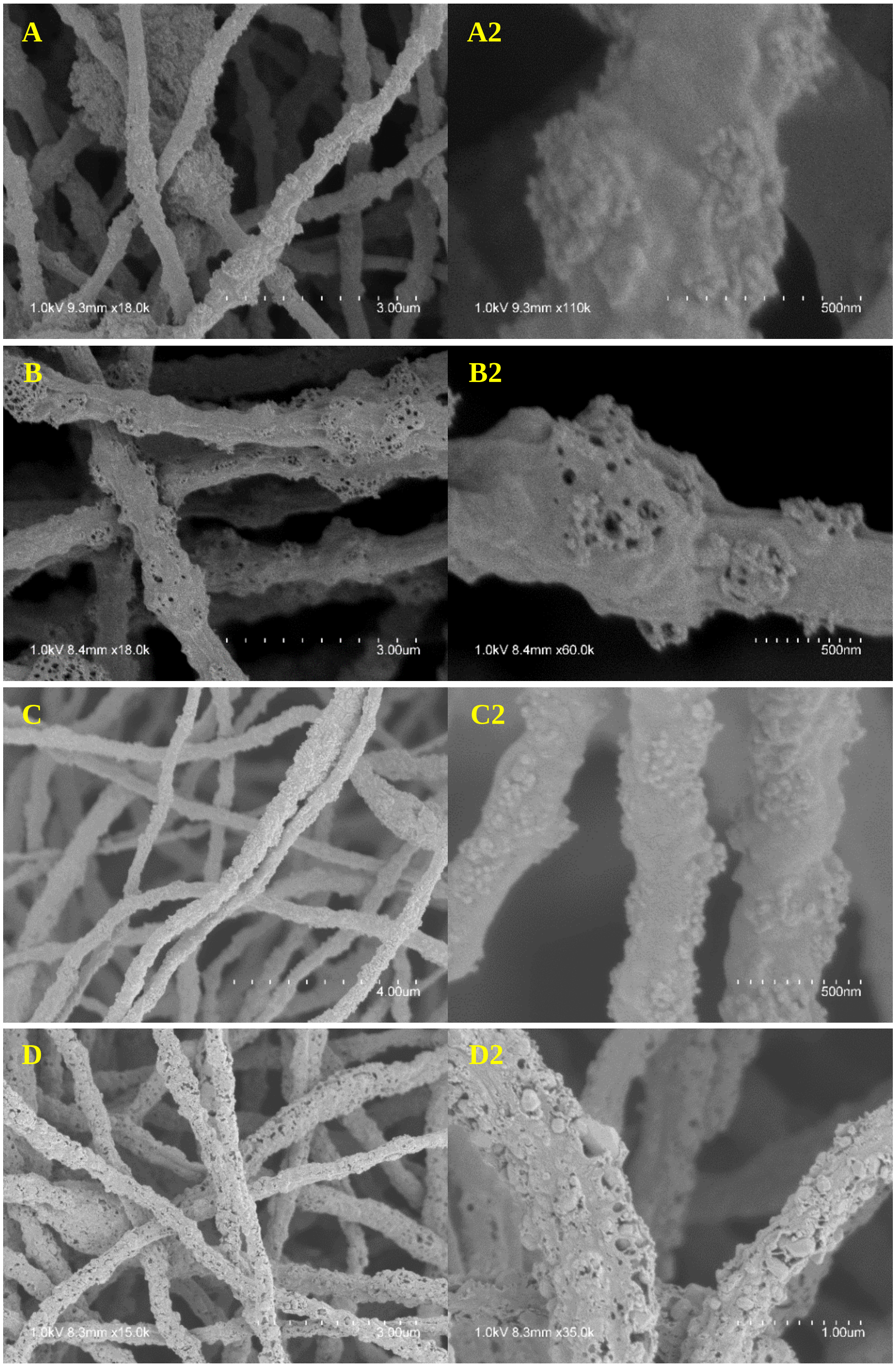

Figure 23 Carbonized composites containing (A and A2) 3.0 wt.% PTA and (B and B2) 4.0 wt.% PTA. Composites containing 2.7 wt.% were carbonized at (C and C2) 600 °C and (D and D2) 1050 °C to investigate temperature effects on mat strength and porosity.

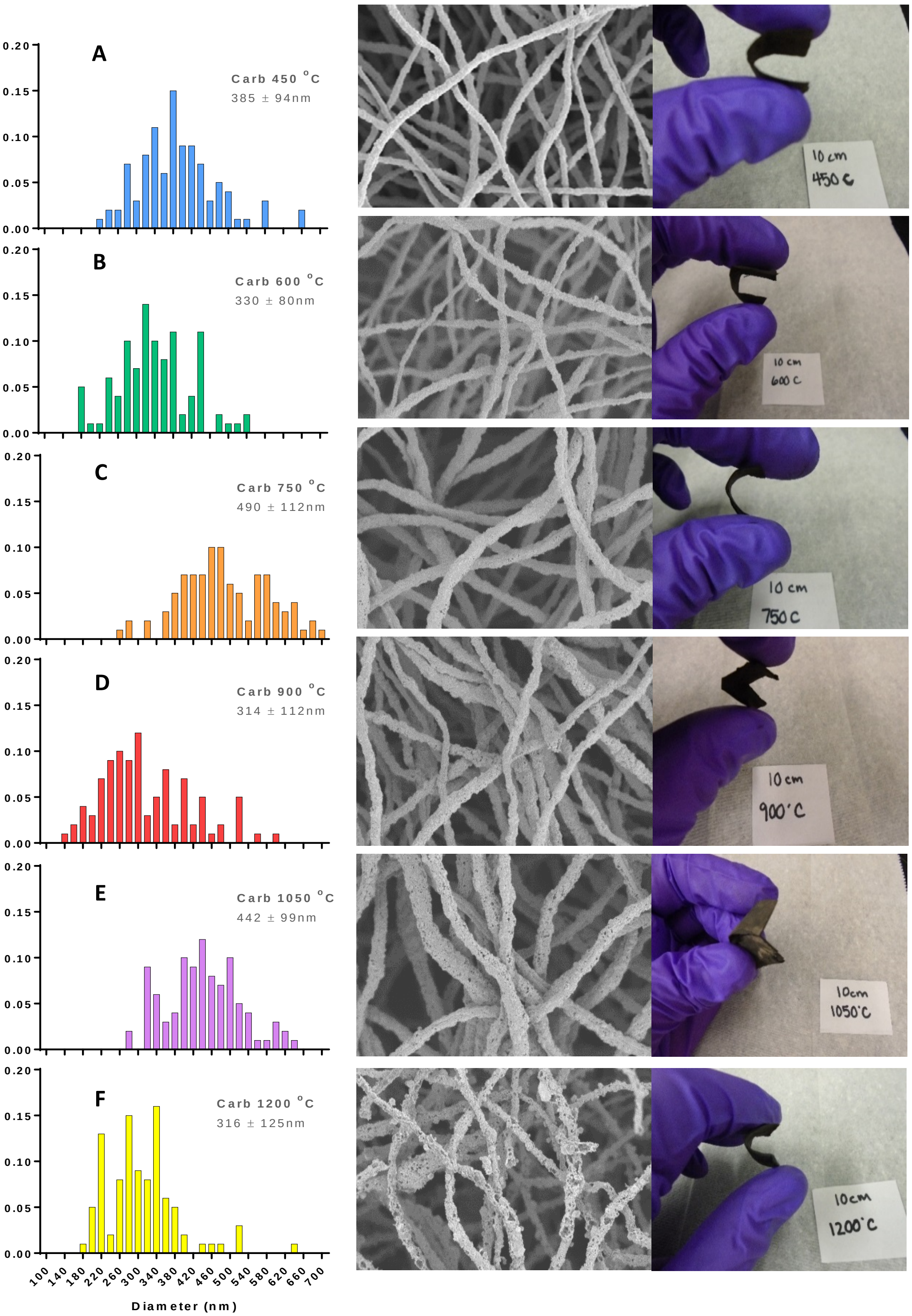

Figure 24 Diameter histogram, SEM, and qualitative fracture studies of CNF/6.0P25 mats carbonized at (a) 450 °C, (b) 600 °C, (c) 750 °C, (d) 900 °C, (e) 1050 °C, and (f) 1200 °C

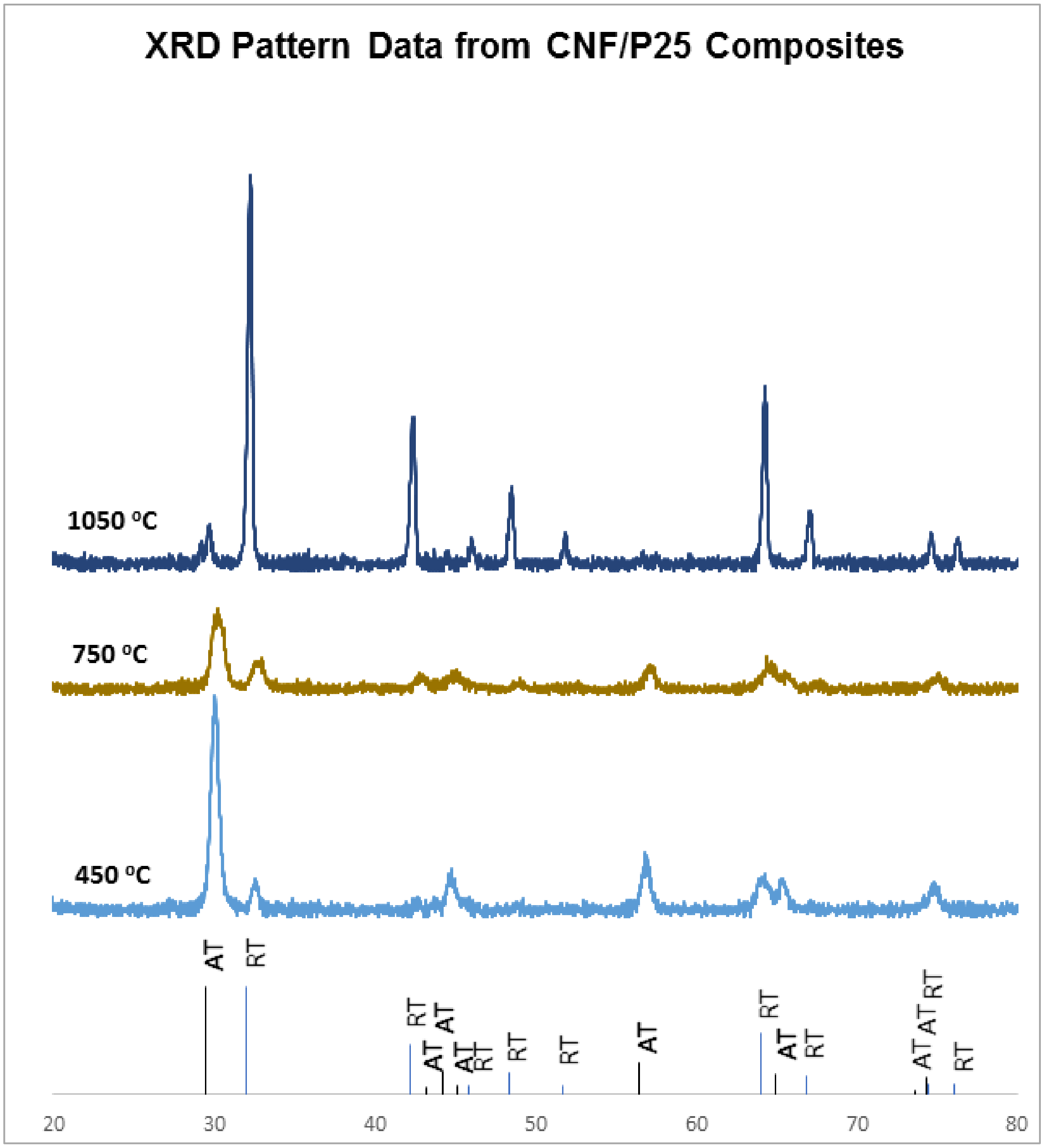

Figure 25 Increasing carbonization temperature of the composite mats leads to the conversion of available TiO_2 from anatase to rutile phase

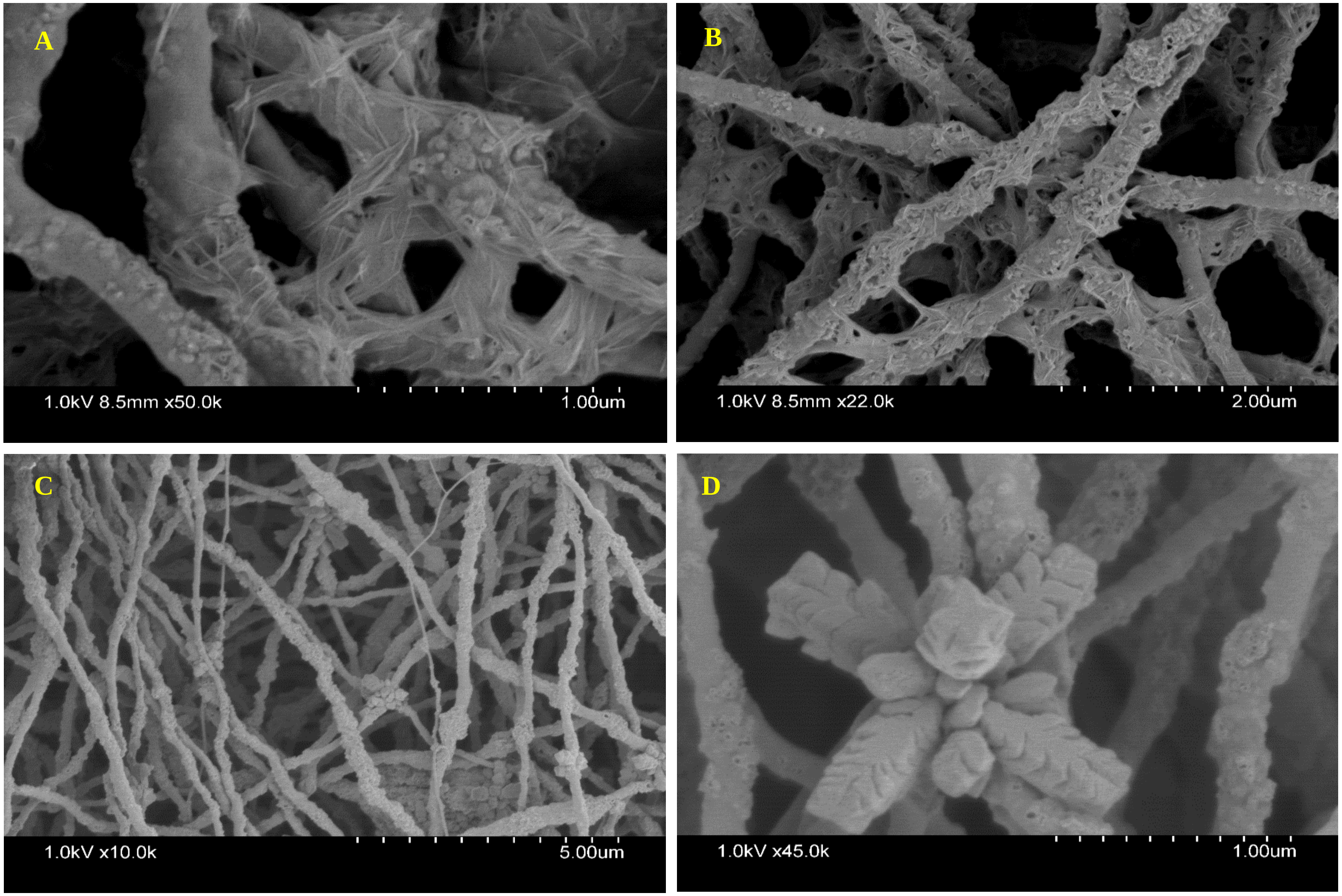

Figure 26 SEM of 'two-stage' alkaline hydrothermal synthesis: (A and B) conversion to sodium titanate; (C and D) ion exchange reaction producing barium titanate

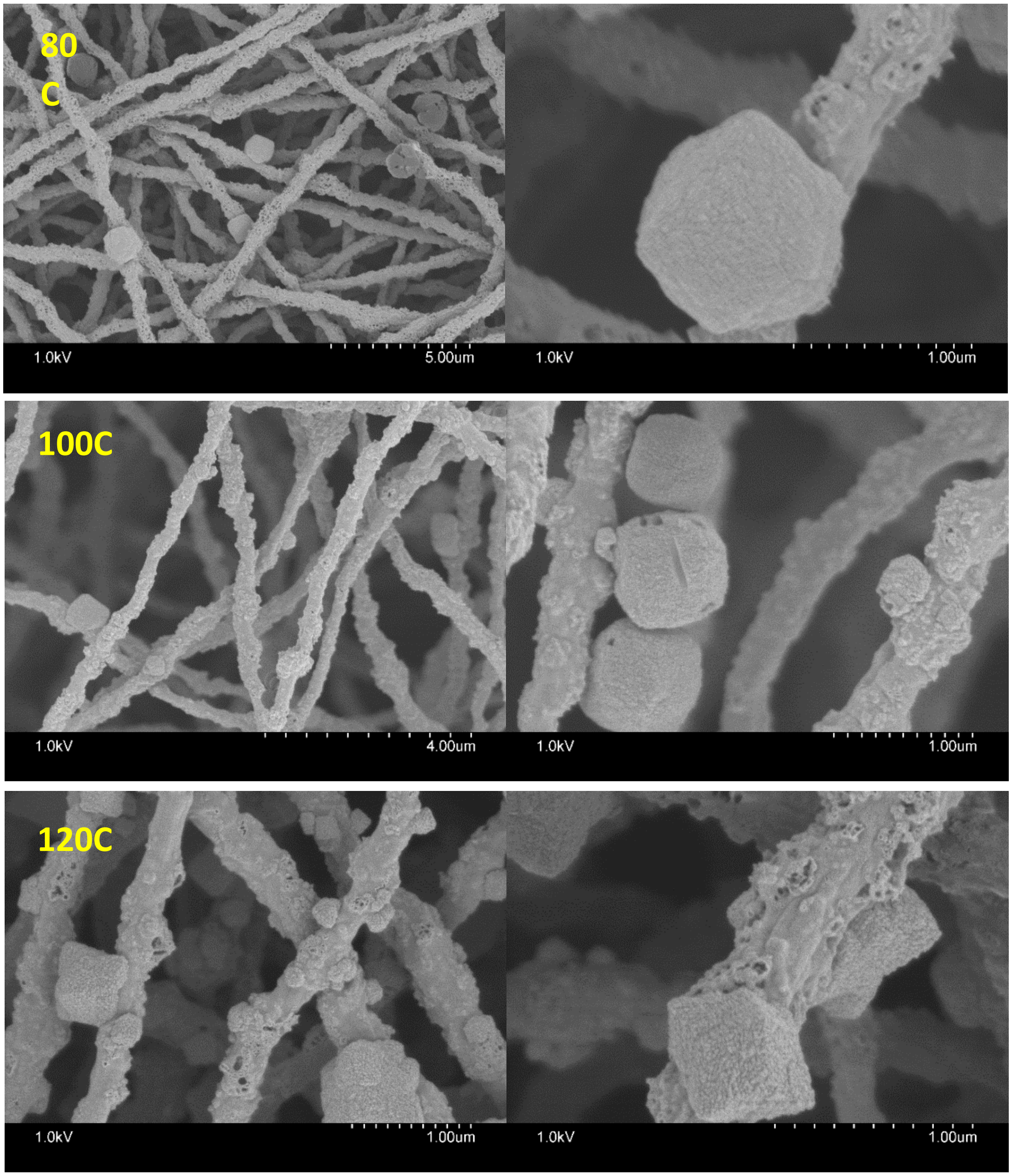

Figure 27 SEM images of the hydrothermally treated CNF/BTO composites at (a) 80 ^{o}C, (b) 100 ^{o}C and (c) 120 ^{o}C

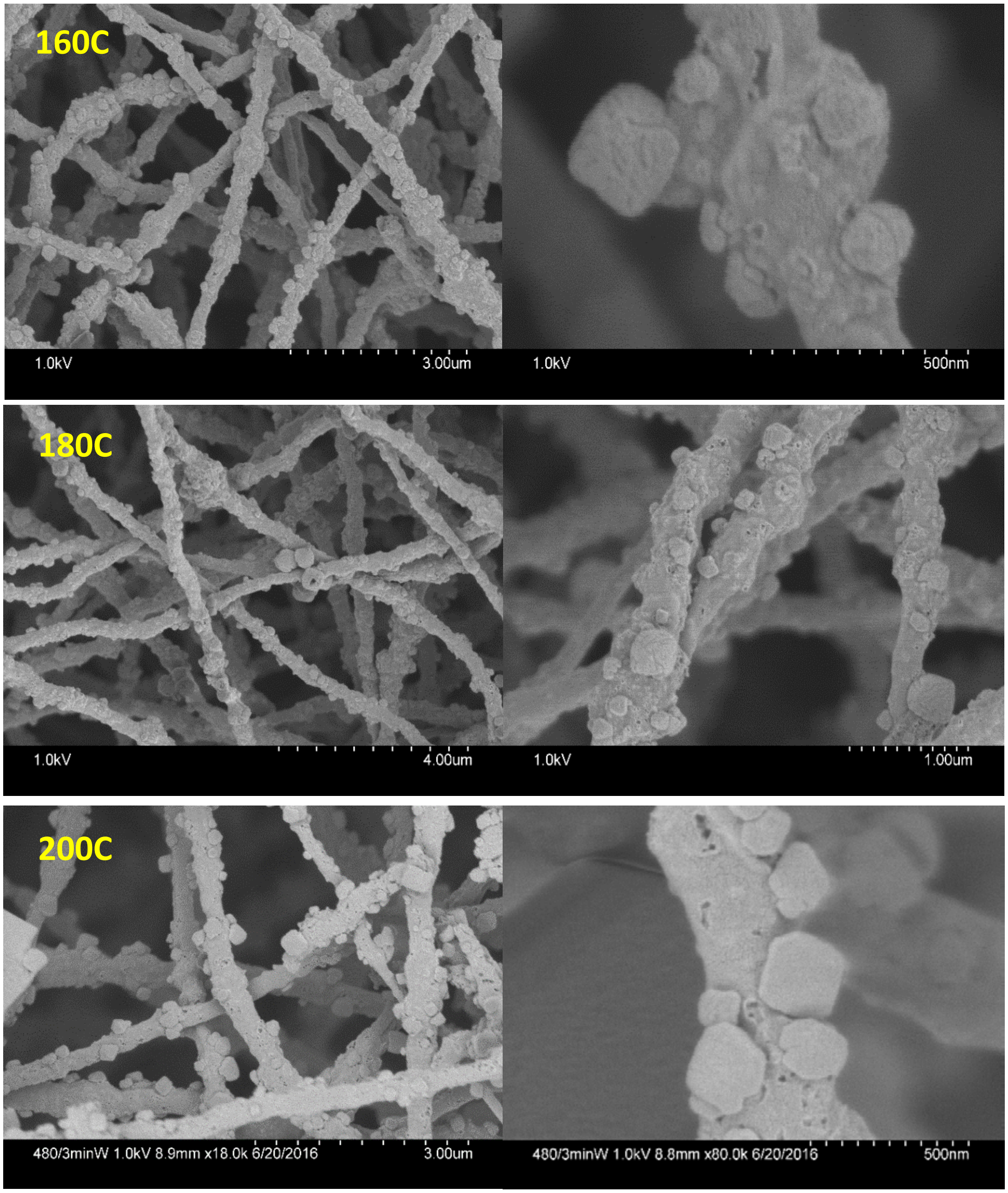

Figure 28 SEM images of the hydrothermally treated CNF/BTO composites at (a) 160 ºC, (b) 180 ºC, and (c) 200 ºC

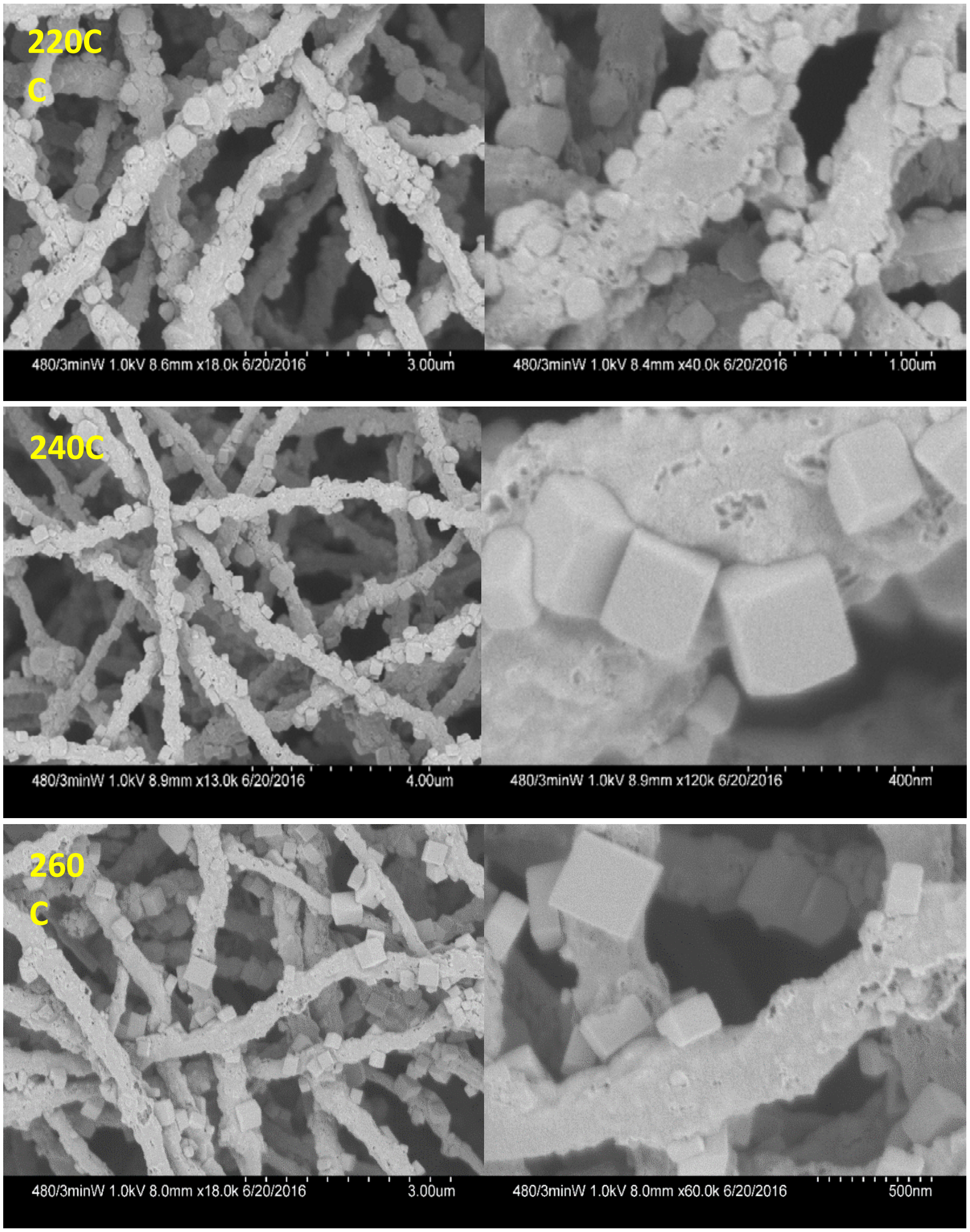

Figure 29 SEM images of the hydrothermally treated CNF/BTO composites at (a) 220 ^{o}C, (b) 240 ^{o}C, and (c) 260 ^{o}C

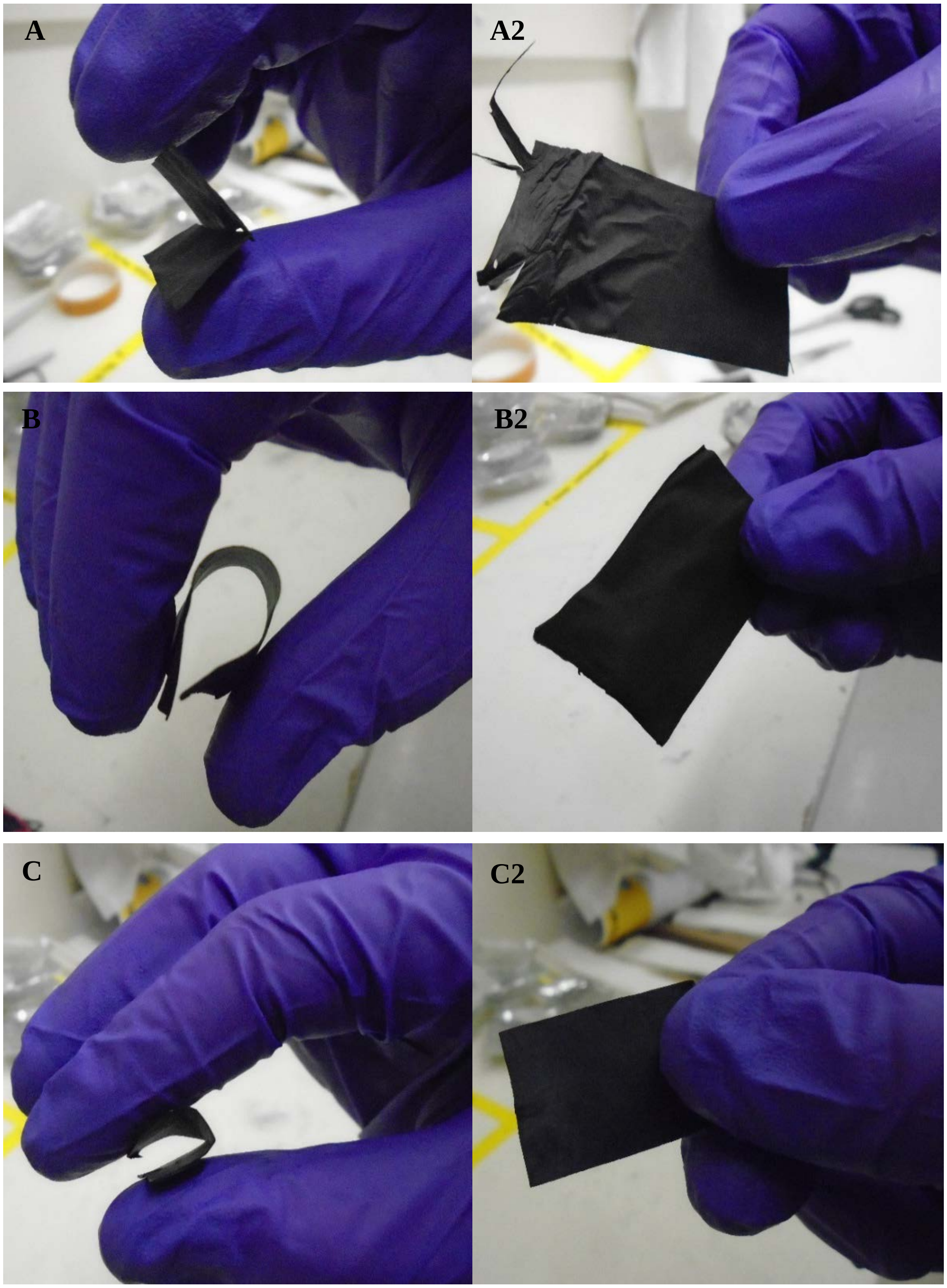

Figure 30 Composite mat flexibility of (A and A2) CNF/6.0P25, (B and B2) CNF/6.0P25 prepared with 2.7 wt.% PTA, and (C and C2) CNF/BTO prepared with 6.0 wt.% P25 and 2.7 wt.% PTA in PAN precursor mat

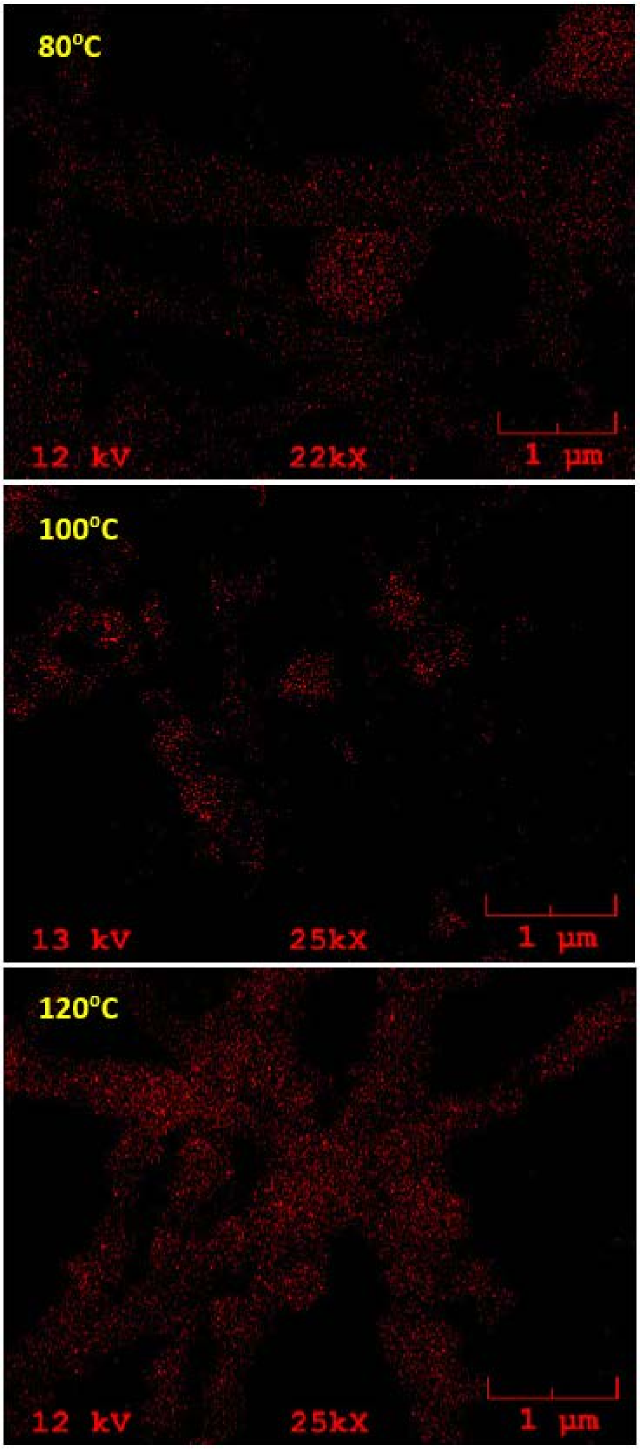

Figure 31 Ba EDS maps of CNF/BTO composites generated at 80º C, 100º C, and 120º C. Red dots represent detected Ba in the nanofibers

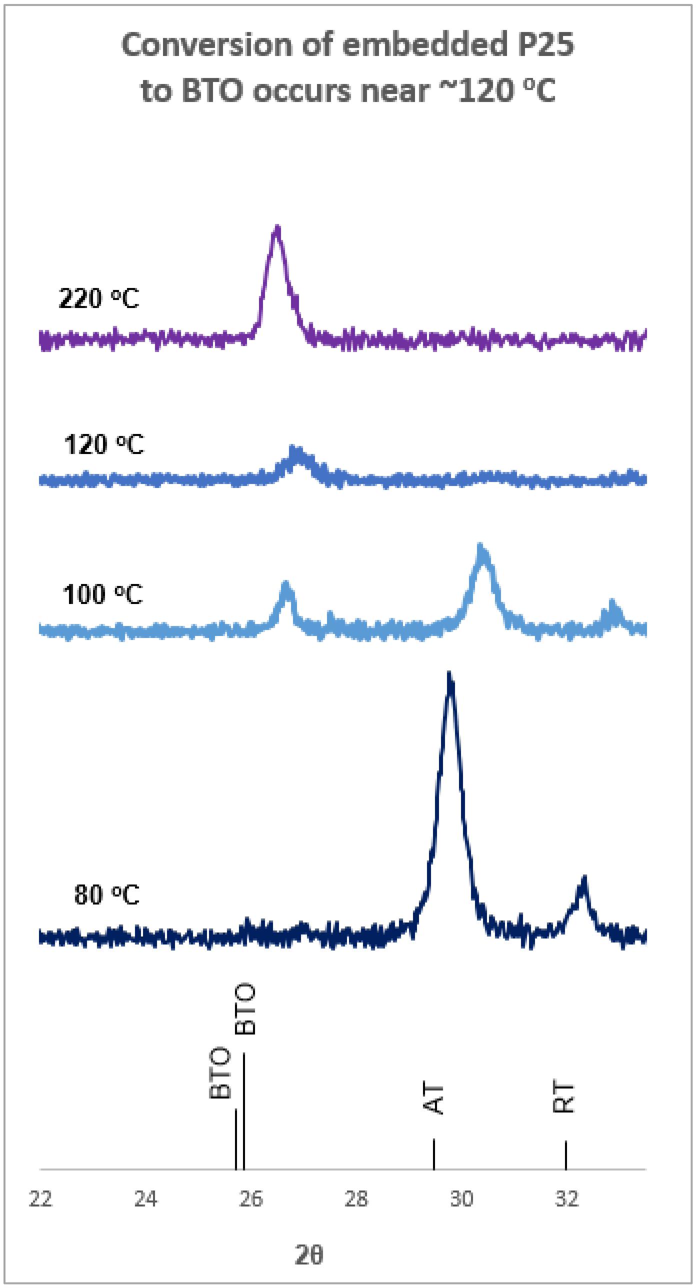

Figure 32 Composites treated at 80 ^{o}C retained anatase (AT) and rutile (RT) peaks; 100 ^{o}C hydrothermal treatment showed diminished AT and RT peaks with the growth of marginal BTO peaks; hydrothermal treatment at 120 ^{o}C eliminated trace AT and RT peaks; 220 ^{o}C treatment showed the growth of significant BTO peaks

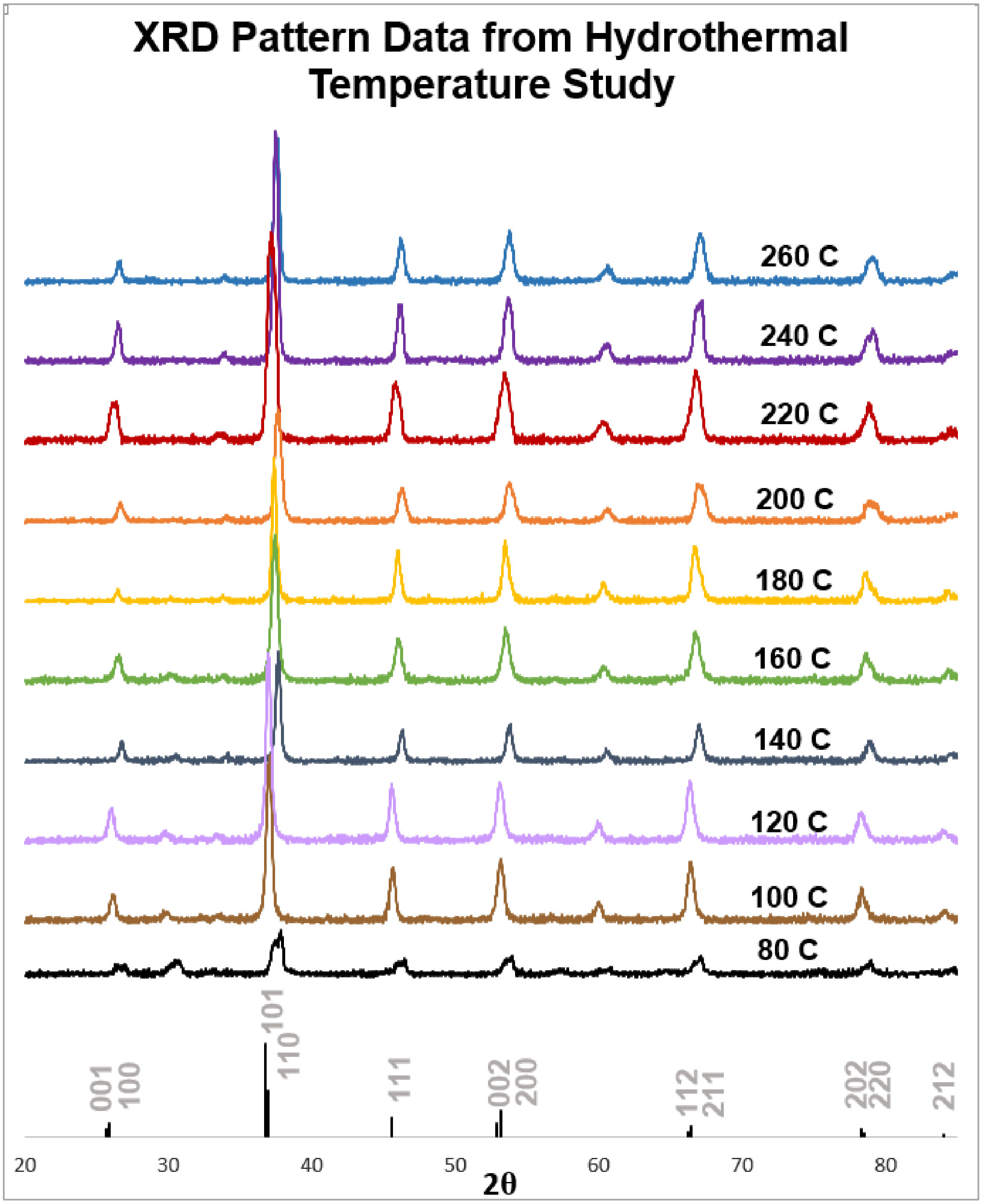

Figure 33 XRD patterns of CNF/BTO composites hydrothermally treated between 80° - 260° C

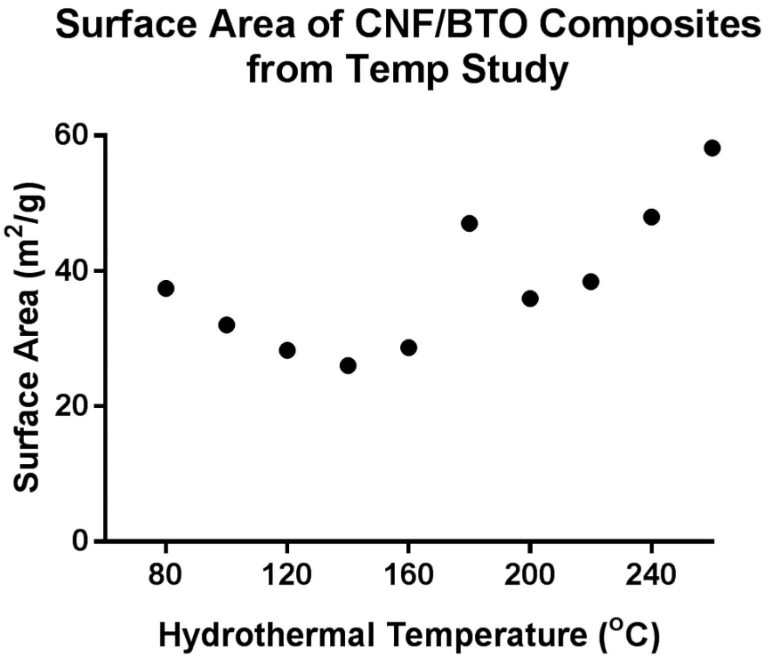

Figure 34 BET surface area measurements of hydrothermal temperature study samples

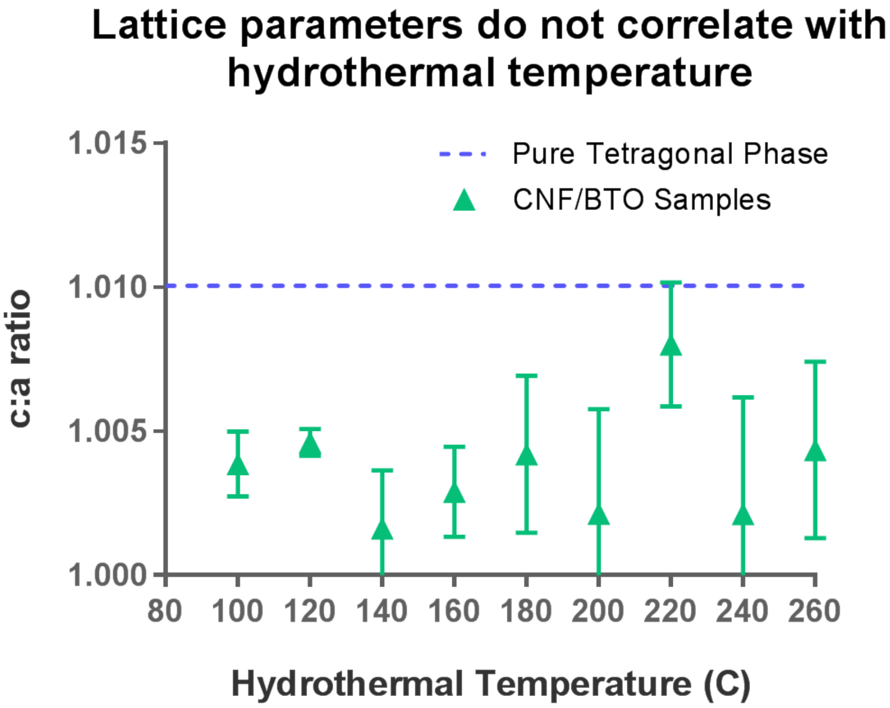

Figure 35 c:a lattice ratios calculated from the XRD scans of the hydrothermal temperature samples (prepared in triplicate)

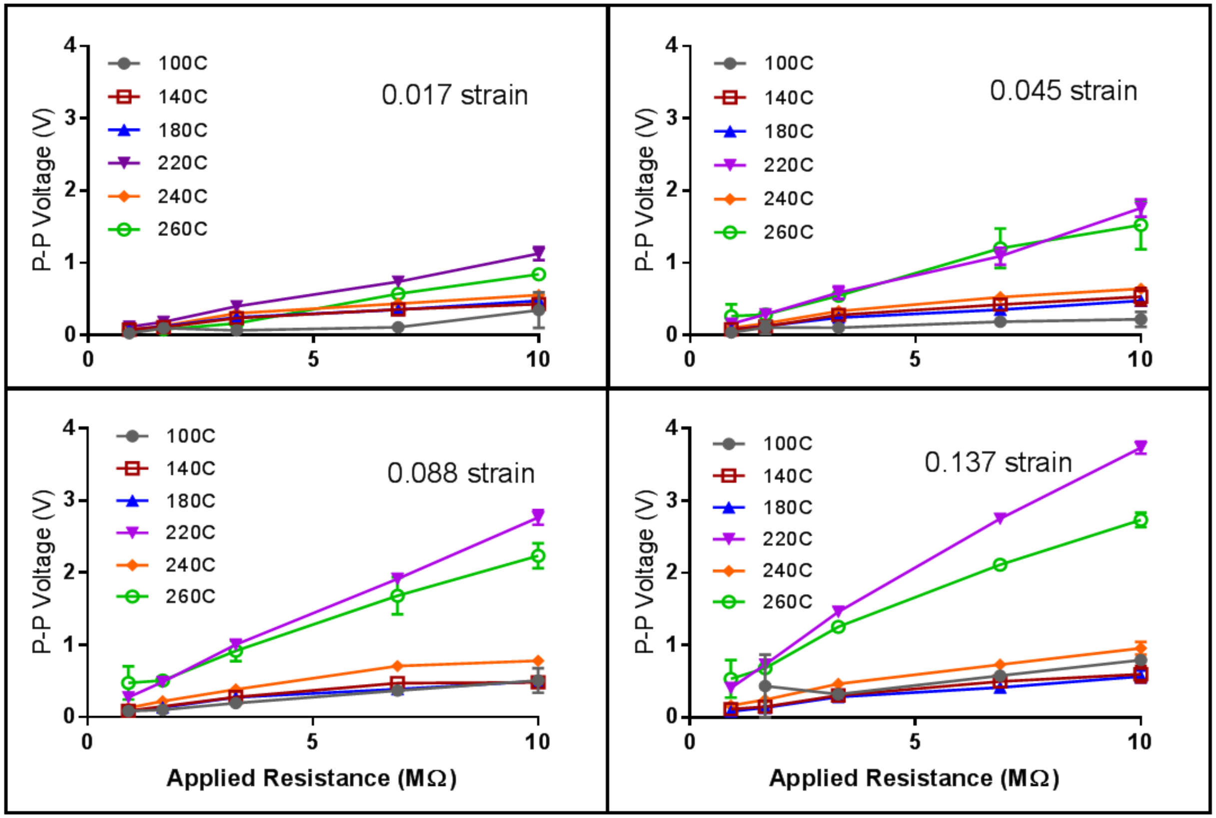

Figure 36 Output peak-to-peak voltages of hydrothermal temperature samples at varied resistance loads and strain rates. In general, output voltage increases with both resistance load, applied strain, and hydrothermal treatment temperature, with treatment temperatures exceeding 200 °C exhibiting the largest electromechanical response

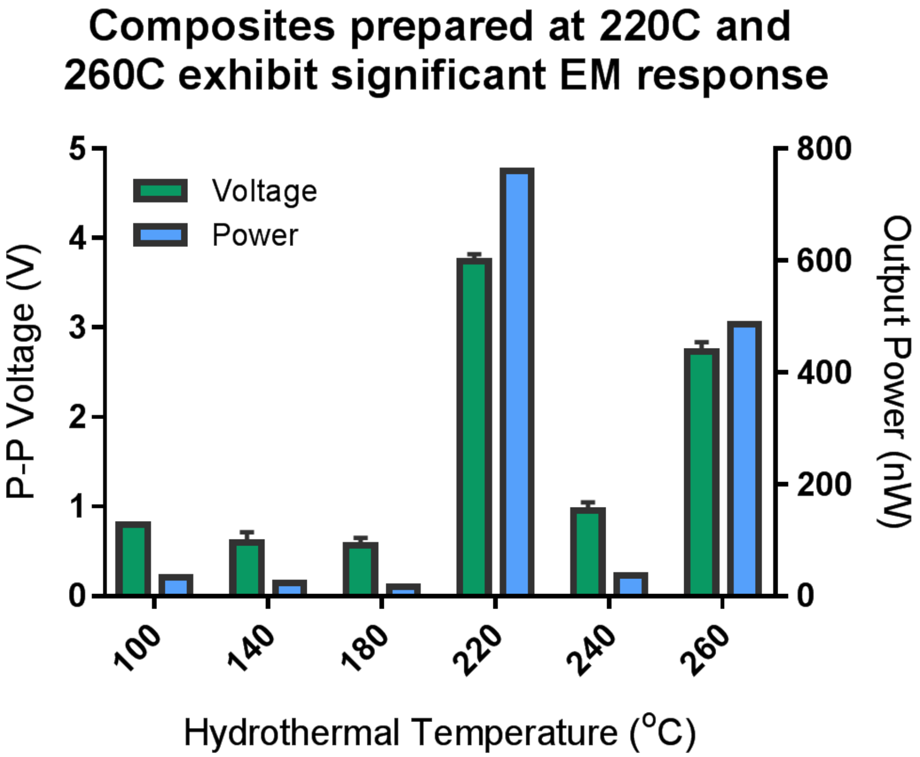

Figure 37 Output voltage and power of hydrothermal samples tested at 0.137% strain and open circuit oscilloscope resistance.

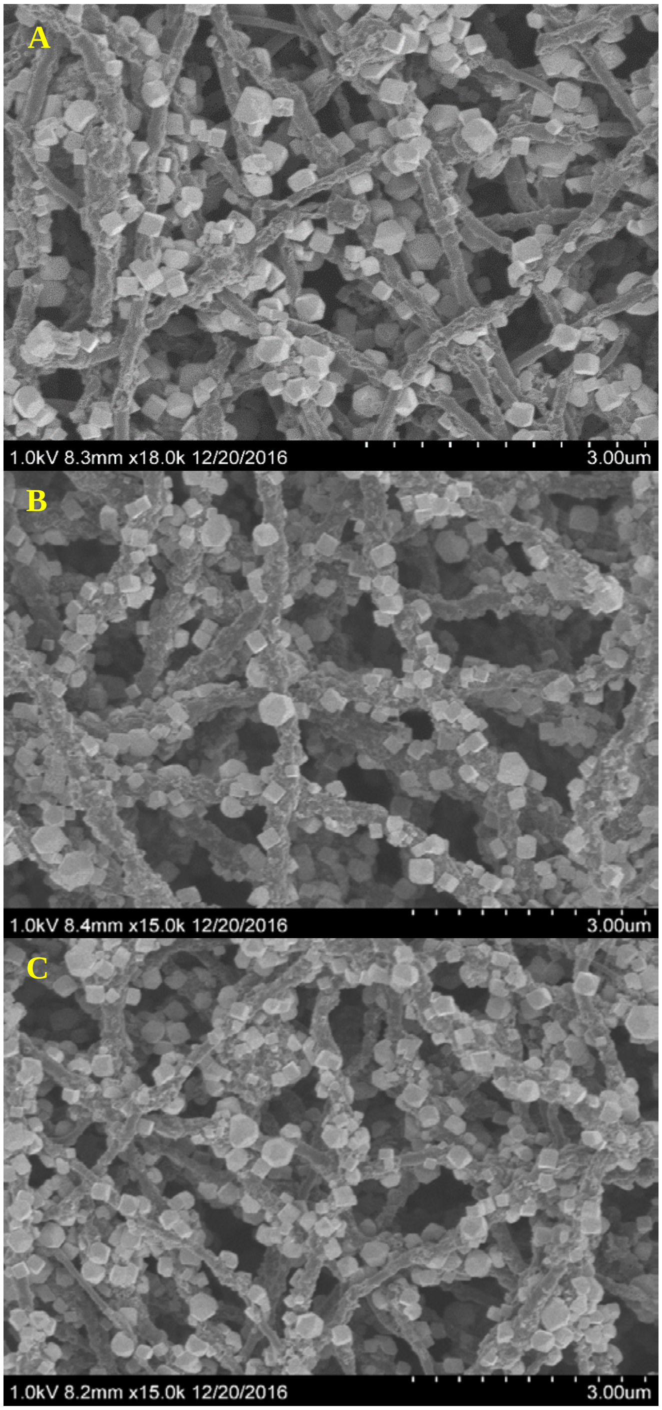

Figure 38 SEM images of varied barium titanate mass loading composites. CNF precursors were prepared with (a) 6.0 wt.% P25, (b) 9.0 wt.% P25, and (c) 12.0 wt.% P25 and hydrothermally treated for 24h at 220 °C

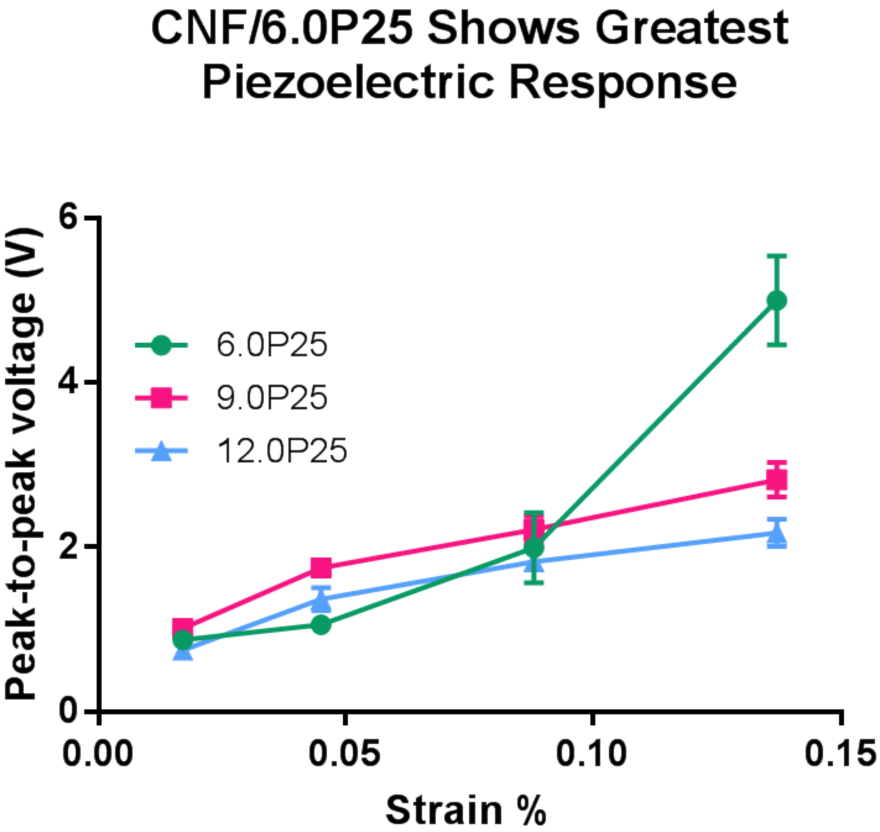

Figure 39 Composites prepared with 6.0P25 generate largest voltage at maximum strain, but 9.0 wt.% and 12.0 wt.% composites outperform at lower strains

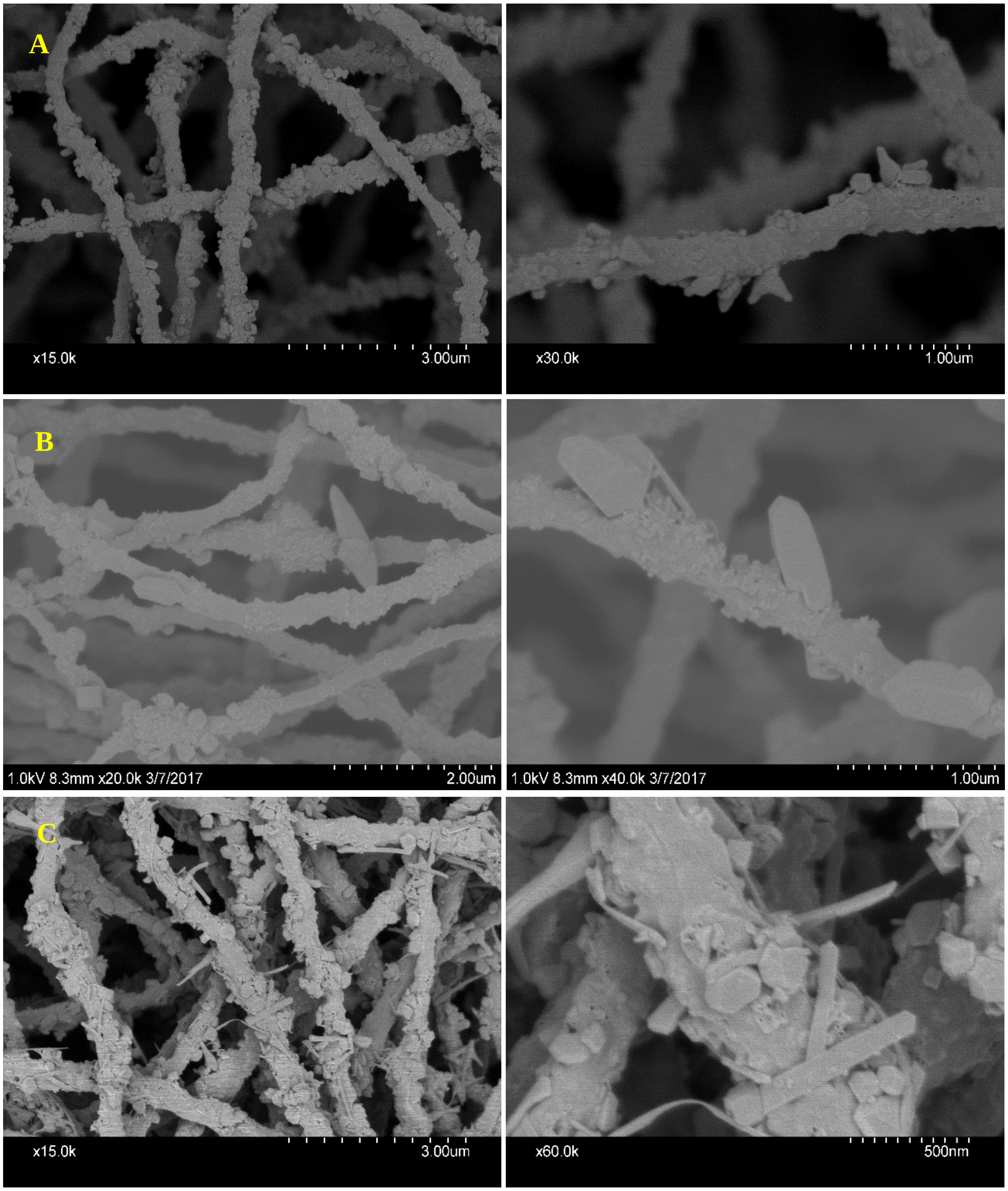

Figure 40 CNF/6.0P25 hydrothermally treated at 200 °C for 24h by the 'one-pot' method in (a) 5.0 vol.% EG, (b) 7.5 vol.% EG, (c) 10.0 vol.% EG, and (d) 11.0 vol.% EG

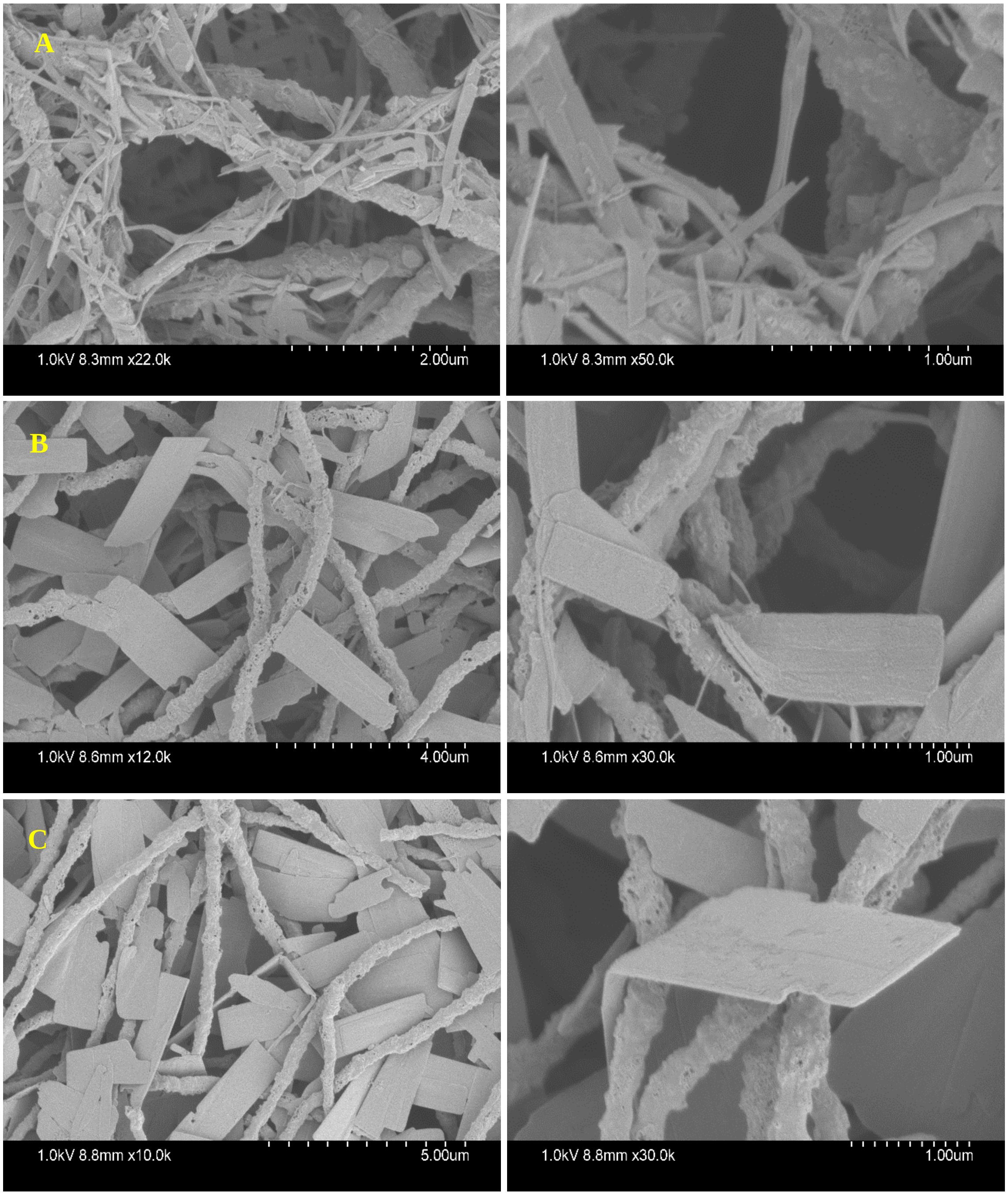

Figure 41 CNF/6.0P25 hydrothermally treated at 200 °C for 24h by the 'one-pot' method in (a) 12.5 vol.% EG, (b) 15.0 vol.% EG, and (c) 17.5 vol.% EG

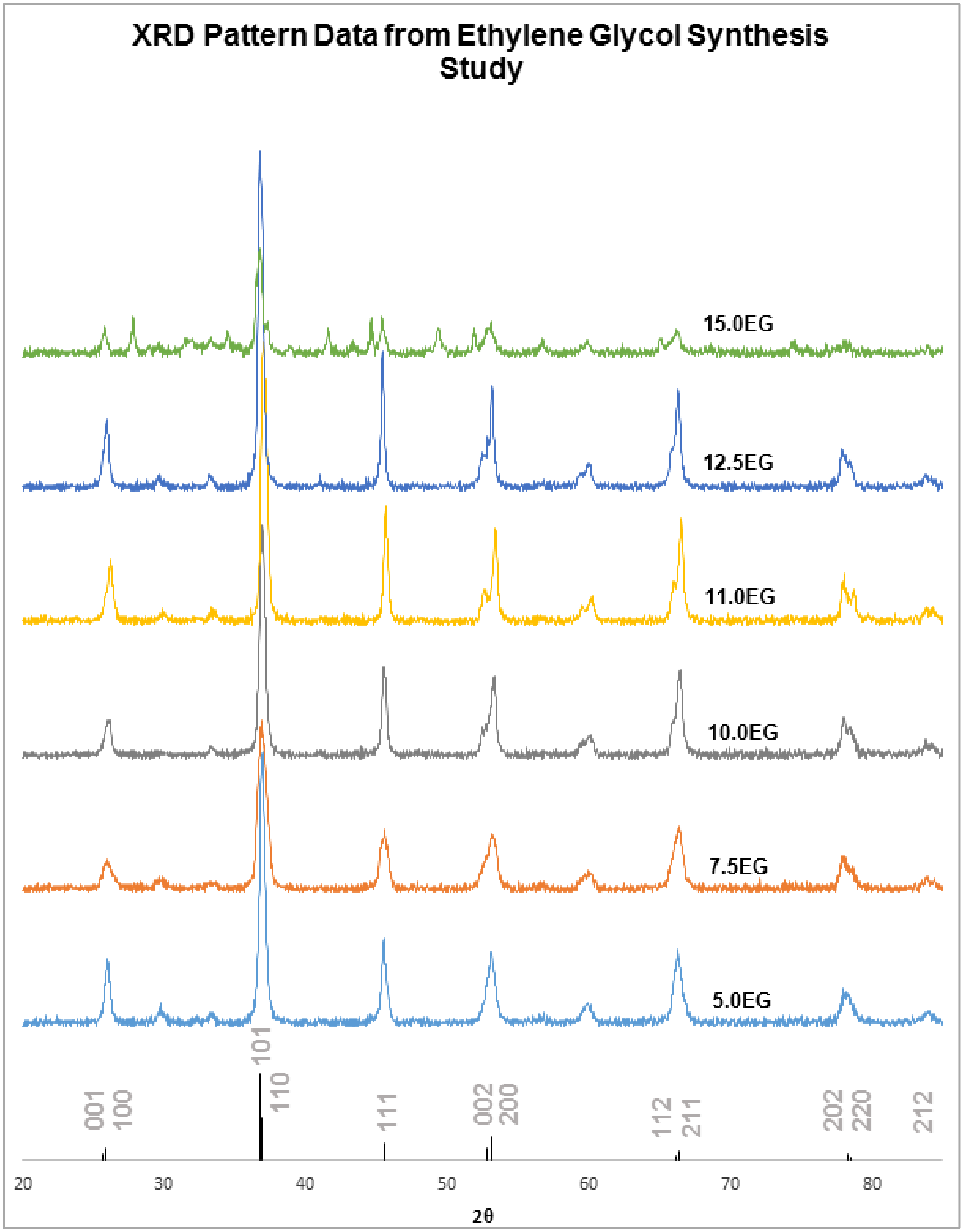

Figure 42 XRD pattern data from 'one-pot- synthesis of CNF/6.0P25 composites with volumetric fractions of ethylene glycol between 5-15%

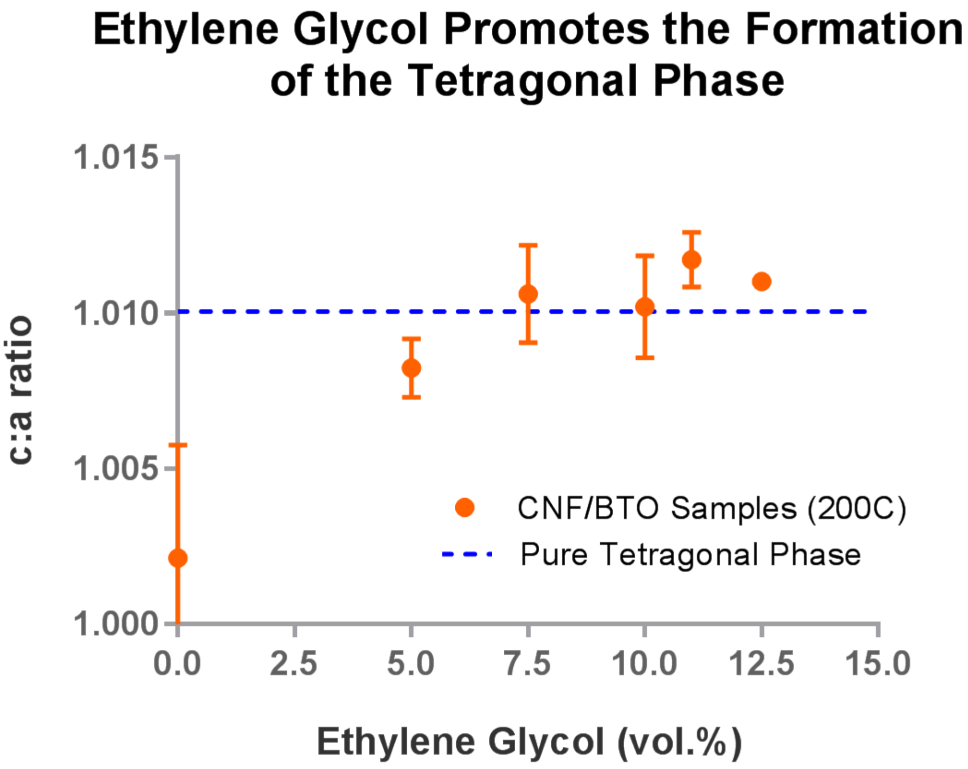

Figure 43 Lattice ratios of CNF/6.0P25 composites hydrothermally synthesized in various volumetric fractions of ethylene glycol

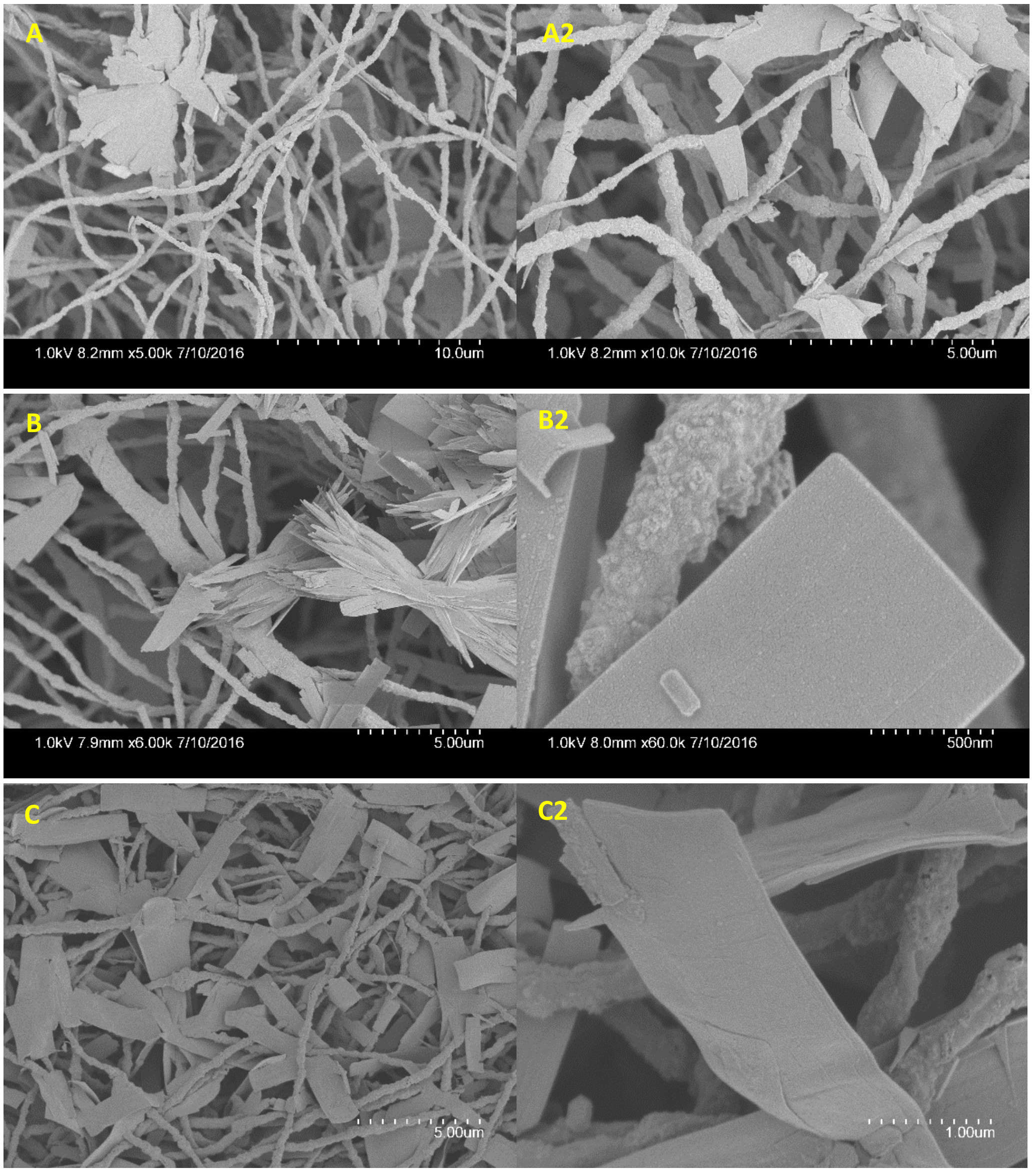

Figure 44 CNF/P25 composites treated in 10.0 vol.% EG for 24h at (A and A2) 140 ºC, (B and B2) 160 ºC, (C and C2) 180 ºC via the 'one-pot' hydrothermal method

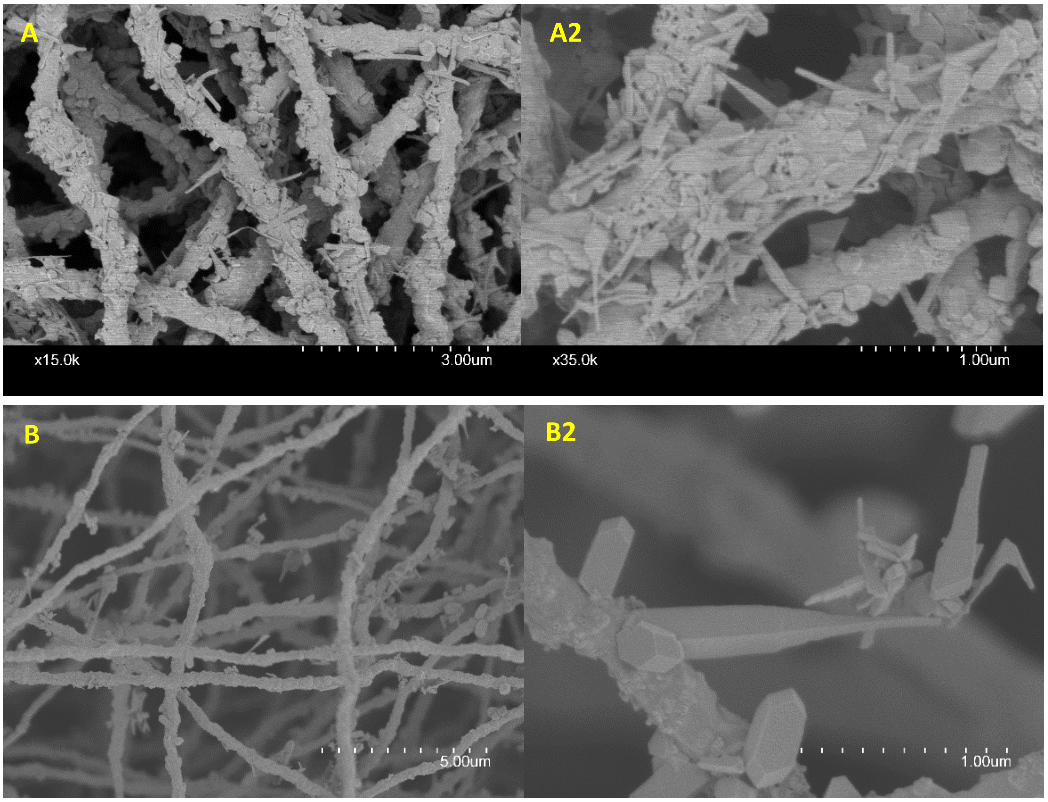

Figure 46 CNF/P25 composites treated in 10.0 vol.% EG for 24h at (A and A2) 200 °C and (B and B2) 220 °C via the 'one-pot' hydrothermal method

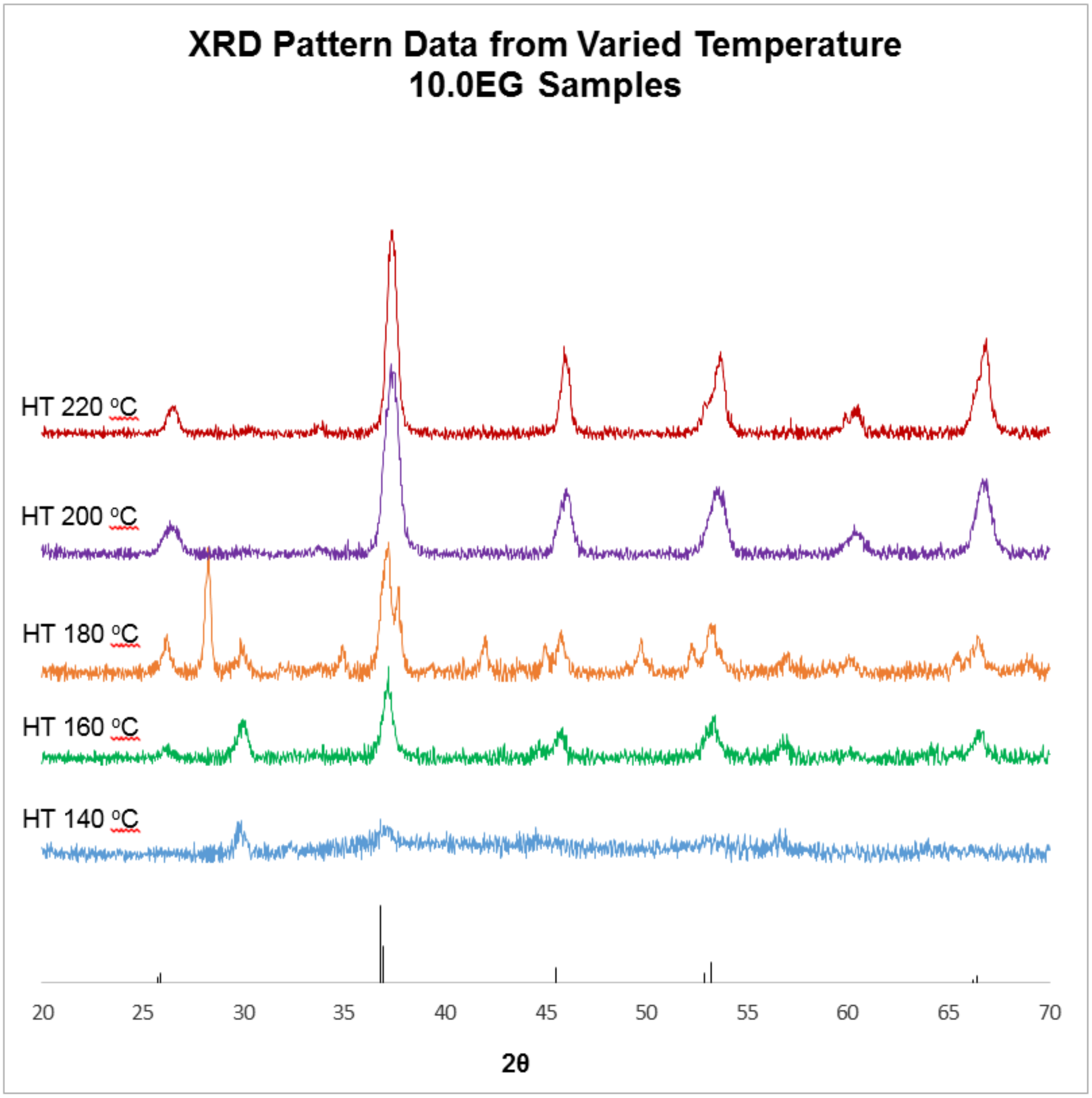

Figure 47 XRD Pattern Data from Varied Temperature 10.0EG Samples

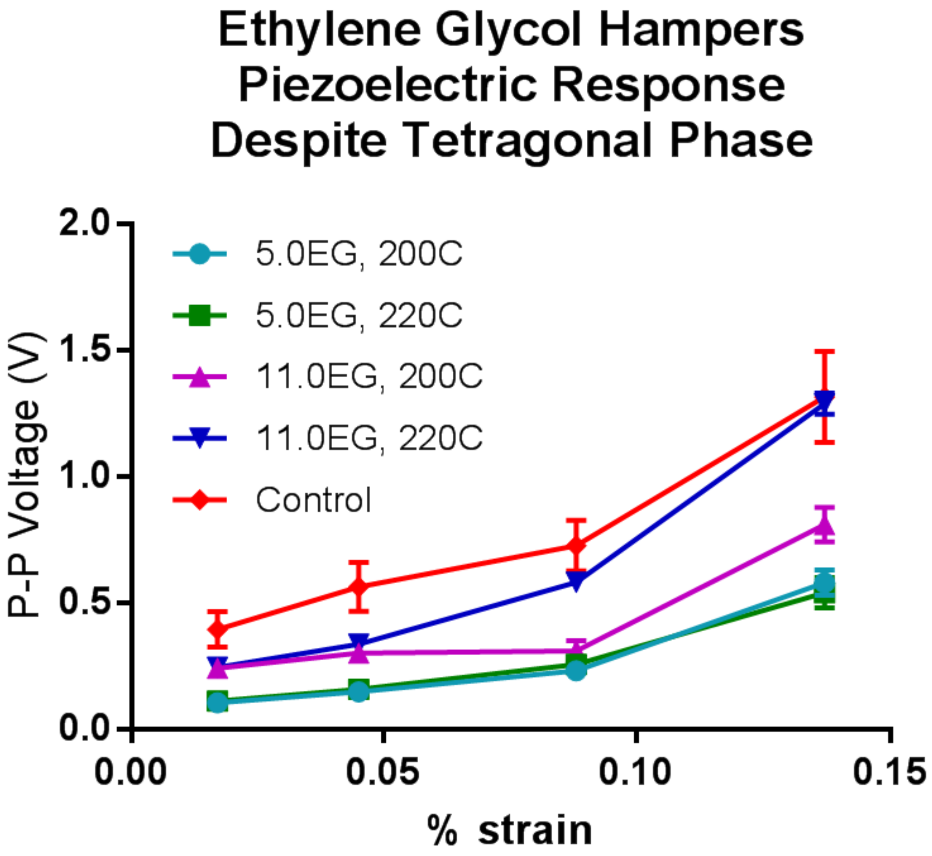

Figure 48 Output peak-to-peak voltage of hydrothermal samples prepared with various fractions of ethylene glycol tested as a function of strain rate

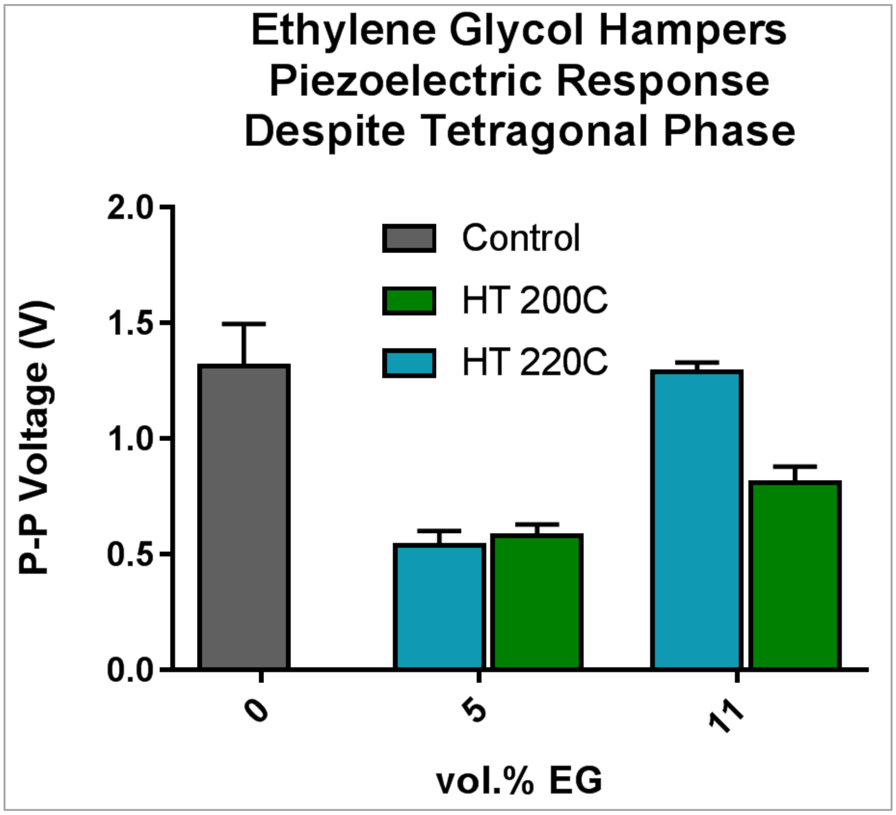

Figure 49 Output peak-to-peak voltage of hydrothermal samples prepared with various fractions of ethylene glycol tested at 0.137% strain and open circuit oscilloscope resistance.

CHAPTER 5 CONCLUSIONS

5.1 Project summary

Engineered piezoelectric materials may be able to supplement potable water treatment processes by spontaneously harvesting and converting waste mechanical energy into useful electrochemical energy available for pollutant degradation. This energy may be applied via direct catalysis (i.e. piezoelectric crystals constitute reactive sites in aqueous solution for adsorption and pollutant decay) or as external power sources either for catalysis or improving process efficiency. In this work, we are among the first to synthesize composite nanofibrous piezoelectric materials for applications in water purification. As piezoelectric properties are intrinsically tied into the mechanical properties of the parent material, this work strove to emphasize material durability and strength in addition to optimizing the electromechanical properties of the barium titanate crystals embedded in the carbon nanofiber matrix.

In the development of novel nano-piezoelectric composites, this work was divided into five sub-studies. Chapter 3 focused on proof-of-concept batch sonication studies performed with suspended BTO nanoparticles to demonstrate piezocatalytic degradation of organic contaminants. Chapter 4 detailed the material development of the CNF/BTO composites, wherein a carbonization/strength study was performed to optimize composite mat bending flexibility, a hydrothermal temperature study investigated the impacts of temperature on BTO crystal morphology and piezoelectric response, and a BTO mass loading and ethylene glycol ‘crystal-capping’ study explored the effects of BTO density, morphology, and phase on the electromechanical properties of the composite mats.

In Chapter 3, we performed batch sonication experiments to compare the piezocatalytic properties of commercial tetragonal barium titanate materials with those of nanocrystals synthesized with the alkaline hydrothermal method developed for the CNF/BTO composites. It was found that tetragonal commercial BTO powder did not contribute to the decolorization of AO7 significantly beyond that of the control. Unlike the commercial powder, the addition of BTO nanocrystals hydrothermally prepared in a solution of 6.5 vol.% ethylene glycol significantly accelerated the rate of AO7 decolorization.

The carbonization study was successful towards the development of flexible and resilient CNF/P25 composites. The inclusion of phthalic acid improved both the dispersion of the embedded Aeroxide® P25 nanoparticles in the polymer nanofibers as well as substantially improving the bending flexibility of composite mat following carbonization. Moreover, varying pyrolysis temperatures resulted in composites that were ductile and cohesive even after hydrothermal treatment at elevated hydrothermal treatment temperatures.

We have shown in the hydrothermal temperature study that temperature influences the piezoelectric properties of the composite materials. Hydrothermal synthesis temperatures exceeding 200 ^{o}C produced BTO crystals that generated 2 volts / cm^2 of mat at strains of 0.138%. Changes to BTO crystal morphology and phase were also evident as a function of temperature. Composites treated at 80 ^{o}C exhibited very low degrees of P25 conversion to BTO. However, the thermodynamic transition to BTO was observed to occur near 100 ^{o}C for this system. In general, increasing hydrothermal temperatures led to improved crystallinity and increased BTO crystal density as a larger fraction of embedded

P25 nanoparticles were converted to BTO in-situ. Treatment at 220 °C and beyond resulted in the formation of highly symmetrical cubic crystal morphologies.

Contrary to our expectations, piezoelectric activity did not scale with BTO loading. Composites prepared with 9.0 wt.% and 12.0 wt.% P25 showed markedly less piezoelectric response than the 6.0 wt.% P25 composite at the maximum tested strain of 0.138%. Instead, composite piezoelectric response appeared to correlate with the degree of tetragonality in the composite mats. Composites prepared with 6.0P25 exhibited the largest lattice ratio of the varied-BTO samples and consequently registered the largest peak-to-peak voltages when flexed.

Furthermore, the inclusion of ethylene glycol as a crystal capping agent during ‘one-pot’ alkaline hydrothermal synthesis promoted the anisotropic growth of BTO in the carbon nanofiber matrix. Moreover, as registered with XRD, resultant BTO morphologies were also nearly phase-pure tetragonal crystalline materials. Resulting BTO crystal morphologies included ‘nanorods’ and ‘nanosheets’, or agglomerates of ‘nanospears’. We had hypothesized that the development of crystal morphologies with large aspect ratios would support larger bending strains and therefore generate larger voltages when the mat was flexed. However, electromechanical testing of the EG composites showed little to no piezoelectric response. In review, we believe that this is likely due to the persistence of EG within the BTO crystal structure following hydrothermal treatment, thereby leading to point-defects in the lattice structure (akin to the point defects commonly observed with hydroxyl ions following low temperature hydrothermal treatment). Moving forward, we hypothesize that post-treatment of the EG composites (such as a heat treatment) may eliminate EG from the lattice structure while preserving the tetragonal phase, and ultimately restore the piezoelectric properties to the composites.

5.2 Future work

Our study has made significant advancements in the development of composite piezoelectric materials specifically tailored for applications in water treatment. However, we recognize that there are still gaps in knowledge in the electromechanical and catalytic properties of these materials that warrant further investigation. The specific piezoelectric properties such as the piezoelectric strain constants, electromechanical coupling factors, and voltage constants of the hydrothermally synthesized BTO crystals have yet to be determined. A study on how the piezoelectric coefficients vary with different synthesis conditions would be valuable in selecting optimized materials.

The piezoelectric response may also be improved by electrical poling of the composite materials, as is usually performed on piezoelectric ceramics. Doing so could align randomly oriented dipoles in the BTO crystals, and therefore promote a uniform electrical response to axial strain.

Charge separation within the composite can be optimized by integrating an appropriate loading of oxidation and reduction co-catalysts, drawing insights into appropriate catalytic materials from the growing body of work on photocatalytic water splitting, and via modification of crystal structure and morphology to promote ROS production.

Further work is required to evaluate the catalytic properties of barium titanate in aqueous solution. Whether BTO is an active aqueous catalyst depends on the adsorptive properties of BTO for water molecules, dissolved gasses, and organic contaminants. The capacity of BTO to release current in aqueous environments (and therefore generate power) is another critical parameter for the application of barium titanate as an in-situ piezocatalyst and warrants detailed electrochemical studies of the composite mats.

Piezoelectric materials may also be incorporated into existing water treatment technologies (such as membranes) to reduce biofouling by applying an electric potential to the piezoelectric materials to 'flex' and cause biofilm to detach from the membrane. Moreover, if BTO is shown to be catalytically active in aqueous environments, engineering CNF/BTO composites may be used for disinfection as well as contaminant degradation. Indeed, chemical oxidation (typically with ozone, chlorine dioxide, hypochlorous acid, chlorine gas, or permanganate) is already the industry standard for disinfection. Spontaneous generation of powerful aqueous oxidants could supplement existing disinfection practices.

LITERATURE CITED

1. Van Metre, P.C., et al., *Complex mixtures of Pesticides in Midwest U.S. streams indicated by POCIS time-integrating samplers.* Environmental Pollution, 2017. **220, Part A**: p. 431-440.
2. Wu, M., et al., *Still Poisoning the Well Atrazine Continues to Contaminate Surface Water and Drinking Water in the United States* 2010, The National Resources Defense Council
3. Godoy, A.A., F. Kummrow, and P.A.Z. Pamplin, *Occurrence, ecotoxicological effects and risk assessment of antihypertensive pharmaceutical residues in the aquatic environment - A review.* Chemosphere, 2015. **138**: p. 281-291.
4. Bartelt-Hunt, S., et al., *Occurrence of steroid hormones and antibiotics in shallow groundwater impacted by livestock waste control facilities.* J Contam Hydrol, 2011. **123**(3-4): p. 94-103.
5. Harner, T., et al., *Using Passive Air Samplers To Assess Urban−Rural Trends for Persistent Organic Pollutants. 1. Polychlorinated Biphenyls and Organochlorine Pesticides.* Environmental Science & Technology, 2004. **38**(17): p. 4474-4483.
6. Stackelberg, P.E., et al., *Persistence of pharmaceutical compounds and other organic wastewater contaminants in a conventional drinking-water-treatment plant.* Science of The Total Environment, 2004. **329**(1–3): p. 99-113.
7. *Pharmaceuticals in Drinking-Water* 2012, World Health Organization: France
8. Caliman, F.A. and M. Gavrilescu, *Pharmaceuticals, Personal Care Products and Endocrine Disrupting Agents in the Environment - A Review* Clean - Soil Air Water 2009. **37**(4-5): p. 277 - 303.
9. *Contaminant Candidate List (CCL) and Regulatory Determination*. 2016 November 17th, 2016 [cited 2017 March 12]; Contaminant Candidate List 4 - CCL4]. Available from: https://www.epa.gov/ccl/contaminant-candidate-list-4-ccl-4-0.
10. Uhlenbrook, S. and M. Miletto, *Water and Jobs* in *The United Nations World Water Development Report 2016*, R. Connor, Editor. 2016, United Nations World Water Assessment Programme Paris, France
11. Tchobanoglous, G., *Trends in Indirect and Direct Potable Reuse* in *Research and Innovations in Urban Water Sustainability* 2012: 2012 NWRI Clarke Prize Conference
12. Johnson, S.E. and S.E. Brennan, *Water Reuse: Expanding the Nation's Water Supply Through Reuse of Municipal Wastewater* 2011, Committee on the Assessment of Water Reuse as an Approach to Meeting Future Water Supply Needs; National Research Council Washington, D.C. .
13. Chou-Hoofman, H.-Y., *2015 Reuse Inventory*. 2016, Florida Department of Environmental Protection Water Reuse Programs: Tallahassee, Florida
14. Oulton, R.L., T. Kohn, and D.M. Cwiertny, *Pharmaceuticals and personal care products in effluent matrices: A survey of transformation and removal during wastewater treatment and implications for wastewater management.* J Environ Monit, 2010. **12**(11): p. 1956-78.

15. Comninellis, C., et al., *Advanced oxidation processes for water treatment: advances and trends for R&D.* Journal of Chemical Technology & Biotechnology, 2008. **83**(6): p. 769-776.
16. *Identifying Future Drinking Water Contaminants*. 1999, National Research Council Washington, D.C. .
17. Thompson, C., et al., *Forty Years of Ozone Experience Treating Municipal Water Supplies in the United States.* Ozone News 2014. **42**(3): p. 17-23.
18. van der Vegt, H. and I. Iliev, *Patent Landscape Report on Membrane Filtration and UV Water Treatment*. 2012, World Intellectual Property Organization
19. Thomas, A., *Global Ozone Technology Market Will Reach $1,242.0 million by 2020* 2014.
20. Cumming, S., *Global Market for Reverse Osmosis Membranes and Components Growing at 10.5% CAGR* 2015.
21. Raucher, R.S., et al., *Risks and Benefits of Energy Management for Drinking Water Utilities* 2008, AWWA Research Foundation U.S.A.
22. Pabi, S., et al., *Electricity Use and Management in the Municipal Water Supply and Wastewater Industries* 2013, Electric Power Research Institute
23. Milmo, S., *Going with the flow* Chemistry & Industry 2014. **78**(5): p. 32 - 35.
24. *Water Treatment Chemicals* in *Gains will be supported by growing use of recycled water, which requires more chemical treatment than fresh supply water or wastewater, as well as by growing use of membranes that require chemical pretreatment* 2015, Freedonia Group
25. Tang, C., et al., *Biomimetic aquaporin membranes coming of age.* Desalination, 2015. **368**: p. 89-105.
26. Ruiz, A.J., *Israeli-based WellToDo Announces Entry into Nevada Will Conduct Nitrate Removal Pilot Program* 2016, Water Start.
27. Baur, C., et al. *Advances in piezoelectric polymer composites for vibrational energy harvesting* 2014.
28. Cook-Chennault, K.A., N. Thambi, and A.M. Sastry, *Powering MEMS portable devices—a review of non-regenerative and regenerative power supply systems with special emphasis on piezoelectric energy harvesting systems.* Smart Materials and Structures, 2008. **17**(4): p. 043001.
29. *Piezoelectric Devices Market by Material (Piezoceramics, Piezopolymers, Piezocomposites, Piezocrystals), Product (Actuators, Transducers, Motors, Sensors, Generators), Application (Industrial, Automotive, Healthcare, Consumer) - Global Forecast to 2022* 2017, marketsandmarkets.com.
30. Moheimani, S.O.R. and A.J. Fleming, *Piezoelectric Transducers for Vibration Control and Damping* Advances in Industrial Control ed. M.J. Grimble and M.A. Johnson. 2006, Germany Springer-Verlag London Limited 250.
31. *Piezoelectric Constants*. 2016; Available from: https://www.americanpiezo.com/knowledge-center/piezo-theory/piezoelectric-constants.html.
32. Starr, M.B., J. Shi, and X. Wang, *Piezopotential-driven redox reactions at the surface of piezoelectric materials.* Angew Chem Int Ed Engl, 2012. **51**(24): p. 5962-6.

33. Starr, M.B. and X. Wang, *Fundamental analysis of piezocatalysis process on the surfaces of strained piezoelectric materials.* Sci Rep, 2013. **3**: p. 2160.
34. Rossmeisl, J., A. Logadottir, and J.K. Nørskov, *Electrolysis of water on (oxidized) metal surfaces.* Chemical Physics, 2005. **319**(1–3): p. 178-184.
35. Tchobanoglous, G., F.L. Burton, and H.D. Stensel, *Wastewater Engineering* 4th ed. 2003, New York, NY: McGraw-Hill Higher Education
36. Hong, K.-S., et al., *Piezoelectrochemical Effect: A New Mechanism for Azo Dye Decolorization in Aqueous Solution through Vibrating Piezoelectric Microfibers.* The Journal of Physical Chemistry C, 2012. **116**(24): p. 13045-13051.
37. Takeo, F., F. Koji, and F. Eiichi, *Electromechanical Properties in the Composites of Epoxy Resin and PZT Ceramics.* Japanese Journal of Applied Physics, 1976. **15**(11): p. 2119.
38. Han, K., A. Safari, and R.E. Riman, *Colloidal Processing for Improved Piezoelectric Properties of Flexible 0–3 Ceramic–Polymer Composites.* Journal of the American Ceramic Society, 1991. **74**(7): p. 1699-1702.
39. Tan, Y., et al., *Unfolding grain size effects in barium titanate ferroelectric ceramics.* Sci Rep, 2015. **5**: p. 9953.
40. Zhu, Y.-F., Q.-Q. Ni, and Y.-Q. Fu, *One-dimensional barium titanate coated multi-walled carbon nanotube heterostructures: synthesis and electromagnetic absorption properties.* RSC Advances, 2015. **5**(5): p. 3748-3756.
41. Kang, M.-G., et al., *Enhanced piezoelectric properties of vertically aligned single-crystalline NKN nano-rod arrays.* Scientific Reports, 2015. **5**: p. 10151.
42. Xu, S., B.J. Hansen, and Z.L. Wang, *Piezoelectric-nanowire-enabled power source for driving wireless microelectronics.* Nature Communications, 2010. **1**: p. 93.
43. Panda, P.K., *Review: environmental friendly lead-free piezoelectric materials.* Journal of Materials Science, 2009. **44**(19): p. 5049-5062.
44. *Piezoelectric Ceramics Electro Ceramic Solutions* M.A. Materials, Editor. 2013, Morgan Advanced Materials plc.
45. Mao, Y., S. Banerjee, and S.S. Wong, *Large-Scale Synthesis of Single-Crystalline Perovskite Nanostructures.* Journal of the American Chemical Society, 2003. **125**(51): p. 15718-15719.
46. Vijatović, M.M., J.D. Bobić, and B.D. Stojanović, *History and Challenges of Barium Titanate: Part I* Science of Sintering, 2008. **40**: p. 155-165.
47. Evans, J., H.T. , *An X-Ray Diffraction Study of Barium Titanate*. 1953, Massachusetts Institute of Technology
48. Li, F., et al., *Piezoelectric activity in Perovskite ferroelectric crystals.* IEEE Trans Ultrason Ferroelectr Freq Control, 2015. **62**(1): p. 18-32.
49. Kwei, G.H., et al., *Structures of the ferroelectric phases of barium titanate.* The Journal of Physical Chemistry, 1993. **97**(10): p. 2368-2377.
50. Eckert, J.O., et al., *Kinetics and Mechanisms of Hydrothermal Synthesis of Barium Titanate*. Journal of the American Ceramic Society, 1996. **79**(11): p. 2929-2939.
51. Maxim, F., et al., *Hydrothermal Synthesis and Crystal Growth Studies of BaTiO3 Using Ti Nanotube Precursors.* Crystal Growth & Design, 2008. **8**(9): p. 3309-3315.

52. Inada, M., et al., *Facile synthesis of nanorods of tetragonal barium titanate using ethylene glycol.* Ceramics International, 2015. **41**(4): p. 5581-5587.
53. Urban, J.J., et al., *Synthesis of Single-Crystalline Perovskite Nanorods Composed of Barium Titanate and Strontium Titanate.* Journal of the American Chemical Society, 2002. **124**(7): p. 1186-1187.
54. Kang, S.-O., et al., *Synthesis of single-crystal barium titanate nanorods transformed from potassium titanate nanostructures.* Materials Research Bulletin, 2008. **43**(4): p. 996-1003.
55. Joshi, U.A. and J.S. Lee, *Template-Free Hydrothermal Synthesis of Single-Crystalline Barium Titanate and Strontium Titanate Nanowires.* Small, 2005. **1**(12): p. 1172-1176.
56. Pierson, H.O., *Handbook of Carbon, Graphite, Diamond and Fullerenes* 1993, Park Ridge, New Jersey Noyes Publications
57. Peter, K.T., *Development of electrospun nanofiber composites for point-of-use water treatment* in *Civil and Environmental Engineering* 2016, University of Iowa Iowa City
58. Hooker, M.W., *Properties of PZT-Based Piezoelectric Ceramics Between -150 and 250C*. 1998, Lockheed-Martin Engineering & Sciences Co. : Hampton, VA
59. *Material: Lead Zirconate Titanate (PZT).* MEMS & Nanotechnology Exchange
60. Shuai, D., et al., *Development and Application of Piezoelectric Nanoheterostructures to Reduce the Chemical and Energy Demand of Water Treatment* 2014.
61. Ertuğ, B., *The Overview of The Electrical Properties of Barium Titanate* American Journal of Engineering Research 2013. **2**(8): p. 01-07.
62. *Material: Zinc Oxide (ZnO), film* MEMS & Nanotechnology Exchange
63. Jean-Mistral, C., S. Basrour, and J.-J. Chaillout, *Comparison of electroactive polymers for energy scavenging applications* Smart Materials and Structures 2010. **19**(8).
64. *Crystal Quartz* Boston Piezo-Optics Inc. .
65. Morgan, D.L., et al., *Implications of Precursor Chemistry on the Alkaline Hydrothermal Synthesis of Titania/Titanate Nanostructures.* The Journal of Physical Chemistry C, 2010. **114**(1): p. 101-110.
66. Ico, G., et al., *Size-dependent piezoelectric and mechanical properties of electrospun P(VDF-TrFE) nanofibers for enhanced energy harvesting.* Journal of Materials Chemistry A, 2016. **4**(6): p. 2293-2304.
67. Blumel, S., H.J. Knackmuss, and A. Stolz, *Molecular cloning and characterization of the gene coding for the aerobic azoreductase from Xenophilus azovorans KF46F.* Appl Environ Microbiol, 2002. **68**(8): p. 3948-55.
68. Perez-Urquiza, M. and J.L. Beltran, *Determination of the dissociation constants of sulfonated azo dyes by capillary zone electrophoresis and spectrophotometry methods.* J Chromatogr A, 2001. **917**(1-2): p. 331-6.
69. Hisashi, H. and K. Hiroo, *Effect of Dissolved Oxygen in Water on H 2 O 2 Production Rate by Sonication.* Japanese Journal of Applied Physics, 2003. **42**(5S): p. 2958.

70. Chen, D., S.K. Sharma, and A. Mudhoo, *Handbook on the Applications of Ultrasound, Sonochemistry for Sustainability* 2012, Boca Raton, FL: Taylor & Francis Group, LLC.
71. Macyk, W., et al., *Titanium(IV) complexes as direct TiO2 photosensitizers.* Coordination Chemistry Reviews, 2010. **254**(21–22): p. 2687-2701.
72. Greenstein, K.E., *Development of Chemically Active Metal Oxide Composite Nanofiber Filters for Water Treatment* in *Civil and Environmental Engineering* 2016, University of Iowa Iowa City.
73. Peter, K.T., et al., *Synthesis, Optimization, and Performance Demonstration of Electrospun Carbon Nanofiber–Carbon Nanotube Composite Sorbents for Point-of-Use Water Treatment.* ACS Applied Materials & Interfaces, 2016. **8**(18): p. 11431-11440.
74. *Phthalic anhydride* [Web Page] 2015 2015; Available from: http://www.chemspider.com/Chemical-Structure.6552.html.
75. Mittal, J., et al., *Denitrogenation behavior and tensile strength increase during carbonization of stabilized pan fibers.* Carbon, 1998. **36**(9): p. 1327-1330.
76. Moreira, F.C., et al., *Electrochemical advanced oxidation processes: A review on their application to synthetic and real wastewaters.* Applied Catalysis B: Environmental, 2017. **202**: p. 217-261.